Surface response of ceramics subject to erosive wear

Gonzalo García-Atance Fatjó

A thesis submitted in partial fulfilment of the requirements of
Bournemouth University for the degree of Doctor of Philosophy

Bournemouth University

October 2010

Copyright Statement

Abstract

Surface response of ceramics subject to erosive wear

Research concerning the surface of technical ceramics is carried out from the viewpoint of their mechanical performance subjected to relevant operating conditions. The selected materials are silicon nitride, zirconia and alumina. They are subjected to cavitation erosion and other wear processes. When polished ceramics are subjected to cavitation, a pseudoplastic deformation pit is discovered, as well as a delayed phase transformation or ageing of the zirconia stored at room temperature. Measured ageing times recorded are of the order of one month. These two discoveries are novel and a full explanation is explored. The creation of cracks that release the slip planes of ceramic grains allowing plastic deformation is proposed to be the main mechanism. In order to understand the relationship of the zirconia surface degradation with its oxides (yttria or magnesia), several material compositions are tested. It is concluded that the delay of phase transformation relies on the existence of partially stabilized tetragonal zirconia regardless of the oxide used to stabilize it.

Part of this research consists of understanding the effects of the experimental procedure that is utilised on the behaviour of the material. An unexpected non homogeneous cavitation erosion shape is obtained when an ultrasonic horn of small diameter is used to produce the bubbles. This non homogeneous region, referred to as ring region for this research, affects the erosion pattern of the material and it differs from the typical ones obtained when following the standard test. The acoustic theory does not explain this phenomenon. Therefore, a new approach is followed. This approach consists of using fluid mechanics equations combined with analytical mechanics principles. It is concluded that the location of cavitation clusters fulfils a condition of minimum energy. On the other hand, there are important differences between this experimental set up and the set up suggested by the published standards. These differences are discussed and a criterion for cavitation erosion resistance is developed. The comparison of cavitation resistance of materials is achieved by means of surface loss as criterion instead of volume loss.

Journal articles resulting from this research

García-Atance Fatjó, G., Hadfield, M., Vieillard, C., and Sekulic, J., 2009. Early stage cavitation erosion within ceramics--an experimental investigation. Ceramics International, 35 (8), 3301-3312.

G. García-Atance Fatjó, A. Torres Pérez, M. Hadfield, 2011, Experimental study and analytical model of the cavitation ring region with small diameter ultrasonic horn, Ultrasonics Sonochemistry, Volume 18, Issue 1, January 2011, Pages 73-79

Conference presentations resulting from this research

García-Atance Fatjó G., Hadfield M., Tabeshfar K. Pitfalls of performing ultrasonic cavitation erosion under a non-standard configuration. TriboUK, Imperial College, London, 22-23 April 2010.

García-Atance Fatjó G., Hadfield M., Tabeshfar K. Cavitation erosion mechanisms in polished ceramics. 19th Mission of Tribology Research, Institution of Mechanical Engineers, London, 1 December 2010.

Contents

List of figures

List of tables

Dedication

A mi madre,

y a mis hermanas.

Acknowledgements

I would like to thank my first supervisor, Professor Mark Hadfield, especially for his enormous support when I first came to this country.

I would like to thank my second supervisor, Professor Kamran Tabeshfar. I really appreciate his interesting feedback about materials.

I am very grateful for the things I have learnt from Angel Torres Pérez about programming, numerical analysis, electronics and tribology.

I would like to thank SKF Engineering and Research Centre who funded a short project that was the initial part of this research.

I would like to thank Dr. Robin Cundill and Professor Pirouz Pirouz for their encouraging visits. Also, I am grateful towards Dr. Jose Luis Viesca Rodríguez, Dr. Antolín Hernández Battez and Dr. Rubén González from Oviedo University.

Also, I would like to express my gratitude to the staff of Bournemouth University and Student Union who has supported and helped me during my time as a PhD student.

Author's Declaration

This thesis contains the original work of the author except otherwise indicated.

Glossary

a contact radius; amplitude of the horn tip oscillation (Chapter 3)

ASTM American Society for Testing and Materials

c speed of sound in bubbly liquid

c_f speed of sound in liquid

c_g speed of sound inside the gas of a bubble

C path of the variables along the time to apply Hamilton's principle

$C1$ path close to C

d effective diameter of the cavitation ring region

d_i diameter of the internal edge of the cavitation ring region

d_e diameter of the external edge of the cavitation ring region

E elastic modulus; kinetic energy of the system (Chapter 3)

E' reduced elastic modulus of ball A and B

E_A reduced elastic modulus of ball A

E_B reduced elastic modulus of ball B

f frequency of the oscillation of the horn tip

h_0 minimum film thickness; initial gap between the horn and the sample (Chapter 3)

h distance or instant gap between the horn and the sample

h' velocity of the horn tip

H hardness

H_v10 Vickers hardness for 10 kilogram load.

H_{Ra} Rockwell hardness, scale A.

i intensity of turbulence

I integral to apply Hamilton's principle

k ellipticity of contact; parameter, expresses the surrounding influence (Chapter 3)

K_C fracture toughness

p pressure

p_{max} maximum contact pressure

r radial cylindrical coordinate

R horn radius

R' reduced radius of ball A and B

R_A radius of ball A

R_B radius of ball B

R_E external radius of the system

R_{C1} internal radius of the liquid region "1"

R_{M1} radius where the fluid velocity is zero in liquid region "1"

R_{M2} radius where the fluid velocity is zero in liquid region "2"

R_R radius of the cavitation ring region.

R_{R1} external radius of the liquid region "1"

R_{R2} internal radius of the liquid region "2"

SEM scanning electron microscope

t time

t_0 initial time for a period

t_1 final time for a period

v fluid velocity (assumed here only along radial coordinate)

v_M maximum fluid velocity at $r = R$

v_r fluid velocity along radial coordinate when there is turbulence

v_z fluid velocity along vertical coordinate when there is turbulence

v_θ fluid velocity along angular coordinate when there is turbulence

U average entraining surface velocity

W normal load; power (Chapter 3)

z vertical cylindrical coordinate

α pressure-viscosity coefficient

β proportion of volume occupied by gas in a liquid

η_0 viscosity of the lubricant

λ film parameter

v_A Poisson's ratio of ball A

v_B Poisson's ratio of ball B

ρ_f density of fluid

σ_A RMS surface roughness of ball A

σ_B RMS surface roughness of ball B

σ_r stress in radial direction

σ_t stress in tangential direction

θ angular cylindrical coordinate

$2d\psi$ aperture of the differential cone

Chapter 1   Introduction

1.1 Background

Ceramic materials have been used by the human being since the New Stone Age in pottery. This material is characterised by being non-metallic inorganic solid made by a process of heating it inside of a kiln or an oven and it often presents a crystalline structure in contrast to the glasses. Nowadays, ceramic materials can be found in building applications, such as bricks and roof tiles; refractory applications, such as kilns or crucibles; house appliances, such as pottery and sanitary ware; and technical applications, such as bearings or prosthesis. Figure 1.1 shows that ceramic materials have increased their importance in the last decades and this tendency will be maintained over the next decade (Ashby 1999). This research is focused in the so called technical ceramics, and specifically in those that are used in bearings. The most common technical ceramics used in bearings according to the catalogues of the manufactures are silicon nitride, zirconia and alumina.
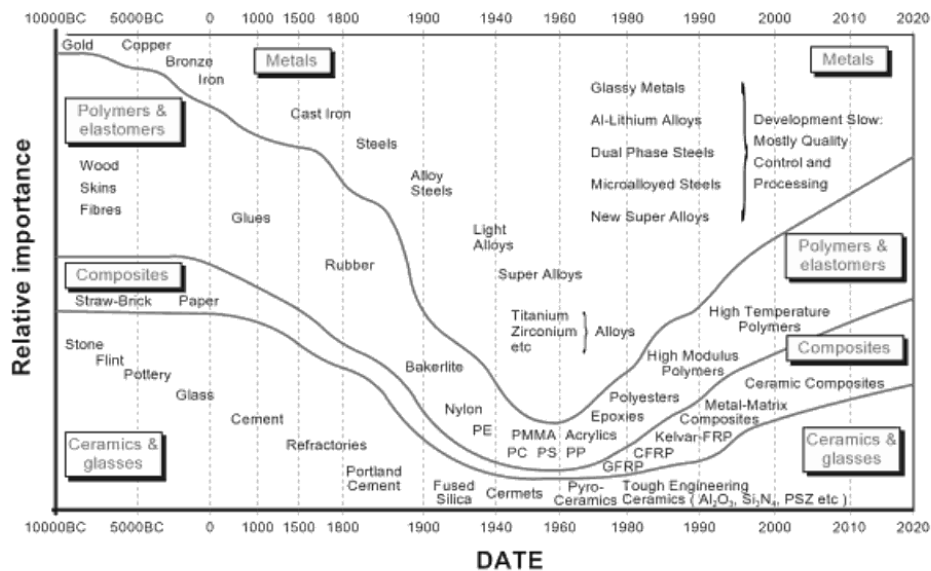
Figure 1.1 Evolution of engineering materials. Taken from Ashby (1999).

Tribology is the science that studies the lubricants, lubrication, friction, wear and bearings (Dowson 1998). The multidisciplinary nature of tribology is at once its

weakness and strength (Dowson 1998). This requires from researches the skill to work using knowledge from different scientific disciplines. The lubricants can be classified in mineral oils; synthetic oils; emulsions and aqueous lubricants; and greases. Also, lubricants can contain additives in order to improve their performance in relation to wear, friction, oxidation, corrosion, contamination control, viscosity, pour point and foam inhibition (Stachowiak and Batchelor 2001). The lubrication can be classified in terms of the distance and interaction between the surfaces as: hydrodynamic lubrication; hydrostatic lubrication; elastohydrodynamic lubrication; boundary and extreme pressure lubrication; and solid lubrication (Stachowiak and Batchelor 2001).

Wear has been studied extensively during the 20th century. It is a phenomenon that depends on a large number of variables such as material properties, microstructure, lubrication, contact conditions, temperature, sliding speed, surface topography and external particles. Archard (1953) found a simple model that explains that the wear rate is proportional to the load.

Wear can occur in different mechanisms. The most common are abrasive, erosive, adhesive, corrosive, and fatigue wear. Abrasive wear occurs when a solid is loaded and slides against other material with greater or equal hardness. Erosive wear occurs when the surface receives the impact of particles of solid or liquid. Adhesive wear occurs when the two surfaces contact one each other and some degree of adhesion between them appears. Corrosive wear is produced by chemical reaction between the worn material and a corroding medium. Fatigue wear happens when the surface is subjected to a cyclic load and the wear particles are generated by fatigue propagated cracks. Besides, it is possible to define a different mechanism that is fretting wear. Fretting wear occurs when the sliding amplitude is very small, even to the point that some regions of the contact do not have relative movement (Stachowiak and Batchelor 2001).

Friction is the resistance to motion during sliding or rolling that happens in the relative motion of one solid body that moves tangentially to another in contact (Bhushan 2002). This resistance to motion is, sometimes, a negative output in the use

of a mechanism, for example, a bearing, while other times is something pursued, for example in brakes. A bearing is a device that allows two components in a mechanism to move relative to one another in either one or two dimensions while it constrains their movement in the other dimensions (Williams 1994).This definition covers a large variety of bearing types. A journal bearing allows the rotation of a shaft under a radial load. A Linear bearing allows motion in one direction. A thrust bearing allows rotation of the shaft with a load parallel to the axis of rotation. There are some kind of bearings that work as a journal and thrust bearing at the same time. Dry bearings are those that work without lubricant, allowing the surfaces to rub together. Fluid film bearings are those who work with a fluid lubrication. Rolling bearings have a third body, a roller or a ball, that is placed between the bearing surfaces. Magnetic or electrostatic levitation bearing are those who use an electrostatic or magnetic repulsion to keep the surfaces separated. (Williams 1994).

The capacity of the material within a rolling bearing to sustain the loads applied without undergoing such deformation that would lead to failure before the end of an acceptable lifetime is fundamental. This is a requirement for the selection of a specific bearing material. A rolling bearing would fail because of a fracture, a fatigue failure or an excessive wear. The most common material for bearings is the steel known as SAE 52100, EN31 or 535A99 whose composition is 1 percent Carbon and 1.5 per cent Chromium. Ceramics are good candidates for bearings due to their high hardness, excellent temperature stability and low density in comparison to the steel. (Williams 1994).

Figure 1.2 Silicon nitrides (balls and rods), alumina
(specimen) and zirconias (rod and balls).

Studies of ceramic rolling elements started to be published at the beginning of the 70s (Baumgartner et al. 1973; Baumgartner and Whieldon 1973; Scott and Blackwell 1973; Scott et al. 1971; Wheildon et al. 1973). From the beginning, it was clear that the porosity and internal flaws of the ceramic material are limiting factors for its rolling contact fatigue life. However, the improvement of the manufacturing process has allowed them to be widely used in specific and high demanding applications. The most common use of ceramic materials in rolling contact is as rolling elements of hybrid bearings. These bearings have the rolling elements made of ceramic material while the races are made of steel. Other variety of ceramic bearing is the full ceramic bearing that has the rolling elements and the races made of ceramic material. The ceramic rolling elements are normally balls but they may be rollers in some cases.

Other application of technical ceramics is as biocompatible materials in medicine. Studies of tooth prostheses made of ceramic have been published over the 20th century (Drum 1939). This provides an extensive source of information for those ceramics that are used either in prostheses or in bearings. This is the case of zirconia (ZrO_2) and alumina (Al_2O_3) due to their white colour. Also, orthopaedic prostheses use ceramic materials (Lyng et al. 1973).

One of the main mechanical behaviours for ceramics is the elastic deformation followed by brittle failure in tension. The failure is originated from existing flaws within the surface or subsurface. As different specimens have different flaws, the strength of the material varies and has to be statistically treated. The distribution used to model the behaviour of strength on ceramic is the Weibull distribution, where a high Weibull modulus means that there is consistency in different specimens while a low Weibull modulus means there is not such consistency. A good ceramic material should have relatively high strength and high Weibull modulus. Also, cracks often grow slowly under applied loads well below their strength leading to an eventual failure. This phenomenon is known as subcritical crack propagation and it is different from cyclic fatigue failure. The time of failure of the ceramic under a static stress big enough to produce subcritical crack propagation is longer than the time for an alternating stress of the same value (Wachtman 1996). The fatigue failure of

silicon nitride rolling elements has been extensively studied (Hadfield 1995, 1998; Hadfield and Stolarski 1995; Wang and Hadfield 1999, 2000a, 2000b). The fatigue life of rolling elements increases in this order: silicon carbide, alumina, zirconia and SiAlON (Asada et al. 1997).

The wear modes of technical ceramics can be briefly classified as mild wear and severe wear. In mild wear, tribochemical reactions take place forming a surface that is detached and also the wear is driven by mechanically forming fine wear debris one-tenth or smaller than the grain size (Kato and Adachi 2002). This wear types are corrosive and abrasive wear in the classification given before. Conversely, the severe wear takes place when the debris is of the size of the grain, and is formed by mechanical cracking of grains or delamination of film of the scale of the grain size. This happens with higher contact pressures (Adachi et al. 1997; Kato and Adachi 2002). Although technical ceramics such as silicon nitride, zirconia, alumina and silicon carbide, are known for being high wear resistance and chemical resistance materials, this abrasive and corrosive wear occurs in their surface, but the wear rate is smaller than the wear rate of other common materials.

Cavitation erosion is a wear mechanism produced by the impact of fluid at high speed against the surface. This high speed is produced by collapsing bubbles that were created in a condition of fluid with a pressure under its vapour pressure and returned to a pressure higher than the vapour pressure (Young 1999). The bubbles may be produced by one of the following mechanisms: in ultrasonic cavitation, the region of low vapour pressure is created with a vibrating surface at ultrasonic frequency; in hydrodynamic cavitation, the region of low vapour is created by the speed of the fluid around a hydrodynamic surface with a specific shape; and in laser cavitation, the bubble is created by increasing the temperature of the liquid at one point, this case is useful to study the collapsing of a single bubble. Since the impact of the liquid is very severe, it can damage any material, including ceramics, and erode them. As ceramics are used in devices that may be subjected to cavitation erosion, such as bearings, injectors or valves, it is necessary to study the cavitation erosion resistance and erosion mechanisms of ceramics in order to improve their performance.

On the other hand, it is important to note that other phenomena different to the cavitation explained here receive also the name of cavitation in the field of this research. Cavitation in the sintering process of silicon nitride refers to the existence of internal cavities within the material. In the present study cavitation refers to fluid mechanic cavitation unless otherwise stated.

This research is focused on the wear of technical ceramics used in bearings. The chosen ceramics are bearing grade silicon nitride and zirconia, and pure alumina. The wear mechanisms are mainly cavitation erosion, polishing manufacturing process, lapping, rolling and indentations. The approach is mainly in terms of surface geometry. Also, the erosion process with cavitation exposure is studied in detail.

1.2 Literature Review

Technical ceramics have been studied in the last decades from the point of view of their wear performance. These wear properties are related to their physical properties, such as high elastic modulus, high hardness, chemical resistance, resistance to high temperature. However, there is normally a drawback with these materials which is their brittleness. In the following sections, the erosion of ceramics is reviewed, both as erosion by particles and cavitation erosion. Also there is a brief review of the structure of ceramics and the phase transformation of zirconia. Finally, other common aspects of the tribological study of ceramic balls are presented.

1.2.1 Erosion of ceramics.

Erosion is the wear mechanism produced by the impact of particles or liquids on the surface. Technical ceramics subjected to this wear mechanism behave in a characteristic manner due to their hardness and brittleness and it has been studied in the literature. Here, a summary of the latest research on this topic is presented. Cavitation erosion is a specific mechanism that is presented independently in the following section.

Erosion of ceramics is one of the major problems in various applications such as valves in natural gas wells (Celotta et al. 2007) or turbine blades in a wet steam environment (Oka and Miyata 2009). The literature includes studies of the erosion resistance of ceramics for various particle materials, size and impact angle. Also, the effect of water jets is studied.

Fang et al. studied the erosion of ceramic materials by a sand water slurry jet. The purpose of the water was to carry and to accelerate the sand. They concluded that zirconia has the best erosion resistance among a group of alumina, sialon and silicon carbide; that the erosion mechanism involves both brittle fracture as well as plastic deformation (ductile) although the maximum erosion rate corresponds to a 90º impact angle (Fang et al. 1999b). The 90º angle suggested that the main contribution to wear was brittle fracture since, aluminium, as a ductile material, showed maximum erosion rate at 15º. The combined effect of corrosion and erosion in the ceramic surface was studied. Corrosion creates a weak surface that is easily removed by the erosion (Fang et al. 1997). In the case of partially stabilized zirconia, it was concluded that some transformation from tetragonal to monoclinic is induced by the impact stresses but mainly, it is induced by corrosion generated by hydrofluoric acid (HF) and hydrochloric acid (HCl) solutions (Fang et al. 1999a).

Celotta et al. studied the erosion resistance of tungsten carbide, silicon nitride and zirconia. They concluded that a new type of tungsten carbide with ultrafine grains has the best erosion resistance and it is consistent with the trend of improving erosion resistance trough a smaller grain size. In this case, zirconia and silicon nitride have worse resistance than tungsten carbide. On the other hand, extensive fragmentation of impact particles contributed to understand the high erosion resistance of hard ceramics (Celotta et al. 2007).

Choi et al. studied the wear mechanism of different silicon nitrides by erosion. They concluded that the best silicon nitride is the one with the finest microstructure. To manufacture it they used a fine starting powder for sintering. The wear resistance was not related to the fracture toughness. Also the erosion mechanism was mainly

grain dislodgement following intergranular fracture. Localized plastic deformation was observed on the eroded surface (Choi et al. 2003).

Oka et al. modelled the dependence of erosion rate with the angle and the hardness of the material. By calculating two exponents, one related to the brittle fracture and another related to the erosion by ductile mechanism, they studied in a systematic way the main mechanism of erosion in silicon carbide, alumina, zirconia and magnesia. The erosion rate was maximum at 90° impact-angle. The erosion was highly influenced by the particle size and slightly by the impact velocity (Oka et al. 2009). Previously, another author found that the erosion rate dependence with the angle presented a local maximum at 45° for silicon nitride, though the absolute maximum was at 90°. This was due to a ductile behaviour of the silicon nitride when it is eroded by SiC particles (Wang and Mao 1996). In that oblique impact condition, as the ductile behaviour plays the main role, the hardness is the predominant mechanical property for the erosion resistance. While in orthogonal impact condition, both hardness and toughness should be taken into account (D'errico et al. 1997, 2001).

Lathabai studied the grain effect of the erosion of partially stabilized zirconia Ce-TZP. He concluded that the erosion rate increases with increase in grain size from 2.3 μm to 5.4 μm, but a further increase to 10.3 μm does not result in further increase. Also he concluded that the hardness of the erosive particles and its velocity have a profound effect on the erosive wear (Lathabai 2000). On the other hand, on partially stabilized zirconia, the accumulated strain due to the impacts leads to phase transformation from tetragonal to monoclinic and reduces the erosion by transformation toughening (Tu and Li 1997).

Oka et al. studied the erosion resistance of ceramics and coating materials to water droplet impingement. They concluded that zirconia has excellent erosion resistance, that the droplet velocity dependence of the erosion rate is linear in a logarithmic scale and equal to 3 and that the erosion resistance of the material is strongly correlated to the fracture toughness (Oka and Miyata 2009).

The erosion wear of ceramics can be used in the manufacturing process. For example, it has been applied to round the edge of silicon nitride (Mohajerani and Spelt 2009). This is produced by micro-chipping on the edge. In contrast the erosion of ceramics is mainly, as the literature has explained, driven by brittle fracture, where sometimes the fracture toughness plays an important role. Ductile behaviour is also presented but plays a secondary role in the erosion of ceramics.

1.2.2   *Ceramics and cavitation erosion.*

When using technical ceramics in environments where cavitation can appear, the brittleness of the ceramics is an important factor that can produce a fast wear of the material. This is due to the high impacts that cavitation can produce on the surface, up to 1.5GPa (Karimi and Avellan 1986), in located points. For this reason, the cavitation resistance of the materials has been studied and the main outcomes are explained within in this section.

The cavitation in liquids is a phenomenon by which regions in a liquid subjected to a local low pressure become vapour, creating bubbles or cavities that when the local low pressure ceases they collapse. The collapsing of the bubbles is violent because the vapour becomes liquid suddenly. Cavitation can be compared with boiling in the sense that both produce vapour, but in boiling this is produced by a high temperature while in cavitation is produced by a low pressure. The changes of pressure can be made quickly, at speed of sound, while the changes of temperature cannot. In case the bubble collapses far away from a surface, the geometry tends to be symmetrical, while if it collapses close to a surface there is an asymmetry and the liquid tends to move towards the surface, filling the space created by the bubble and producing a jet stream. The pressures induced by consecutive jet streams eventually damage any surface. Coleman et al. took a famous micrograph that shows clearly a jet stream inside of the collapsing bubble (Coleman et al. 1987).
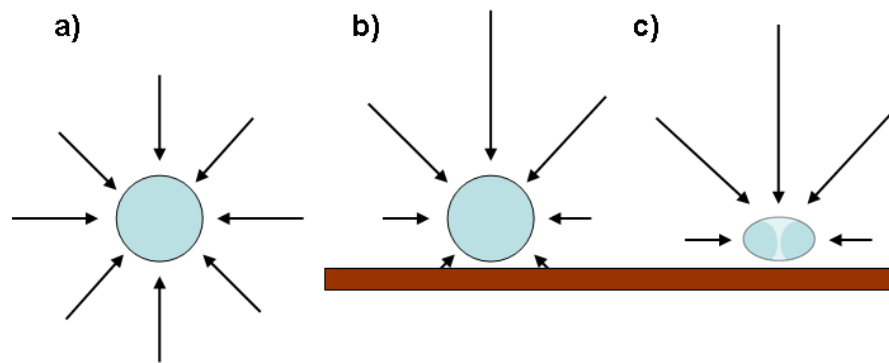
Figure 1.3. Cavitation, collapsing bubble. a) initial velocity; b) initial velocity when the bubble is close to a surface; c) collapsing bubble close to a surface.

In the case of cavitation erosion in ceramics, the finishing of the surface and the number of flaws and porosity have a drastic effect on the incubation time. Silicon nitride is found to be one of the ceramics with best performance in terms of cavitation resistance followed by zirconia, alumina(99.9%), silicon carbide, silicon carbide-boron carbide composites, boron carbide and alumina (97.5%) (Tomlinson and Matthews 1994). It is important to note that this study was published in 1994 and since then, the manufacturing processes and final quality of the materials have been changed. This is important because of the role that internal flaws and microstructure have in the cavitation erosion performance.

Alumina cavitation resistance has been studied extensively in relation to purity and microstructure. It is found that pure alumina has better performance than debased alumina, that a larger grain size leads to a higher erosion rate and that the main mechanism of erosion is the dislodging of whole grains due to fracture in the intergranular glassy phase. Debased aluminas are those with more than 1% of glassy phase.(Tomlinson et al. 1999).

 Also, another study found, that the erosion rate of pure alumina depends on the grain size. Larger grain size leads to larger erosion rates. The dominant wear mechanisms are cracking of grain boundaries and detachment of grains. Higher cohesion strength at the grain boundaries produces better cavitation resistance. The material with best cavitation resistance is zirconia. A "home made" experimental ceramic made of

Zirconia and Alumina mixture had better performance than pure alumina of similar grain size. (Litzow et al. 2006)

The behaviour of ceramics in aqueous solutions (acid, base and NaCl) has been studied. There are no variations due to the media except for the erosion rate of alumina in base solution, that increases by 60%, and zirconia in acid solution, that increases by 25%. The erosion mechanism is intergranular fracture. The ranking in water is Silicon Nitride, Zirconia, Alumina and Macor^{TM}. (Niebuhr 2007)

The erosion mechanism of silicon nitride subjected to cavitation exposure has been studied. The cracking is mainly intergranular although some cracks are visible in big grains and elongated grains. These cracks produce erosion pits, most of them showing microcracks extension at the boundaries. This produces pits bridging or coalescence, removing successively more pits (Karunamurthy et al. 2010a).

Recently, a study of the relationship of cavitation erosion with rolling wear in silicon nitride has been published. Bearings in rocket engines can undergo cavitation due to the huge pressure variations and the lubrication with liquid oxygen or liquid nitrogen. Hence, the combination of both mechanisms produces a blistering on the surface of the rolling silicon nitride element that leads to pit proliferation and wear. (Karunamurthy et al. 2010b)

1.2.3 *Discussion of cavitation erosion resistance of ceramics.*

In order to have a clear image of the behaviour of different ceramic materials exposed to cavitation, a table is presented with the data reported in the previous studies (Table 1.1).

Table 1.1 Cavitation erosion resistance of ceramics. Rankings.

Rank	(Tomlinson and Matthews 1994)	(Tomlinson et al. 1999)	(Litzow et al. 2006)	(Niebuhr 2007)
1st	Silicon Nitride		Zirconia	Silicon Nitride
2nd	Zirconia (TZP)	Pure Aluminas	Silicon Carbide	Zirconia
3rd	Alumina (99.9%)		Alumina (fine)	Alumina
4th	Silicon Carbide		Alumina-Zirconia	Macor™
5th	Silicon Carbide-Boron Carbide	Debased Aluminas	Alumina (coarse)	
6th	Boron Carbide			
7th	Zirconia (PSZ)			
8th	Alumina (97.5%)			

The experimental set up of the studies that are reviewed here were slightly different to each other. The differences are presented in the next table for comparison and reference (Table 1.2).

Table 1.2 Experimental set ups of the studies.

	(Tomlinson and Matthews 1994)	(Tomlinson et al. 1999)	(Litzow et al. 2006)	(Niebuhr 2007)	(Astm 2003)
Frequency:	20 kHz	20 kHz	20 kHz	20 kHz	20 kHz
Amplitude:	50 μm	50 μm	25 μm	50 μm	50 μm
Diameter:	14 mm	14 mm	16 mm	15.9 mm	15.9 mm
Gap:	1 mm	1 mm	0.5 mm	1 mm	No agreement.
Temperature:	18 ±1 ℃	18 ±1 ℃	25 ±2 ℃	25 ±2 ℃	25 ±2 ℃
Depth:	3-6 mm	3-6 mm	12 ±4 mm	30 mm	12 ±4 mm

The standard states: "*Tests using a stationary specimen in close proximity to the horn tip have been described by several authors, but inconsistent findings concerning optimum separation distance have discouraged standardization to date*" (ASTM G32). For this reason it is possible to find differences among the experimental set ups in the previous works. However, it is recommendable to use the values of the standard as long as it is possible, for repeatability and comparison purposes.

In order to compare the volume loss rate of the different studies reviewed here, it is necessary to note that, the work of Litzow cannot be compared since the amplitude is different. However, the works of Tomlinson and Niebuhr may be compared as long as it is noted that the rates in Niebuhr are measured from an erosion area 29% bigger than in Tomlinson's, therefore, it is expected that this difference influences the results. Also, the deeper location in Niebuhr decreases the cavitation and the higher temperature in Niebuhr increases the cavitation (Young 1999).

1.2.4 *Microstructure of ceramics.*

The mechanical properties of ceramics are the result of their microstructure and the bonds of the atoms that constitute them. For this reason, the main microstructures of the ceramics are described here. One material can present different microstructures depending on the temperature and the containment of contaminants or additives.

Alumina is the most widely used ceramic. Its most common form is α-Alumina that shows a hexagonal close packed anion sublattice (oxygen ions) and the cations (aluminium ions) filling two-thirds of the octahedral interstices (Lee and Rainforth 1994). It has a structure that it is not easy to describe with a drawing due to its three dimensional complexity.

Zirconia, or zirconium dioxide, is a ceramic that shows different crystal structures at room temperature. This behaviour is called polymorphism (Figure 1.4). Monoclinic polymorph (m) is thermodynamically stable from room temperature to 950 °C. Tetragonal polymorph (t) is stable at high temperature. Also it is possible to find cubic polymorph (c) that, since it has an inter-atomic plane distance similar to the tetragonal value, can be extremely difficult to quantitatively differentiate from tetragonal zirconia. Finally, orthorhombic polymorph appears only in pure zirconia at high pressures (Lee and Rainforth 1994).
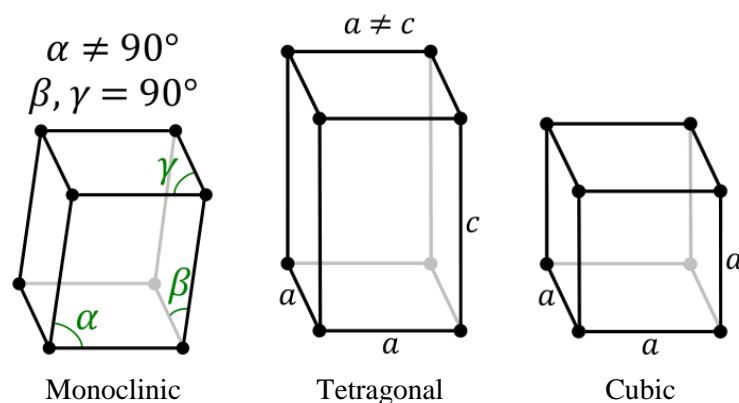
Figure 1.4 Zirconia crystals (GNU license).

Silicon nitride has two polymorphs, α and β. The structure of silicon nitride is built up of SiN_4 tetrahedra joined in a three-dimensional network, each nitrogen corner is common to three tetrahedra. The α and β forms are hexagonal. The difference is that in β-Si_3N_4 the SiN_4 are linked in such a way that there are tunnels parallel to the c-axis of the unit cell (Lee and Rainforth 1994). The typical microstructure of silicon nitride is grains of β-Si_3N_4 with needle shape in a glassy intergranular phase.

Sialons (SiAlON) are alloys of silicon nitride where some silicon atoms have been substituted by aluminium atoms and some nitrogen atoms by oxygen atoms. They have the same α and β structures as silicon nitride (Lee and Rainforth 1994).

1.2.5 *Discussion of the microstructure of ceramics.*

The Peierls-Nabarro stress is the force needed to move a dislocation within a plane. It is a theoretical value given by the shear modulus, the poisson´s ratio, the interatomic spacing and the interplanar spacing. This value might be seen as a theoretical value of the yield strength. The following literature survey was done in order to find information to calculate the Peierls-Nabarro stress.

An important work related to the microstructure of silicon nitride has been made by Grun (1979) since it fully defined the geometry. The crystal structure of β-Si_3N_4 is defined as a non-centrosymmetric space group $P6_3$. This is deduced by the measurement of the interatomic distances and bond angles that are represented in Table 1.3. However, when the values of this table were looked in detail, typographic mistakes were found. Hence, these mistakes are shown here. The Table 1.4 is the suggested correction of Table 1.3.

Table 1.3 Interatomic distances (Å) and bond angles (°) of β-Si$_3$N$_4$ P6$_3$ (Grun 1979).

Si-N(1)^I	1.728 (2)	Si-N(1)^{III}	1.767 (5)
Si-N(1)^{II}	1.704 (5)	Si-N(2)	1.730 (1)

	Angle	N-N distance
N(1)^{III}-Si-N(1)^I	109.4 (2)	2.801 (5)
N(1)^{II}-Si-N(2)	109.7 (5)	2.808 (9)
N(1)^I-Si-N(1)^{II}	113.5 (2)	2.902 (8)
N(1)^I-Si-N(2)	106.7 (1)	2.774 (1)
N(1)^I-Si-N(1)^{II}	106.6 (2)	2.801 (5)
N(2)-Si-N(1)^{II}	110.8 (5)	2.878 (9)

	Angle	Si-Si distance
Si^{IV}-N(1)-Si^{VI}	125.1 (3)	3.046 (1)
Si^{IV}-N(1)-Si^V	113.5 (1)	2.902 (0)
Si^{VI}-N(1)-Si^V	121.3 (3)	3.046 (1)
Si-N(2)-Si^{VII}	119.97 (4)	2.996 (1)

Equivalent positions

(I) x+1,y,z	(II) x-y,-y,z+0.5
(III) x-y,-y,z-0.5	(IV) -x,y-x,z+0.5
(V) -x,y-x,z-0.5	(VI) x-1,y,z
(VII) -y,y-x,z	

Table 1.4 Suggested corrections to Table 1.3. Interatomic distances (Å) and bond angles (°) of β-Si$_3$N$_4$ and corrections.

Si-N(1)^I	1.728 (2)	Si-N(1)^{III}	1.767 (5)
Si-N(1)^{II}	1.704 (5)	Si-N(2)	1.730 (1)

	Angle	N-N distance
N(1)^{II}-Si-N(1)^I	109.4 (2)	2.801 (5)
N(1)^{II}-Si-N(2)	109.7 (5)	2.808 (9)
N(1)^{III}-Si-N(1)^{II}	113.5 (2)	2.902 (8)
N(1)^I-Si-N(2)	106.7 (1)	2.774 (1)
N(1)^I-Si-N(1)^{III}	106.6 (2)	2.801 (5)
N(2)-Si-N(1)^{III}	110.8 (5)	2.878 (9)

	Angle	Si-Si distance
Si^{IV}-N(1)-Si^{VI}	125.1 (3)	3.046 (1)
Si^{IV}-N(1)-Si^V	113.5 (1)	2.902 (0)
Si^{VI}-N(1)-Si^V	121.3 (3)	3.046 (1)
Si-N(2)-Si^{VII}	119.97 (4)	2.996 (1)

Equivalent positions

(I) x+1,y,z	(II) x-y,-y,z+0.5
(III) x-y,-y,z-0.5	(IV) -x,y-x,z+0.5
(V) -x,y-x,z-0.5	(VI) x-1,y,z
(VII) -y,y-x,z	

1.2.6 *Phase transformation of zirconia.*

Zirconia, or zirconium dioxide, is mainly presented in two common crystal structures: tetragonal and monoclinic. The tetragonal phase is stable at high temperature while the monoclinic phase is stable at low temperature. Various dopants, such as yttria or magnesia can retain metastable tetragonal at room temperature, this metastable tetragonal phase can transform into monoclinic phase with an associated volume expansion, producing transformation toughening. This characteristic makes the zirconia a ceramic with very high flexure strength and good mechanical properties. It is widely used in prosthesis and the literature has studied the relationship of this transformation with the environment, the stress state and the mechanical properties.

When the tetragonal zirconia is stabilized with yttria (yttrium oxide), it is called Y-TZP; this is the most common presentation in dentistry and orthopaedic prosthesis. This material for prosthesis is widely studied in the literature. Specifically, recent studies have focused on the relationship of the flexural strength with the finishing (Ho et al. 2009; Kosmac et al. 1999), and the flexural strength with the finishing and ageing effects (Papanagiotou et al. 2006). This is important in order to minimize the risk of catastrophic failure of prosthesis.

Other studies have been focused on the ageing itself (Deville et al. 2006; Wada and Yokoyama 1999), for this purpose the 3%mol Y_2O_3-ZrO_2 was subjected to a high humidity and high temperature (>95 °C) treatments in order to achieve transformation from tetragonal to monoclinic phase in practical test times. Annealing releases residual stress (from the polishing or grinding) and transforms other phases in tetragonal phase. The rhombohedral phase that can appear as a result of the grinding process has been studied (Denry and Holloway 2006) and it has been found that is removed by annealing.

There is evidence that the phase transformation is related to chemical reactions, since when the specimens are soaked, some precipitates have been found; and that a high concentration of Zr and Y ions in water suppresses the tetragonal to monoclinic transformation (Wada and Yokoyama 1999). Also, the phase transformation is

related to the mechanical stress, the monoclinic phase has a 3-5% increase of volume and compressive stresses inhibit the transformation while tensile stresses are favourable to that (Li et al. 2001).

The main causes of the transformation of Y-TZP (yttria – tetragonal zirconia) into monoclinic phase have been studied. It is concluded that there are several factors that accelerate the transformation. The main factors are a tensile stress and the decrease of t-ZrO_2 stability due to the reaction of H_2O and Y_2O_3 that causes the emergence of Y_2O_3. Also it was calculated that a tensile stress of 425 MPa is the critical value to obtain stress-induced phase transformation, however, a tensile stress of 100 MPa accelerates the transformation but it does not produce the transformation by itself alone, it needs the reaction of water and yttria (Li et al. 2001).

1.2.7 *Discussion of zirconia articles.*

It has been found that the depth of the layer including monoclinic phase is greater in polished surfaces than in the cut surfaces (Wada and Yokoyama 1999). Also it has been stated in the article that this cannot be explained there. In other words, the transformed layer is deeper in the polished surface than in the cut surface, although the cut surface presents cracks and a higher proportion of monoclinic phase on the surface. In this research an explanation of this discord is suggested (Figure 1.5). According to other results of the same article, the polished surface presents a warped region at about 20 µm depth. This is a sign of the residual stress produced by the increase of volume in the transformation. It is known that the stress can produce the change of phase. In a polished surface this stress can be greater because of the homogeneous transformation and because it has not cracks to release the stress, this can produce a chain effect that achieves deeper grains. For this reason, although the proportion of the polished surface of monoclinic phase is smaller, the depth of the layer with monoclinic phase is greater than in the cut surface.
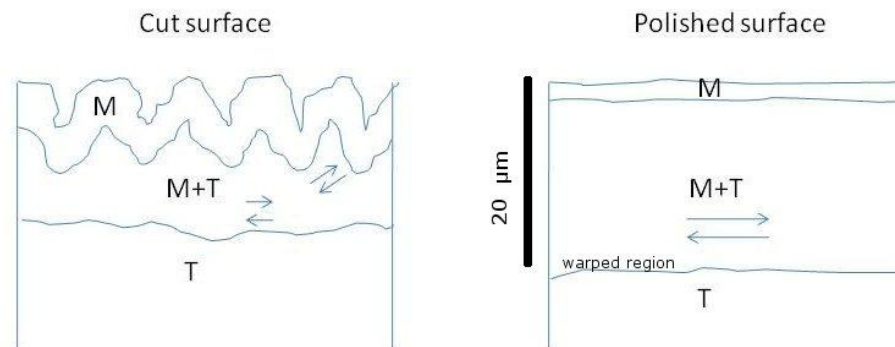
Figure 1.5 Suggested explanation for the discord reported in the article by Wada and Yokoyama (1999).

A reduction after annealing of the crack size of an indentation has been reported (Ho et al. 2009). This study produces Vickers indentation of the surface with a load of 300 N. These indentations create a crack in the corners of the footprint. The biaxial strength has been measured for samples that have been: Ground + Indented (GI); Ground + Indented + Annealed (GIA); Ground + Annealed + Indented (GAI). The strength is clearly greater for those samples whose last treatment has been annealed in comparison to those whose last treatment has been indentation. For this reason, this article concludes that the crack size has been reduced with the annealing. There is a healing effect. However, the stress state around the indentation is also important. It is known that an indentation produces plastic deformation that generates a tensile residual stress around it. This tensile residual stress reduces the strength of the samples, it is clear that an annealing treatment that alleviates the tensile residual stress would increase the strength of the sample. In this article it is apparently deduced that the increase of the strength after annealing is due to a reduction of the crack size and, at least in the article, the effect of the residual stress on this behaviour is not discussed. The reduction of the crack size after annealing is probably right, since it has been reported previously, but it is probably true, as well, that the residual stress around the crack plays an important role in the strength.

1.2.8 *Contact pressure and film thickness in spherical concentrated contacts.*

Recurrent topics in the tribological study of ceramic material used in ball bearings are the contact pressure, the lubricant film thickness and the lubrication regime. To calculate the contact pressure between two balls is necessary to take into account that the balls are being deformed with the contact pressure. To calculate the film thickness of the contact it is necessary to take into account both, the deformation of the balls and the pressure. To define the lubrication regime it is necessary to calculate the film thickness and to know the roughness of the surface. In turn, the roughness of the surface causes the change of contact pressure locally because of asperity contact. To address all these difficulties, there are several approximations of these parameters that have been extensively used over time. For contact pressure the Hertz's theory is used here while for film thickness, Hamrock and Dowson empirical formulae is used (Hamrock and Dowson 1981).

Hertz's theory comes from nineteenth century and was published originally in German (Hertz 1881). It assumes that the material is perfectly elastic, the force is only normal to the contact, the contact area is very small in comparison with the size of the solids that are at rest and in equilibrium, and the roughness effect is negligible. Hertz calculated the solution for elliptical contact. In this research, only the solution for contact between spheres is presented. Before calculating the contact area and the contact pressure it is necessary to calculate the reduced radius and the reduced elastic modulus. The reduced radius is given by Equation 1.1. The reduced elastic modulus is given by Equation 1.2. (Stachowiak and Batchelor 2001)

$$\frac{1}{R'} = \frac{2}{R_A} + \frac{2}{R_B}$$

Equation 1.1

where R' is the reduced radius, R_A and R_B are the radii of the two spheres.

$$\frac{1}{E'} = \frac{1}{2}\left[\frac{1-v_A^2}{E_A} + \frac{1-v_B^2}{E_B}\right]$$

Equation 1.2

where E' is the reduced elastic modulus, E_A and E_B are the elastic moduli of the two spheres, and ν_A and ν_B are the Poisson's ratios of the spheres.

Once the reduced parameters are defined, the contact radius and the contact pressure are given by Equation 1.3 and Equation 1.4 respectively (Stachowiak and Batchelor 2001).

$$a = \left(\frac{3WR'}{E'}\right)^{1/3}$$ **Equation 1.3**

$$p_{max} = \frac{3W}{2\pi a^2}$$ **Equation 1.4**

where a is the contact radius, W is the normal load and p_{max} is the maximum contact pressure. In the modified four ball machine, the load applied by the machine is distributed among three spheres with an angle of 35.3°. Then, the normal load (W) must be calculated taking into account this.

Hamrock and Dowson (1981) derived formulae numerically for the minimum film thickness and central film thickness of lubricant in the contact area . They measured the film thickness and fitted the results with an equation. Equation 1.5 gives the minimum film thickness according to Hamrock and Dowson (Stachowiak and Batchelor 2001).

$$\frac{h_0}{R'} = 3.63\left(\frac{U\eta_0}{E'R'}\right)^{0.68}(\alpha E')^{0.49}\left(\frac{W}{E'R'^2}\right)^{-0.073}\left(1 - e^{-0.68k}\right)$$ **Equation 1.5**

where h_0 is the minimum film thickness, U is the average entraining surface velocity, η_0 is the viscosity of the lubricant, α is the pressure-viscosity coefficient and k is the ellipticity of the contact. In this case (between two spheres): $k = 1$.

Finally, it is possible to define different lubrication regimes. The lubrication regime is a classification that can predict the type of wear and contact that exists between two bodies with roughness. According to the value of the relation between the minimum film thickness and the roughness, the existence of wear can be

predicted. For such relation the film parameter is defined according to Equation 1.6 (Stachowiak and Batchelor 2001). For values of the film parameter greater than 4, full separation of surfaces, elastohydrodynamic regime and no wear can be expected.

$$\lambda = \frac{h_0}{\left(\sigma_A{}^2 + \sigma_B{}^2\right)^{0.5}}$$

Equation 1.6

where λ is the film parameter, and σ_A and σ_B are the RMS surface roughness of the balls. Zaretsky summarizes these and other parameter and models in a report (Zaretsky 1990).

1.2.9   Research questions

The scope of this investigation is concerned with experimental and theoretical analysis of cavitation erosion in ceramics. Three types of technical ceramics are considered in relation to tribological applications. The main research questions are therefore:

- Understand the mechanisms of cavitation erosion and plastic deformation of silicon nitride, zirconia, and alumina.

- Understand the relationship of phase transformation of zirconia and cavitation erosion.

- Explain the existence of ring shape cavitation cluster found experimentally for the chosen set up.

Chapter 2 Experimental Methodology

2.1 Experimental procedure for cavitation erosion.

The testing methodology for cavitation erosion is based on the standard ASTM G32-03 (2003). This standard defines the method for testing cavitation erosion in brittle materials also referred as "stationary specimen method". The normal procedure to test samples as metals is to attach them to the tip of the probe. The "stationary specimen method" is used when the sample cannot be machined in order to be screwed into the tip of the probe. Brittle materials, such as ceramics, cannot be easily machined to shape a screw on them. For this reason, another approach is used. In the "stationary specimen method" a flat sample is located in front of the tip. However, in this research most of the samples are balls. For that reason, it was considered the use of balls instead of flat samples, but there are several pitfalls when a ball is used that are summarized here:

- A ball is more difficult to locate under the tip. Not only the gap between the ball and the probe tip has to be controlled, also, the location of the highest point of the ball respect to the centre of the probe. Otherwise the movement of the fluid would change dramatically.

- A ball is more difficult to be examined in the optical microscope and in the 3D profilometer. Since the surface presents a changing slope and part of it goes out of the depth of field.

- The ball has less number of references within its geometry. It could be difficult to change the erosion location or to remove and relocate the sample during the erosion process.

- The cavitation field between the ball and the tip is more unpredictable since it is not an easy geometry of a thin film. The repeatability would be smaller.

For these reasons, a flat sample is used here. The flat sample allows easy examination in the microscope, easy relocation of the sample under the probe tip and the cavitation field is produced in a thin layer that is easier to control and study.

The flat sample is positioned in the water bath with a vice press, that is placed on the bottom of a plastic box. A plastic box is chosen because the bottom of the box is flexible and when supporting the vice press with an extra wooden board base underneath of the plastic box, the gap between the sample and the probe tip is very stable (Figure 2.1). The use of a glass beaker, that has no flat bottom, may make difficult this operation. Furthermore, the glassy beaker may be broken with the constant location and removing of a heavy metal vice press.

The methodology followed in this report has one difference in relation to the standard. The standard defines a probe diameter of 15.9 mm while in these experiments the probe diameter is 5 mm because it creates a slow damage rate that is useful to study the mechanism of erosion. Besides, this geometry creates a pattern of damage that allows looking into regions with different damage grade. On the other hand, this geometry chosen does not present the magnification reported by Moussatov et al. (2005), because the small size is not big enough to create acoustic resonance. The Figure 2.1 shows the test assembly. The gap between the probe and the sample is 0.5 mm and the specimens are flat.
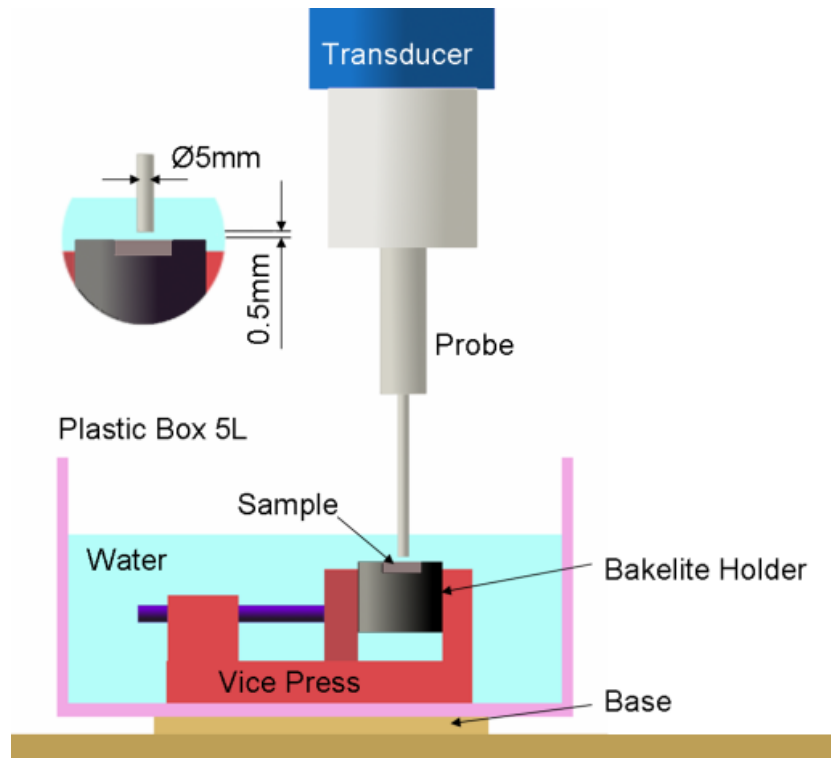
Figure 2.1 Cavitation erosion test assembly.

An ultrasonic piezoelectric transducer is used, this transducer oscillates at the frequency of 20 kHz and the amplitude of the probe tip is adjustable. The electric working power of the piezoelectric is measured. The water temperature is also measured.

Optical microscope micrographs are taken at various cavitation exposure times from 15 seconds to 180 minutes. These micrographs are always taken of the same place in the sample. With this process, a record of the surface along the cavitation erosion in early stages can be made. Micrographs with polarizing filter are useful to note the small initial damage on the surface, because any small change in the slope of the surface is visible with the filter and because damage and /or plastic deformation will create a slope. Micrographs without polarizing filter are useful to note the cracks and material loss.

A Profiler Interferometer is used to measure the damage on the surface of the samples at different stages. The measurements are made for the sample area corresponding to the centre of the cavitation damage (centre corresponding to the

probe). Measurements of the pseudoplastic deformation pits are also made. Further, SEM observation of the damaged surface is carried out. Dye penetrant inspection is used in order to understand the relation between cracks and pseudoplastic deformation. However, no crack is visible with the dye penetrant inspection.

2.1.1 *Location of the samples and the ultrasonic horn*

In order to monitor the erosion process of the samples, microphotographs are taken at different times of the erosion process. To do that, it is necessary to remove the sample from the water bath and to replace it in the same position with respect to the ultrasonic horn. For such a task the use of geometrical references is employed (Figure 2.2). The sample is fixed in a holder that is moulded with Bakelite. Also this holder is used to polish the sample with diamond slurry in a polishing machine. Then several notches are cut in the edge of the Bakelite holder. These notches help to orientate the sample in the microscope and are used to locate an acetate sheet on the surface of the sample. The acetate sheet thickness is smaller than 0.5 mm to allow free movement of the horn over the surface of the sample when the acetate sheet is onto the surface. The acetate sheet is cut with the same shape as the holder and has several lines, made with a permanent marker, that are coincident with the notches. The notches are highlighted with a corrector pen because of its white colour that has a clear contrast with the dark colour of the Bakelite holder.

When the samples are prepared with their corresponding acetate sheet, a suitable place on the surface of the sample is looked for on the microscope. This place may have some polishing line or polishing defect useful as a reference. Also, in the border of the visual field it may have some defect or a scratch made with a metal tip. This helps to locate the sample in the microscope for a quick photographic monitoring process. As the visual field is bigger than the field of the photo camera installed in the microscope, the presence of metal debris does not appear in the micrographs. Once the area is chosen, a drop of ink is put in the middle of the image from the camera with a marker and with help of a close diaphragm. It is possible to check if the drop is in the middle of the image through removing the sample from the microscope and replacing it as it would be made in the experimentation process. If the drop of ink is in the middle of the image, it allows a quick shooting process.
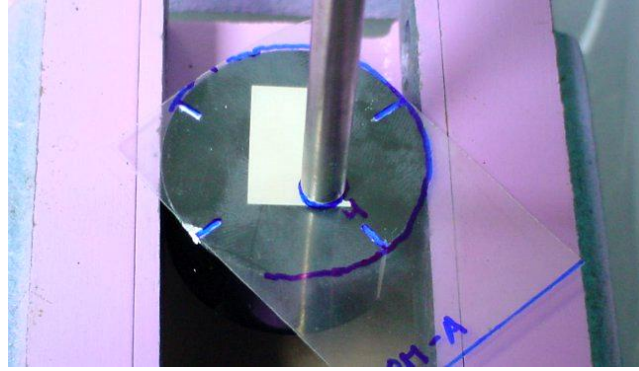
Figure 2.2 Acetate sheet and sample.

The acetate sheet is transparent. It is located onto the sample with the orientation defined by the notches and another point is marked with ink, coinciding with the drop of ink of the sample surface. Then the centre of the eroded surface is pointed on the acetate sheet that is located on the tip of the horn. The horn has machined lines and the centre of the horn is clear. A circle with the same diameter as the horn is draw with a permanent marker on the acetate sheet making sure the centre of the circle is the point already marked on the acetate sheet. Using the minimum magnification objective from the microscope it is possible to check the centre of the eroded surface on the sample and the point and circle of the acetate sheet.

Finally, the set up of the ultrasonic horn for the experiment is made in this way. The sample is cleaned and located horizontally in the vice press that is soaked in the water bath. With help of a 0.5 mm gauge, the ultrasonic horn is located vertically over the sample with that gap. Then, the acetate sheet is slipped between the sample and the horn. It is orientated and located with help of the notches. Then, the base of the laboratory holder used to keep the horn is moved a small amount until the circle is covered equally from all the sides. The acetate is removed.

This methodology ensures that: (1) erosion process can be interrupted, (2) that the sample can be extracted and micrographs can be taken, and (3) that the sample can be replaced, and the erosion process can be carried out as if it would have never been stopped.

The record of micrographs along the erosion process allows monitoring the damage and the detection of small changes. To do this, an image process consisting on the translation and rotation of the image with image software, in order to create a movie of the surface, where the surface remains fixed, is developed. The result of this is visible in Appendix A, where some frames of the footage are presented. This allows the identification of pits on the surface. Also, with the same image software, the use of layers allows the comparison of two layers of the same image. One layers ha been transformed in only black and white pixels, with the use of contrast and brightness, while the other layer remains in its original state. The comparison of the two layers allows checking that the black pixels correspond to places where the original surface is lost. In this way it is possible to measure the surface loss.

2.2 Experimental procedure for detection of phase transformation in zirconia.

The phase transformation of zirconia may be induced by the following strategies: Cavitation erosion, polishing, lapping, indentation and ageing. Also, the ageing process may be suppressed by soaking in grease since it may prevent the presence of water.

The phase transformation can be detected by: optical microscopy using polarizing filter; profiler interferometer to detect the increase of volume of transformed grains converted into monoclinic phase; and by means of X-ray diffraction. Different phases have different interatomic plane distances giving different X-ray diffraction angles.

The type of X-ray used here is monochromatic Cu K alpha radiation (1.5418 Armstrong). The scanned angle range is from 26° to 32°. It is expected to get a peak of tetragonal at around 30.3° and two peaks of monoclinic at 28.5° and 31.5° (Ho et al. 2009; Kosmac et al. 1999; Wada and Yokoyama 1999).

The irradiating volume depends on the collimator chosen. In this case the irradiated volume is approximately a regular hexahedron of 1.5 mm x 1 mm x 0.01 mm. This

volume allows the measurement of the diffraction angle of the surface region that is eroded by cavitation exposure.

2.3 Experimental procedure for rolling contact and lapping.

In order to understand the mechanical performance of the ceramics, rolling contact and lapping wear experiments are carried out. Rolling contact is used to produce extreme high contact pressure and to study the existence of plastic deformation at very high loads. Lapping is used in order to change the surface state of the balls through the third body abrasion produced by the diamond slurry.

Rolling contact experiments are performed in a Plint TE92 rotary tribometer that complies the standard IP 300 of rolling contact. The spindle of the tribometer holds a ball that is pressed against other three balls that can roll in a cup (Figure 2.3). The speed and the load are controlled from a computer. The machine automatically stops when the piezoelectric attached to it detects a vibration more intense than a threshold and for a period of time longer than a reference time. This vibration threshold and reference time can be adjusted with potentiometers. This strategy allows the user to automatically stop the machine when a failure is produced on the track of the upper ball or on the surface of the lower balls.

Figure 2.3 Rolling contact set up.

The lapping machine used here is an eccentric lapping machine that was developed by Kang and Hadfield (2001a). The lower plate has an eccentric groove where a batch of balls is placed and pressed by the upper plate by means of a spring (Figure 2.4). The lower plate turns. The load is regulated by a screw. The lapping machine is used with very light load and speed in order to produce a slight damage on the surface that keeps parts of the surface undamaged.
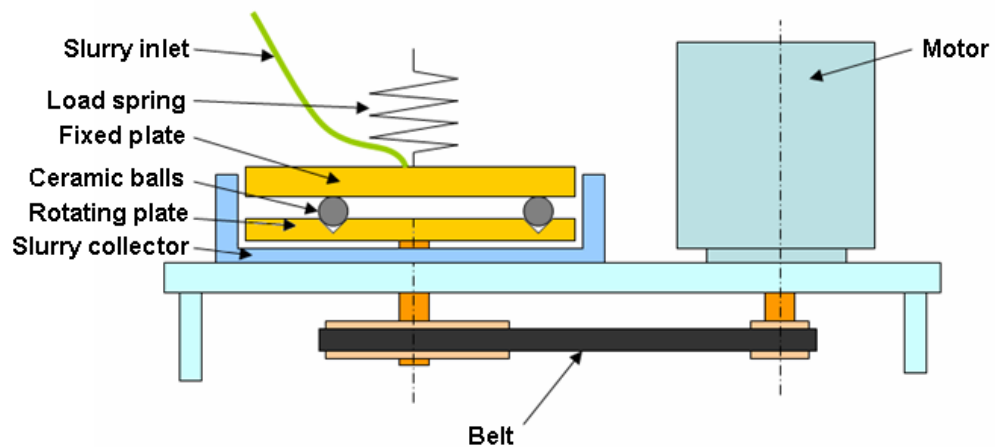
Figure 2.4 Lapping machine.

2.4 Sample materials.

The samples materials are commercially available ceramics. The ceramics chosen are silicon nitride, zirconia and alumina. The selection of these ceramics is based on its use within rolling bearing elements and for tribological applications.

Silicon nitride sample materials come from commercially available bearing balls. Zirconia sample materials come from either bearing balls, milling balls or rods. The alumina material, used here as a reference, is provided by SKF in a form of almost pure alumina. Silicon nitride materials are bearing grade and they can be polished to "mirror" grade, with roughness of several nanometres. One of the zirconia materials that come from milling balls is difficult to polish since grain dislodging occurs. Zirconia materials have both magnesia or yttrium dioxide as additives. Table 2.1 gives typical values for silicon nitride, zirconia and alumina that can be found on the

internet (www.accuratus.com). Table 2.2 gives the mechanical properties of the samples used in this research. The data is from the manufacturer, from SKF or from direct measurements during this research.

Table 2.1. Typical values for technical ceramic materials (www.accuratus.com).

	Silicon Nitride	Zirconia	Alumina
Hardness (H_v)	1580 kg/mm^2	1200 kg/mm^2	1440 kg/mm^2
Elastic modulus	310 GPa	200 GPa	375 GPa
Poisson's ration	0.27	0.31	0.22
Density	3.3 g/cm^3	6.0 g/cm^3	3.9 g/cm^3
Fracture toughness	6.1 MPa√m	13 MPa√m	3.5 MPa√m

The material provided by SKF has been characterised using thermal etching and SEM by SKF Research and Development Company. The manufacturing process of silicon nitrides "A", "B", "C" and "D" has yielded a minimum presence of porosity. The grain size for the various materials is shown in Figure 2.5 to Figure 2.8. Silicon nitride "A" shows the finest average grain size, silicon nitride "B" and "C" are similar to each other and slightly coarser than material "A". Material "D" was the coarsest. As shown in Table 2.2 they show fairly similar hardness and toughness values, when measured using a Vickers hardness method, material "D" presenting slightly lower hardness and fracture indentation toughness.
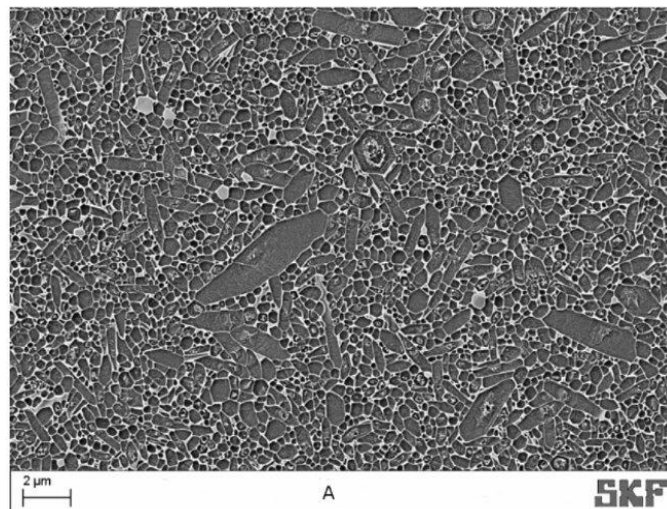
Figure 2.5 Microstructure of silicon nitride "A". Courtesy of SKF.
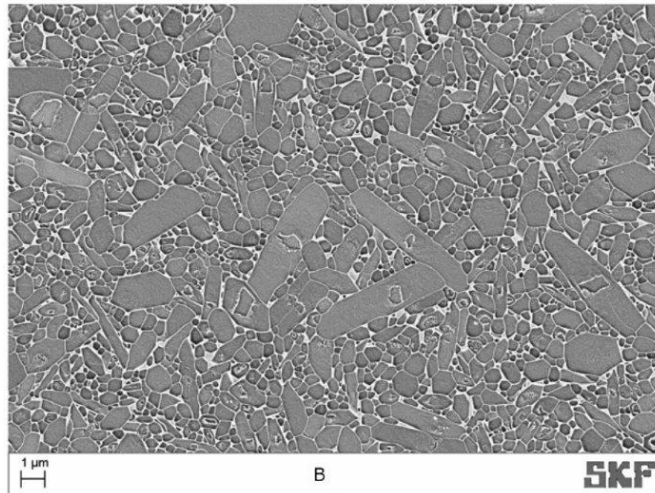
Figure 2.6 Microstructure of silicon nitride "B". Courtesy of SKF.
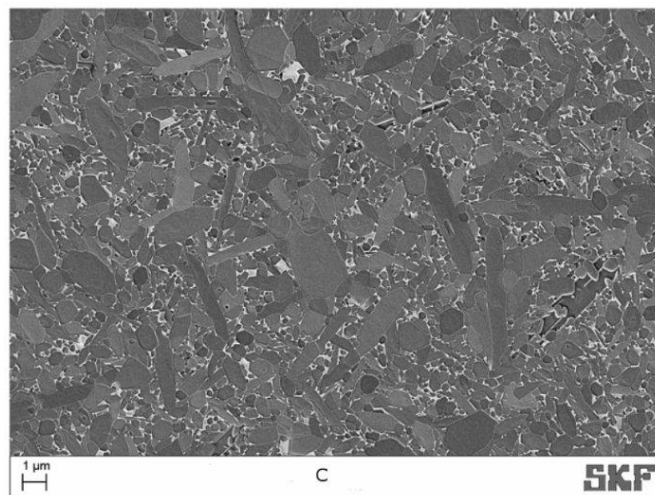
Figure 2.7 Microstructure of silicon nitride "C". Courtesy of SKF.
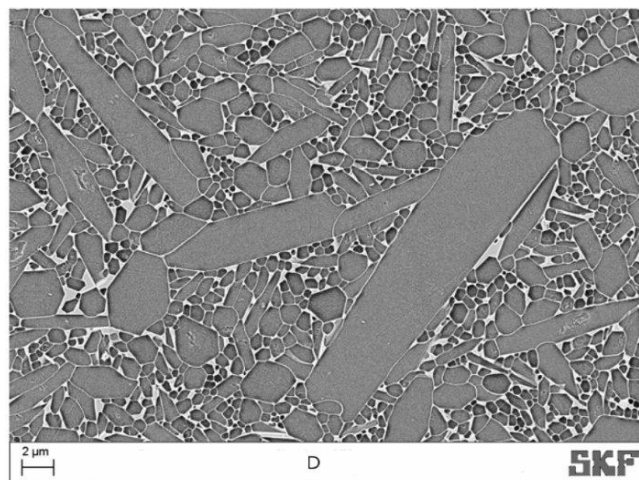
Figure 2.8 Microstructure of silicon nitride "D". Courtesy of SKF.

The alumina material "N" is a 99.9% purity commercially available pressure-less sintered alumina showing noticeable porosity with sizes up to 20 μm, and grain size up to 8μm. The grain size of alumina "N" is shown in Figure 2.10. The polished specimen for the erosion test presents more small break-outs than the genuine material porosity.
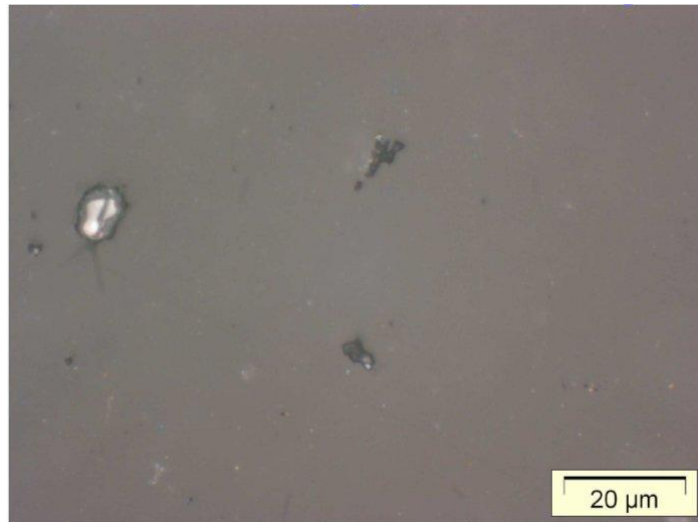
Figure 2.9. Polished alumina "N". Courtesy of SKF.
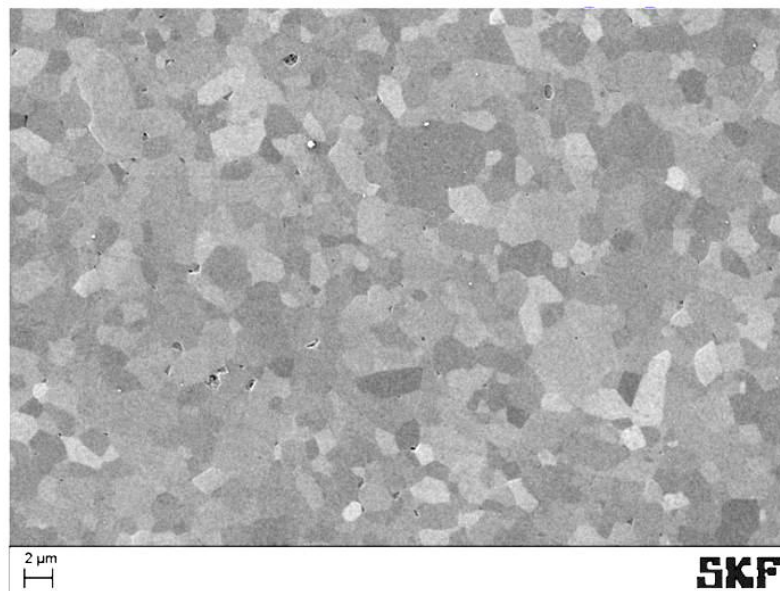
Figure 2.10. Microstructure of the alumina "N". Courtesy of SKF.

The zirconia material "H" is a commercially available Y-TZP material, manufactured by sintering, and hot isostatic pressing providing a fine structure, high density, with a fine distribution of very small alumina based secondary phase particles and a dual distribution of very fine zirconia grains (submicron or about 1μm) and few coarser zirconia grains (from 3 to 5 μm diameter), as shown in Figure 2.12.
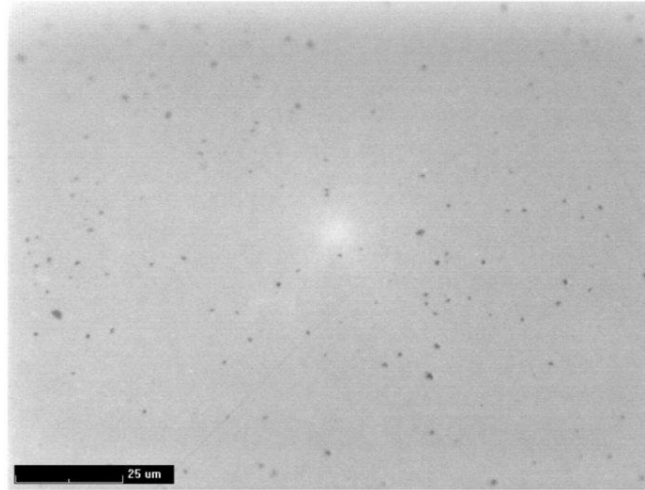
Figure 2.11 Polished zirconia "H" Y-TZP. Courtesy of SKF.
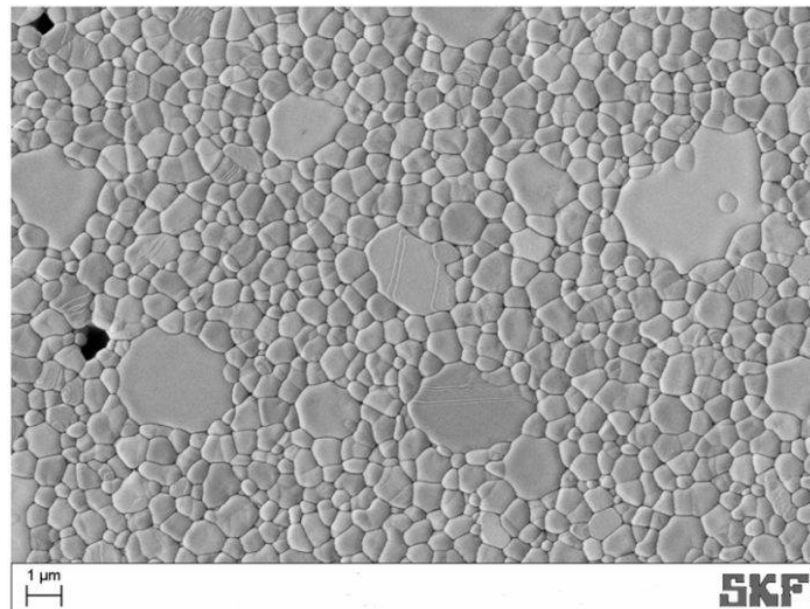
Figure 2.12 Thermally etched zirconia "H" Y-TZP. Courtesy of SKF.

The zirconia materials "I", "J", "K", "L" and "M" are commercial ceramic balls. Zirconia "I", "J" and "M" are bearing balls while zirconia "K" and "L" are milling balls for chemistry and forensic laboratories. Zirconia "I" is magnesia (magnesium oxide) partially stabilized, while zirconia "J" is yttria (yttrium oxide) partially stabilized. Zirconia "K" has an unknown but important percentage of hafnium oxide and five percent of yttria. Zirconia "L" has 3.2 percent of magnesia, this amount of magnesia should be enough to warranty a partially stabilized tetragonal phase but it is unknown if it has followed the heat treatment and quench process that allows the tetragonal phase to remain as metastable. Zirconia "K" and "L" are milling balls. The transformation toughening in a milling ball is not as important as in a bearing ball since they do not need to stand high loads in its working condition. The composition of zirconia "M" is unknown but it is a ball bearing for leisure industry.

Table 2.2. Mechanical properties of the samples.

Nickname	A	B	C	D	E	F	G
Material	Silicon Nitride	Silicon Nitride	Silicon Nitride	Silicon Nitride	Silicon Nitide	Silicon Nitride	Silicon Nitride
Type							
Manufacturer	Toshiba		Saint Gobain	NKE	Saint Gobain	Saint Gobain	Toshiba
Comercial Name	TLS	CXY	NUO	NTK	NBD-200	SN101C	TSN-03NH
Composition					MgO sintering aid	Y_2O_3; Al_2O_3 sintering aid	
Hardness kg/mm^2	[2] 1592 H_V10	[2] 1542 H_V10	[2] 1600 H_V10	[2] 1485 H_V10	[1] 1550 H_V10	[1] 1600 H_V10	[1] 1500 H_V20
Fracture indentation toughness MPa√m	[2] 7.02±0.10	[2] 6.9±0.30	[2] 7.3±0.20	[2] 6.23±0.05	[1] >5.5	[1] >6.5	[1] 7
Bending strength MPa	[2] 1174	[2] 956	[2] 1043	[2] 816	[1] >900	[1] >1000	[1] 1100
(Weibull modulus)	[2] 16.3	[2] 13.5	[2] 16.6	[2] 25	[1] >15	[1] >25	[1] 20
Elastic modulus GPa					[1] 320	[1] 310	[1] 310
Poisson's ratio					[1] 0.26	[1] 0.27	[1] 0.29
Density g/cm3							[1] 3.24

Table 2.2 (continuation).

Nickname	H	I	J	K	L	M	N
Material	Zirconia	Zirconia	Zirconia	Zirconia	Zirconia	Zirconia	Alumina
Type	YTZP	MgPSZ	YTZP				Pure
Manufacturer		Spheric Trafalgar	Shangai Unite Technology Co. LTD	Fritsch	Fritsch	Boca Bearing	
Comercial Name				55.0050.27	55.0100.27		
Composition		3% MgO	~% Y_2O_3	5% Y_2O_3; ~HfO_2	3.2% MgO		
Hardness kg/mm^2	[2] 1271 H_V10	[1] 80-84 H_{Ra}	1270	[1] 1290 H_V1	[1] 17Gpa Knoop (100g)	[1] 1250	[2] 1828 H_V10
Fracture indentation toughness MPa√m	[2] 10.51						[2] 3.77
Bending strength MPa (Weibull modulus)	[2] 1418 [2] 16.1						[2] 300 [2] 8.1
Elastic modulus GPa		[1] 200				[1] 211	
Poisson's ratio							
Compressive strength GPa		[1] 1.96					
Tensile strength GPa		[1] 0.41				[1] 5.48	
Density g/cm3				[1] 6.06	[1] 5.9	[1] 6.062	
		[2] measured by SKF		[1] measured by the manufacturer			

Chapter 3   Analytical study of the cavitation clusters

The experimental set up used in this research is slightly different to the experimental set up indicated in the standard (ASTM G32). As explained in section 2.1, the ultrasonic horn used here has a diameter of 5 mm while the standard has a diameter of 15.9 mm. The standard method produces an homogeneous erosion on a surface of similar diameter as the horn, as can be seen somewhere else (Hattori et al. 2008). With the horn diameter used here, the erosion pattern differs from the standard and it is not homogeneous in contrast with the standard methodology. It is evident that the selection of a small diameter probe has an enormous influence in the erosion of the sample. Hence, it is necessary a good understanding of this and its implications to the erosion test. The variations that the non homogeneous cavitation erosion pattern produces in the erosion of the sample are studied in detail. In this section, an explanation of the erosion pattern is given and its implications for tribology are discussed.

3.1.1   *Erosion pattern with 5 mm diameter ultrasonic horn.*

The erosion of the samples with the experimental set up used in this research (section 2.1) shows a concentration of erosion in two particular regions. One region appears at the centre of the sample with a circular shape. The other region shows a ring shape surrounding the former region. This erosion distribution is presented on the specimen surface as well as on the horn tip. Figure 3.1 shows the distribution of severe erosion on the horn tip after 10 hours of cavitation exposure and on a silicon nitride sample after 3 hours. The erosion pattern is related to the existence of two cavitation clusters. These clusters are shown in Figure 3.2. The present section explains the existence of this pattern and examines its application to cavitation erosion resistance tests.
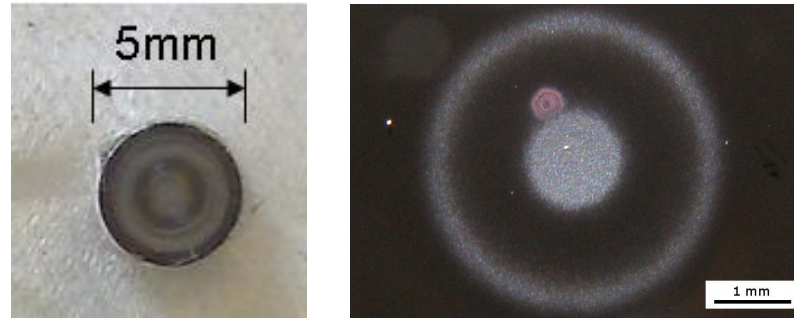
Figure 3.1 Erosion pattern on the horn and on silicon nitride "G" after 10 and 3 hours of cavitation exposure respectively.
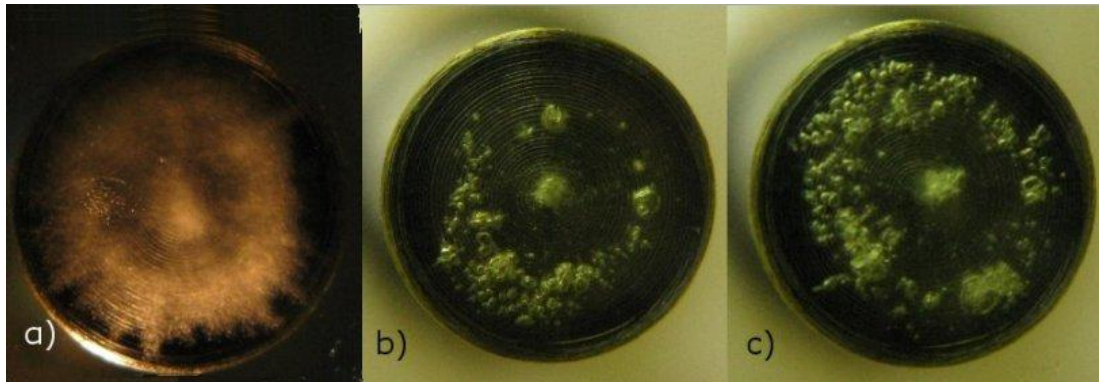
Figure 3.2 Clusters with 5 mm diameter horn. a) is a low speed photograph of the bubbles with glass sample; b) and c) are high speed photographs of the bubbles with glass sample.

3.1.2 *Hydrodynamic approach versus acoustic approach*

During the last decade several studies considered the morphology of the bubble field under ultrasonic cavitation. These studies present two types of experimental set-up; first set-up is without a specimen in front of the horn tip (Campos-Pozuelo et al. 2005; Moussatov et al. 2003) while the second set-up considers a specimen in front of the horn tip (Moussatov et al. 2005). According to the experimental set-up last study is relevant in the present study but it cannot explain the cavitation ring region. The model proposed there is carried out for a normalised radii and gaps greater than those in the present study. The normalisation is performed in respect to the wavelength corresponding to a speed of sound of 1490m/s in water. In the work of Moussatov et al. the normalised radii of the probe tip have values greater than 0.1

while in the present study the normalised radius is out of this range and corresponds to 0.03. Therefore, the work of Moussatov et al. cannot be used to explain the cavitation phenomena under the experimental set-up of the present study.

The study of Moussatov et al. does not consider the changes of the speed of sound with the proportion of bubbles in the liquid. This effect is addressed in (Silberman 1957; Wijngaar 1972; Wood 1941; Young 1999). Equation 3.1was proposed by Wood and can be used to calculate the speed of sound in the bubbly region (Wood 1941).

$$\frac{1}{c^2} = \frac{(1-\beta)^2}{c_f^{\,2}} + \frac{\beta^2}{c_g^{\,2}} + \frac{\rho_f \beta (1-\beta)}{p}$$
                                                                        Equation 3.1

where c is the speed of sound in the bubbly liquid, c_f is the speed of sound in the liquid, c_g is the speed of sound in the gas of the bubbles, p is the pressure, ρ_f is the density of the fluid and β is the proportion of volume occupied by gas.

A small proportion of gas leads to big changes of speed of sound. For example, for a bubble volume fraction of 0.6% the speed of sound is reduced from 1490m/s (without bubbles) to 131m/s (bubbly liquid). Moussatov et al. do not address the change of speed of sound; the results are valid when the proportion or distribution of cavities is small enough to keep the speed of sound constant. However, under the mentioned experimental conditions the fraction of bubbles is significant to alter the speed of sound. The bubbles are clearly visible and their volume fraction is greater than 0.6%. The present study addresses this phenomenon using a different approach and explains the existence of a cavitation ring region. Furthermore, it helps to understand the behaviour of cavity clusters in ultrasonic cavitation and it shows the significance of the fluid velocity in thin layers. This is made with the combination of fluid mechanics and analytical mechanics theories, from a hydrodynamic point of view.

3.1.3 *Measurement of the ring diameter*

A polished sample of aluminium is used during the measurement of the diameter of the cavitation ring region due to its resistance to corrosion and because it is easy to be polished. Also, the aluminium polished surface is easily damaged by cavitation due to its low hardness. This makes the experimentation faster than with other materials. The basic lay out of the experimental set up is described in section 2.1 but for the study of the clusters location, variations of the gap and the amplitude are used. The gaps go from 0.05 mm to 0.5 mm and the amplitudes go from 15 µm to 50 µm. Samples are exposed to cavitation erosion and the diameters of the ring region are measured using the following steps:

Step 1. Different micrographs are taken of the eroded part as shown in Figure 3.3.

Step 2. At this point two measurements are taken: the diameter of the external border (d_e) and the diameter of the internal border (d_i) of the cavitation ring erosion as shown in Figure 3.3.

Step 3. The effective diameter of each ring is calculated according to Equation 3.2.
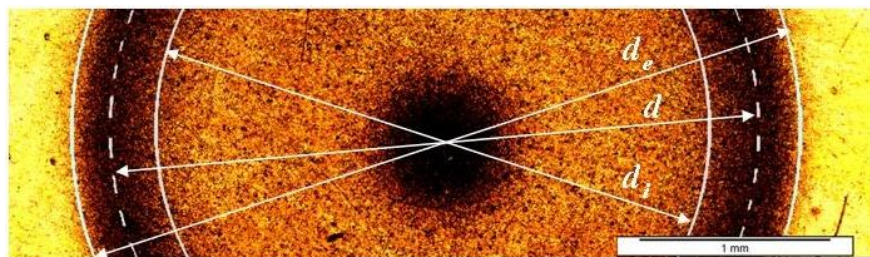
Figure 3.3. Cavitation erosion regions with 20µm of amplitude and 0.1mm of gap.

$$d = \sqrt{\frac{d_i{}^2 + d_e{}^2}{2}}$$ Equation 3.2

where d is the effective diameter of the cavitation ring region, d_i is the diameter of the internal edge of the cavitation ring region and d_e is the diameter of the external

edge of the cavitation ring region as explained before. This equation makes the area between d_i and d equal to the area between d and d_e.

A high degree of accuracy in results requires a large number of experiments. To characterise this phenomenon a total number of ninety experiments were performed. The diameter of the cavitation ring region was measured for each sample. These experiments were performed using a gap of 0.05mm, 0.1mm, 0.2mm, 0.3mm, 0.4mm, 0.5mm and amplitude of 15µm, 20µm, 30µm, 40µm and 50µm. The measured diameters are represented in Table 3.1 and Figure 3.4. as a function of the gap and the amplitude. Data from experiments is fitted using a 2nd order polynomial fit (parabolic regression) as shown in dashed lines in Figure 3.4.
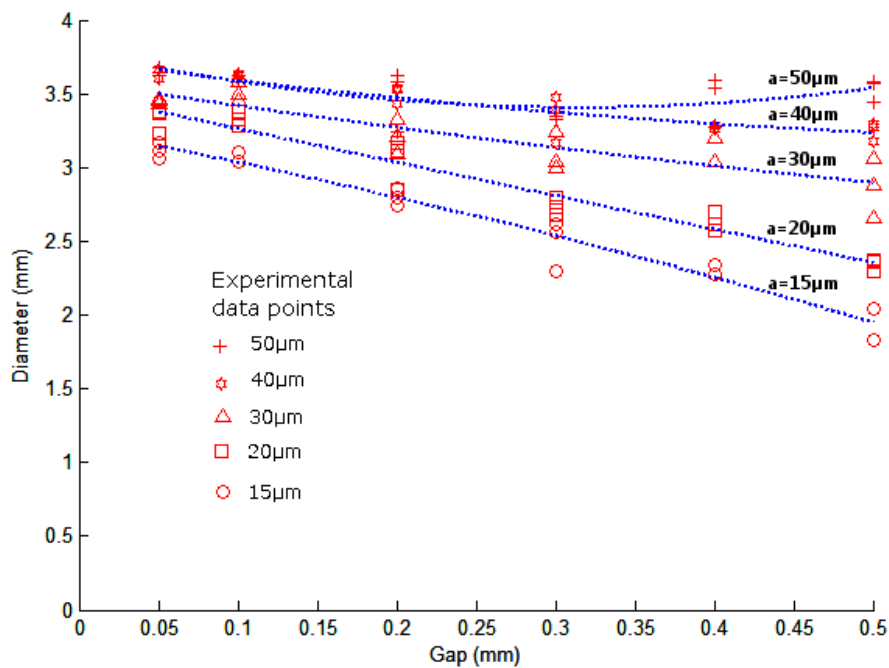
Figure 3.4. Diameter of the ring region for different gaps and amplitudes. Experimental data.

Table 3.1 Range of experimentally measured ring region diameter (mm).

Amplitude	Gap					
	0.05 mm	0.10 mm	0.20 mm	0.30 mm	0.40 mm	0.50 mm
50 μm	3.61-3.68	3.60-3.63	3.23-3.63	3.33-3.55	3.27-3.59	3.44-3.58
40 μm	3.60-3.67	3.59-3.63	3.43-3.55	3.16-3.48	3.26-3.28	3.18-3.30
30 μm	3.43-3.47	3.45-3.58	3.09-3.33	2.99-3.25	3.04-3.20	2.65-3.10
20 μm	3.23-3.38	3.28-3.39	2.85-3.17	2.67-2.80	2.56-2.70	2.29-2.38
15 μm	3.05-3.17	3.04-3.11	2.74-2.86	2.29-2.62	2.27-2.35	1.82-2.05

3.1.4 *Considerations and summary of the suggested model to simulate the clusters*

As shown in the previous section, the diameter of the cavitation ring regions varies with the gap and the amplitude. The variation of the diameter with the amplitude suggests that the acoustic method is not suitable to address the problem. The resonance of the acoustic waves depends on the geometry of the system and its boundaries rather than on the amplitude of the excitation. Also the variation of the speed of sound with the bubble content makes the analysis difficult as explained in section 3.1.2. Hence a hydrodynamic model is used, where the geometry of the ring is a constraint and it is evaluated with energy principles, specifically Hamilton's principle from analytical mechanics theory.

After experimental observations the proposed model is based on the assumption that the clusters remain stable and correspond to the erosion regions shown in Figure 3.1. This is a reasonable assumption as this behaviour was observed changing the metallic sample for a glass one (Figure 3.2). This piece of glass allows direct observation of the two cavity clusters; one is clearly seen in the centre of the tip and another in the zone of the ring region of cavitation erosion.

The proposed model assumes that the cavities or bubbles are changing their size in the same frequency as the perturbation produced by the horn. This assumption is consistent with other studies which state that the cavities are oscillating in a stable situation until some of them grow and collapse (Gogate and Pandit 2004; Young

1999). The present study assumes that there are only cavities in the central and ring region zone. The rest of the space is liquid without cavities. This assumption agrees with the experiments made with a piece of glass as sample. Another simplification is that the density is much smaller in the region of the cavities than in the liquid region, therefore the region of the cavities is not taken into account for momentum conservation and kinetic energy calculus. The phenomenon of collapsing is neglected in the calculus for the liquid movement.

The proposed model assumes the liquid density is constant, it has no change of volume; conversely, the cavities region is the one which changes the volume to adapt the system to the changes of volume produced by the horn movement. Therefore the movement of the liquid (Figure 3.5) is as it follows: when the horn goes down, the volume of the central region of cavities and the ring region of cavities decrease. When the horn goes up, the regions of cavities increase their volume. Furthermore, it is assumed the main component of the velocity of the fluid is radial; no other component is taken into account.

An analytical model to explain the existence and the size of the cavitation ring region is created. It is based in the geometry explained in Figure 3.5 that represents a cut in the axis of the horn. The analytical model is developed according to the following steps:

1. The radius of the ring region is a parameter with a value in the range of 0 to 2.5 mm. It also remains stable for a given gap and amplitude. The radius is the generalised coordinate for application of Hamilton's principle.

2. The velocity field inside the thin film liquid is created according to Figure 3.5.

3. The energy and power to move the liquid is calculated using numerical methods.

4. The Hamilton's principle is used to decide which radius of the ring region is valid.

5. The solution of the system is calculated using the previous radius value.
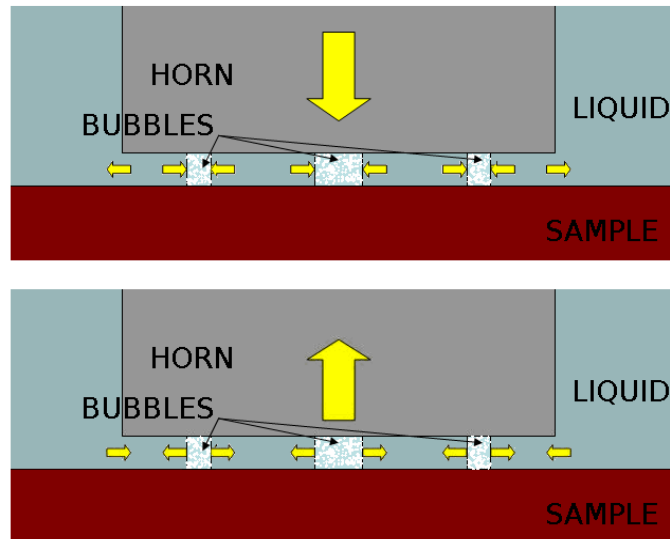
Figure 3.5 Movement of the cavities regions and surrounding liquid assumed in this study.

The main assumption is the two liquid and two bubbly regions of the system. The liquid regions are in two places, one between the central region and the ring region and another one outside the ring region. The liquid region outside the ring region is defined in section 3.1.6. The mass of the bubbly region is neglected in comparison to the mass of the liquid region. This mass is not taken into account for kinetic energy calculation.

3.1.5 *Fluid velocity in liquid region "1".*

Firstly, the liquid region between the central region and the ring region is modelled. This region is called "1" in Figure 3.6. The volume of liquid is constant and the bubbly region absorbs the change of volume. The volume of liquid is calculated when the distance between the sample and the horn is minimal, then the volume of

the bubbly region is zero. The movement of the horn is assumed to be a sine wave and the distance between horn and sample follows the following equation:
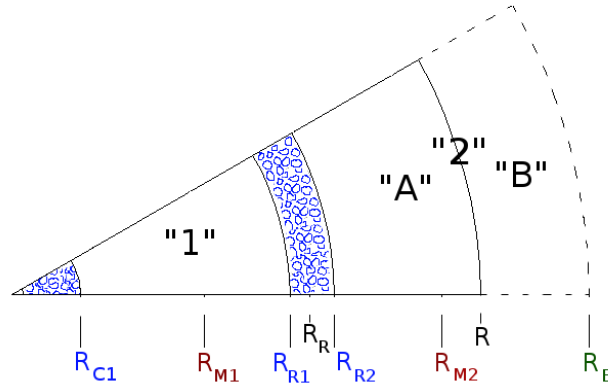
$$h(t) = h_0 + \frac{a}{2}\sin(2\pi f t)$$ Equation 3.3

Figure 3.6 Sector showing the two liquid regions analysed.

This region between the central region and the ring region has not any radial force resultant due to it being surrounded by two bubbly regions. The momentum along the radial direction for this region should be zero. With this simplification it is possible to calculate the fluid velocity in this region. As there is cylindrical symmetry only a sector of the disk is used (Figure 3.6). The velocity is given as a function of the time and the radius using Navier-Stokes in integral and cylindrical form for the conservation of mass and for the radial momentum (Liñán Martínez 1967). Equation 3.4 shows the fluid velocity,

$$v(r,t) = \frac{(R_{M1}{}^2 - r^2)h'}{2rh}$$ Equation 3.4

R_{M1} is given by Equation 3.5 and it is such that momentum is zero. The fluid velocity is zero at $r = R_{M1}$.

$$R_{M1} = \frac{R_R}{\sqrt{3}}$$ Equation 3.5

This velocity is valid for this liquid region between these two radii, R_{C1} and R_{R1}. The radii are calculated using conservation of mass and are given by Equation 3.6 and Equation 3.7.

$$R_{C1}(t) = R_{M1}\sqrt{1 - \frac{h_0 - a/2}{h(t)}}$$ Equation 3.6

$$R_{R1}(t) = R_{M1}\sqrt{1 + 2\frac{h_0 - a/2}{h(t)}}$$ Equation 3.7

3.1.6 *Fluid velocity in liquid region "2".*

Secondly, the liquid region outside of the ring region is modelled. This region has a large extension and it contains all the fluid space around the sample and the horn. This liquid region is modelled by the region called "2" in Figure 3.6. This region "2" is reduced to two zones, zone "A" below the horn and zone "B" around the horn. This reduction of the volume of the fluid space is a simplification. Therefore, the volume of zone "B" is the volume inside of these limits: the external radius R_E, the radius of the horn R and height h_0. Outside of this ring the fluid velocity is neglected in the calculations. This simplification tries to take into account the effect of the movement of the liquid out of the thin layer and the influence of the interface phenomenon that happens between the region below the horn and the rest of the liquid. It should be noted that in the real system the movement around the horn forms a vortex. This vortex is fed by the combination of two effects: first, when the horn is going down, the direction of the fluid velocity is approximately radial; and second, when the horn is going up, the liquid is going into the space between the sample and the horn from different directions as shown in Figure 3.7. The fluid velocity of this region is assumed to be radial in order to simplify the calculations.
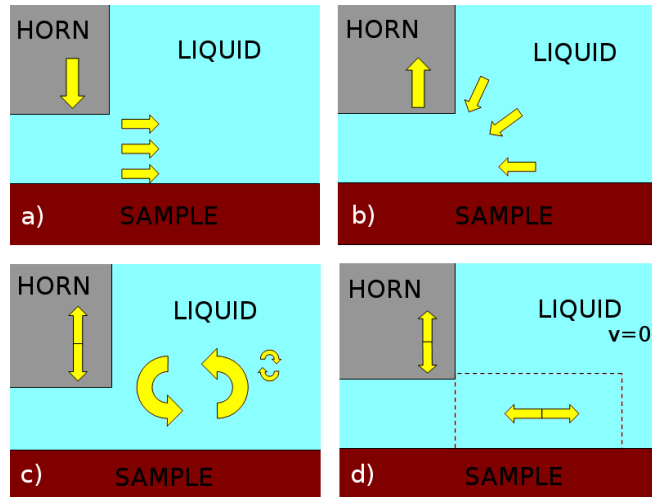
Figure 3.7 Fluid velocity around the horn when a) the horn is going down, b) the horn is going up c) combination of both movements and d) simplification.

The external radius R_E is calculated with the next supposition. It is proportional to the kinetic energy of the fluid going out of the zone "A" when the fluid velocity is at its maximum. This is a strong simplification; otherwise, the calculation of the velocity field in this liquid region might become impractical. R_E is given by Equation 3.8.

$$R_E = R + k(v_M(R))^2 \qquad \text{Equation 3.8}$$

Where k is a parameter function of the amplitude that is fitted with the experimental data.

The velocity in zone "A" is given by Equation 3.9 and is calculated in a similar way as Equation 3.5.

$$v(r,t) = \frac{(R_{M2}^2 - r^2)h'}{2rh} \qquad \text{Equation 3.9}$$

The velocity in zone "B" is calculated with the mass conservation equation from Navier-Stokes and is given by Equation 3.10.

$$v(r,t) = \frac{(R_{M2}^2 - R^2)h'}{2rh} \qquad \text{Equation 3.10}$$

R_{M2} is calculated with the same assumptions as R_{M1}. Consequently, it is such that the momentum in the radial direction is zero in the liquid region "2" and is given by Equation 3.11.

$$R_{M2} = \sqrt{\dfrac{R^2 R_E - \dfrac{2R_E{}^3 + R_R{}^3}{3}}{(R_E - R_R)}}$$ Equation 3.11

The limits of zone "A" are R_{R2} and R . The limits of zone "B" are R and R_E. R_{R2} is given by Equation 3.12 and obtained from mass conservation.

$$R_{R2} = \sqrt{R_{M2}{}^2 - (R_{M2}{}^2 - R_R{}^2)\dfrac{h_0 - a/2}{h}}$$ Equation 3.12

3.1.7 *Kinetic energy of the system.*

The kinetic energy of the system is calculated using the energy equation from Navier- Stokes in integral and cylindrical form (Liñán Martínez 1967). There are three different equations to calculate the fluid velocity in the system. Thus, three integrals are used. The kinetic energy of the system depends on the variable time (t), on the parameter radius of the cavitation ring region (R_R) and is given by Equation 3.13a.

$$E(t, R_R) = \frac{1}{2}\rho\left(\int_{R_{C1}}^{R_{R1}}\int_0^{2\pi}\int_0^{h(t)} v^2 \cdot r\,dr\,d\theta\,dz + \int_{R_{R2}}^{R}\int_0^{2\pi}\int_0^{h(t)} v^2 \cdot r\,dr\,d\theta\,dz + \int_{R}^{R_E}\int_0^{2\pi}\int_0^{h_0} v^2 \cdot r\,dr\,d\theta\,dz\right)$$ Equation 3.13a

An improvement of the calculus of the kinetic energy can be made introducing into the Equation 3.13a a parameter to take into account the turbulence. This parameter gives an idea of the intensity of turbulence, i, and is defined in Equation 3.14. $i = 1$ is for no turbulence and $i > 1$ is for turbulence. Equation 3.13a is transformed into Equation 3.13b. This parameter, intensity of turbulence, will be fitted with the experimental data.

$$E(t, R_R) = \frac{1}{2}\rho\left(\int_{R_{C1}}^{R_{R1}}\int_{0}^{2\pi}\int_{0}^{h(t)}(i \cdot v)^2 \, r dr d\theta dz + \int_{R_{R2}}^{R}\int_{0}^{2\pi}\int_{0}^{h(t)}(i \cdot v)^2 \, r dr d\theta dz + \int_{R}^{R_E}\int_{0}^{2\pi}\int_{0}^{h_0}(i \cdot v)^2 \, r dr d\theta dz\right)$$ Equation 3.13b

$$i = \frac{\sqrt{v_r^2 + v_\theta^2 + v_z^2}}{v}$$ Equation 3.14

The power is given by Equation 3.15.

$$W = \frac{d}{dt}E$$ Equation 3.15

Figure 3.8 shows the kinetic energy of the system depending on the time and on the whole range of the parameter R_R. There is a specific value of R_R for which the change of energy is minimal.
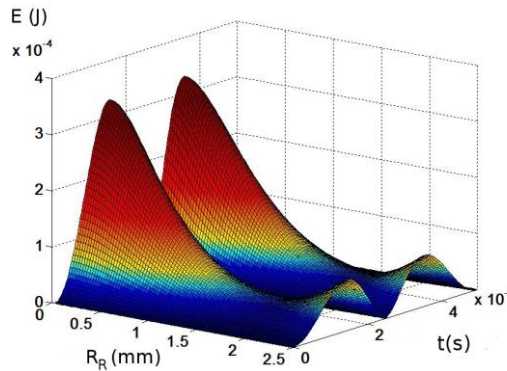
Figure 3.8 Kinetic energy of the system for the whole range of R_R.
Gap of 0.5 mm, amplitude of 50 μm, $k = 0.001$ and $i = 1$.

The value of energy and power is obtained using numerical methods. The selection and implementation of these numerical methods was made by Angel Torres Pérez. In order to calculate the fluid velocities (Equation 3.8, Equation 3.9 and Equation 3.11) in liquid region "2", the Gauss Newton algorithm is used. After solving the limits of the integrals, the integral equation that represents the kinetic energy (Equation 3.13b) is solved using the adaptive Simpson's rule.

3.1.8 *Hamilton's principle.*

According to analytical mechanics it is possible to define an integral of the kinetic energy along a curve of the generalised coordinates from t_0 to t_1, initial and finish time of a period respectively. Equation 3.16 shows this integral.

$$I = \int_C E \, dt$$ Equation 3.16

For this case, the integral from Hamilton's principle (Equation 3.16) becomes the following equation:

$$I = \int_C \frac{1}{2}\rho \left[\int_{\frac{R_R}{\sqrt{3}}\sqrt{1-\frac{h_0-a/2}{h_0+\frac{a}{2}\sin(2\pi ft)}}}^{\frac{R_R}{\sqrt{3}}\sqrt{1+2\frac{h_0-a/2}{h_0+\frac{a}{2}\sin(2\pi ft)}}} \int_0^{2\pi} \int_0^{h_0+\frac{a}{2}\sin(2\pi ft)} \left(i \cdot \frac{\left((R_R/\sqrt{3})^2 - r^2\right)\left(a2\pi f\cos(2\pi ft)\right)}{2r\left(h_0+\frac{a}{2}\sin(2\pi ft)\right)} \right)^2 r\,dr\,d\theta\,dz + \right.$$

$$+ \int_{\sqrt{\left(\sqrt{\frac{R^2(R+k\cdot(v_M)^2)-\frac{2(R+k\cdot(v_M)^2)^3+R_R^3}{3}}{(R+k\cdot(v_M)^2)-R_R}}\right)^2 - \left(\left(\sqrt{\frac{R^2(R+k\cdot(v_M)^2)-\frac{2(R+k\cdot(v_M)^2)^3+R_R^3}{3}}{(R+k\cdot(v_M)^2)-R_R}}\right) - R_R^2\right)\frac{h_0-a/2}{h_0+\frac{a}{2}\sin(2\pi ft)}}}^{R} \int_0^{2\pi} \int_0^{h_0+\frac{a}{2}\sin(2\pi ft)} \left(i \cdot \frac{(R_{M2}{}^2 - r^2)(a2\pi f\cos(2\pi ft))}{2r(h_0+\frac{a}{2}\sin(2\pi ft))} \right)^2 r\,dr\,d\theta\,dz +$$

$$\left. + \int_R^{R+k(v_M)^2} \int_0^{2\pi} \int_0^{h_0} \left(i \cdot \frac{(R_{M2}{}^2 - R^2)(a2\pi f\cos(2\pi ft))}{2r(h_0+\frac{a}{2}\sin(2\pi ft))} \right)^2 r\,dr\,d\theta\,dz \right] dt$$

where R_{M2} and v_M are:

$$R_{M2} = \sqrt{\frac{R^2\left(R+k\left(\frac{(R_{M2}{}^2-R^2)a2\pi f}{2Rh_0}\right)^2\right) - \frac{2\left(R+k\left(\frac{(R_{M2}{}^2-R^2)a2\pi f}{2Rh_0}\right)^2\right)^3 + R_R^3}{3}}{\left(R+k\left(\frac{(R_{M2}{}^2-R^2)a2\pi f}{2Rh_0}\right)^2\right) - R_R}}$$

$$v_M = \frac{(R_{M2}{}^2 - R^2)a2\pi f}{2Rh_0}$$

51

The path C is a curve of generalised coordinates along the time. It is possible to define any other path that is very close to C with respect to the time. This new path is called $C1$. If the change of the integral between these two paths is zero, the path is a solution of the system (Prieto Alberca 1994).

$$\delta I = \int_C E dt - \int_{C1} E dt$$ Equation 3.17

When $\delta I = 0$, C is solution of the system.

In the present study, the system has only one generalised coordinate R_R. The chosen curve C is R_R constant. The solution for the value of R_R is given by Hamilton's principle. Figure 3.9 shows the value of I for different values of R_R. The value of R_R where I is minimal is the solution.
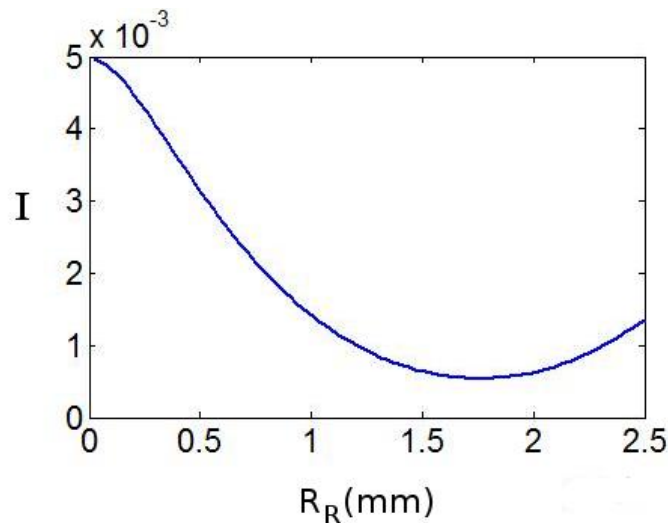
Figure 3.9 Integral value for Hamilton's principle. Gap of 0.5 mm, amplitude of 50 μm, $k = 0.001$ and $i = 1$.

 It is possible to put this value into the previous equations and then, it is possible to calculate the instant power of the system. Also, the average power of the system and the velocity field of the liquid can be calculated.

3.1.9 *Numerical results of the proposed model.*

Figure 3.10 shows the results of the model depending on different values of k. The value of k is important for the shape of the graph, when $k = 0$ means that the movement of the liquid outside of the layer between the horn and the sample is not taken into account. The value of k has been fitted manually due to the complexity of the model. Finally, $k = (3000 \cdot a)^3$ is taken as the best value as shown in Figure 3.10.
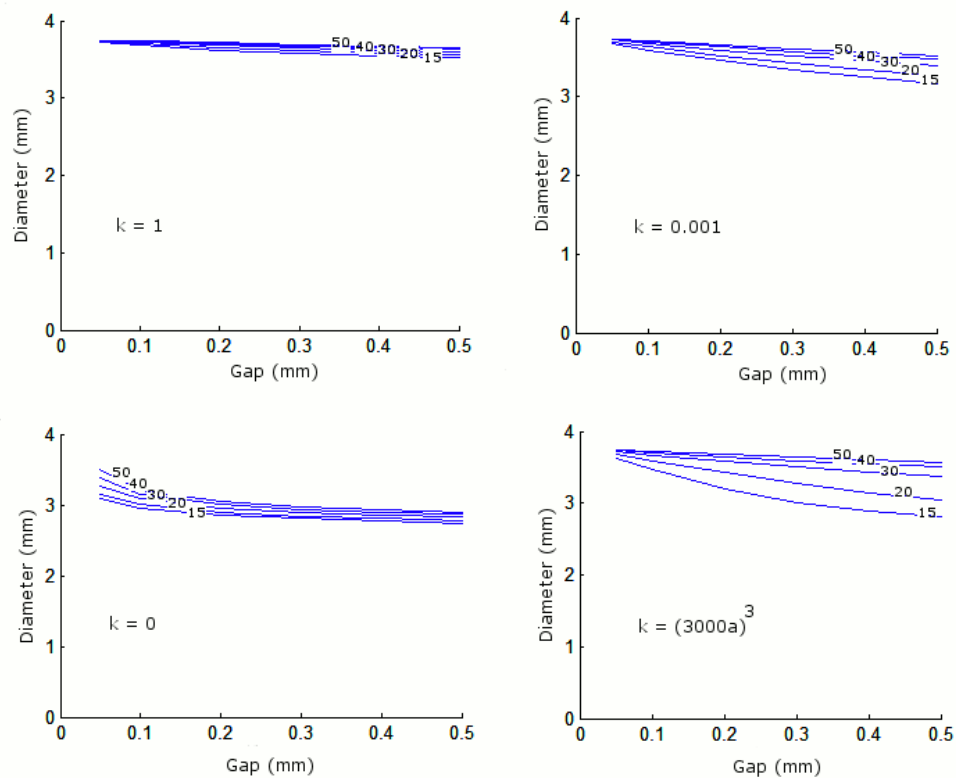
Figure 3.10 Cavitation ring diameter for different values of k. The amplitudes for each line from up to down are 50 µm, 40 µm, 30 µm, 20 µm and 15 µm.

Although the trends of the diameters represented in the last graph of Figure 3.10 are close to the trends of the experimental results, these values are higher than those from the experimental data represented in Figure 3.13. This is because the turbulence has not been taken into account in Figure 3.10. The value of the intensity of turbulence, i, that is used in Eq. 12b. for Figure 3.10 is $i = 1$. In order to fit the values of the diameters the intensity of turbulence, i, is manually fitted to $i = 1.4$ for

the region "1" and $i = 1$ for the region "2". The result is shown in Figure 3.11. The parameter "k" has a strong influence on the trends while the parameter "i" has a strong influence on the values of the diameters.
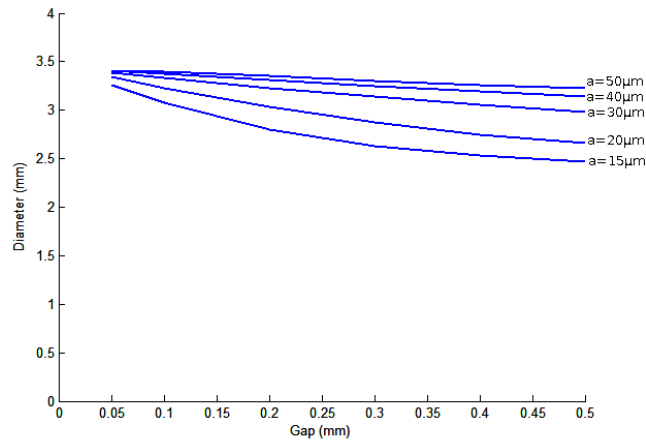
Figure 3.11 Cavitation ring diameter provided by the model for the fitted k and i.

The power of the system has been calculated from the fitted analytical model by means of Equation 3.15. This power is plotted in Figure 3.12. As well, the electric power of the ultrasonic horn measured directly in the wave generator is plotted in Figure 3.12 in dashed lines and has been fitted using a second grade polynomial regression.
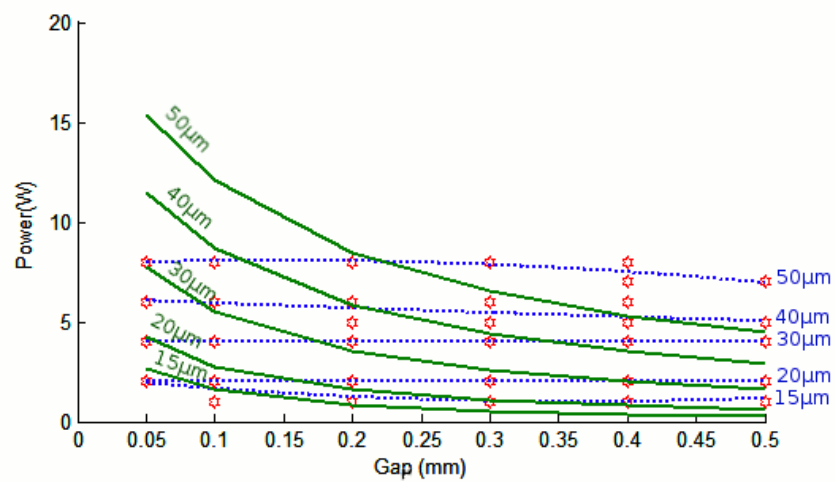
Figure 3.12 Analytically calculated power of the fluid system in solid line. Experimentally measured electrical power in dashed line.

There is a satisfactory agreement between the proposed model and the experimental data as shown in Figure 3.13. The proposed model matches with a good degree of accuracy the values of the diameters, especially in the central zone of the graph. It also agrees with less accuracy in the estimation of power as shown in Figure 3.12. The power matches especially well for a gap of 0.2 mm and it remains of the same order of magnitude for the whole range of parameters. This agreement between the analytically calculated power and the experimentally measured is highly satisfactory in comparison with the power calculated if no cavitation is assumed. If there is no cavitation the power is six magnitude orders greater than the power of the experiments. Hence, the estimated power of the proposed model is representative of the power of the system.
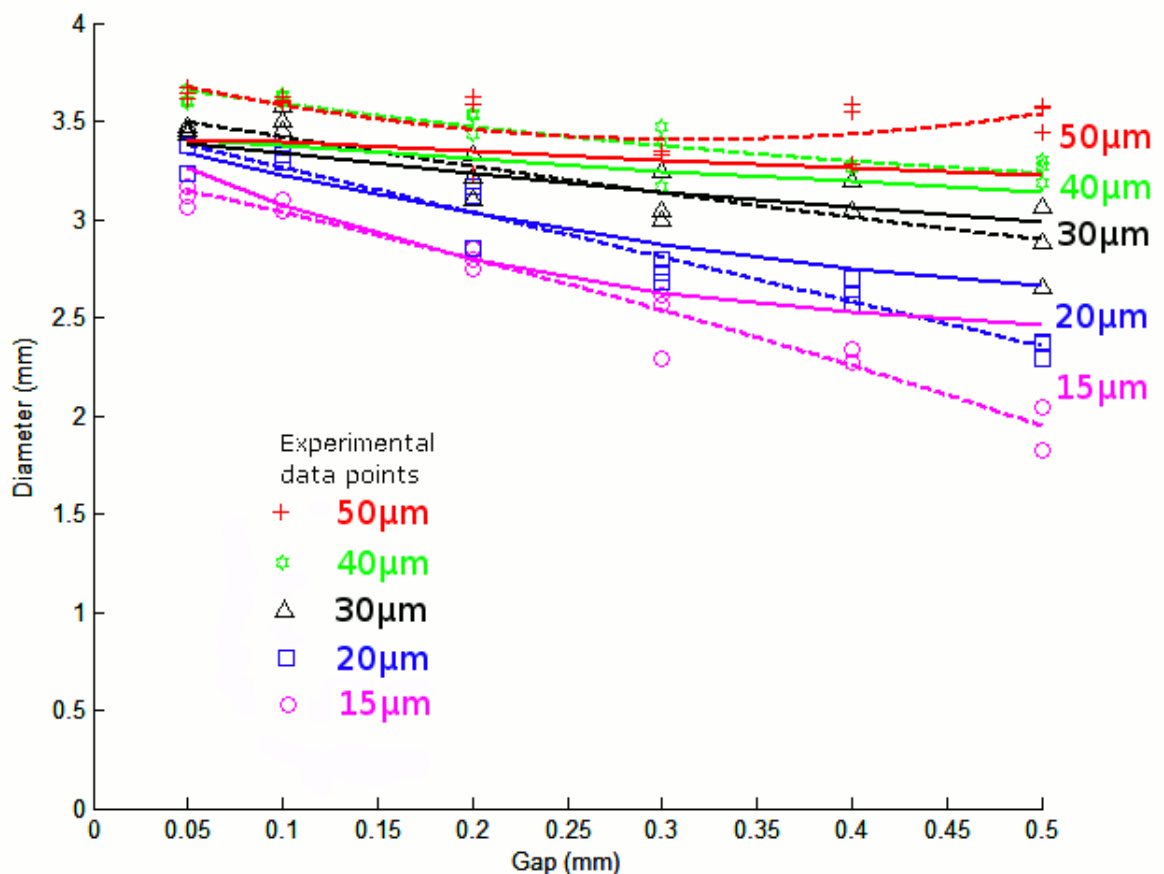
Figure 3.13 Comparison of the model (solid line) with the experimental data (dashed line).

 The introduction in the model of the intensity of turbulence, i, and the parameter k that takes into account the influence of the liquid in the surroundings allows the fitting of the diameter values of Figure 3.13. Therefore, the value of the parameter i suggests that turbulence inside of the thin layer of liquid between the horn and the sample is not negligible, while the value of the parameter k suggests that the movement of the liquid outside of the thin layer has an important influence on the cavitation clusters inside of the thin layer.

Since power and diameter calculation agree with experimental data it is possible to affirm that the model represents the system with a high degree of satisfaction. Therefore it is possible to say that the main movement of liquid inside of the thin layer is similar to that expressed in Equation 3.4, Equation 3.9 and Equation 3.10. However the high turbulence that the model suggests there is in the region "1" might vary the velocity of the fluid, although an average value of velocity inside this region is expected to be similar to the value of Equation 3.4.

The cavitation ring region allows the movement of fluid under minimum energy constraint. If the cavitation ring region is not considered, the required power is several orders of magnitude greater than considering it. Consequently, this result justifies the existence of the cavitation ring region and its size. On the other hand, the model presented here is only validated for the 5 mm diameter horn. It is not known if the existence of the cavitation ring region occurs with other diameters. It is clear that with the standard diameter of 15.9 mm does not occur. It is likely that the model works with similar diameter different to 5 mm but it is out of the scope of this research to determine where the limits for the diameters are. Nevertheless, it is anticipated that the minimum energy constraint may explain the existence of repetitive pattern in the acoustic cavitation clusters with other geometries although the model to apply Hamilton's principle might differ.

On the other hand, this distribution of the clusters in a central region and the ring region creates a non-homogeneous erosion whose implications in tribology tests are explained below.

3.1.10 Implications of the location of cavity clusters in tribology tests.

The chosen methodology in this research uses a 5 mm diameter horn instead of a 15.9 mm diameter horn that is the size given by the standard (ASTM G32). This produces a different pattern and a smaller eroded area than the standard (Figure 3.1). Consequently, the differences in erosion surface have strong implications in the way that cavitation erosion resistance is measured. Here, these implications are explained.

The standard and literature define two variables to evaluate the erosion resistance of the materials. These variables are the incubation time and the volume loss rate. To measure this variables a precision microbalance is used and the samples are measured periodically. Also, sometimes it is possible to find in the literature weight loss rate instead of volume loss rate, but the inconvenience of this is that different materials have different densities. Then, the weight loss rate has not a direct relation to the size of the erosion. The incubation time is defined in two different ways in the literature: (1) it is defined as the time that the weight loss is 0.1mg; or (2) the time where the linear regression of the weight loss intersects the axis (Figure 3.14).
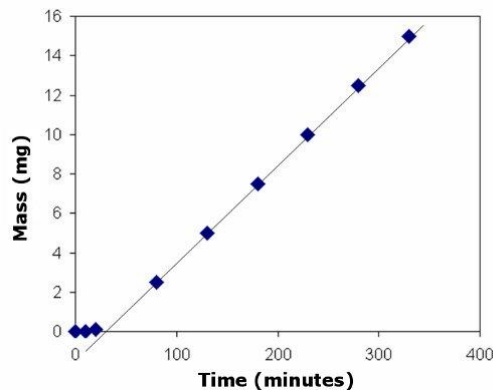
Figure 3.14 Typical weight loss versus time graph in
cavitation erosion of ceramics.

The variables defined by the standard to evaluate the erosion resistance depend on the amount of weight loss and its linearity with the time. In the set up used here, the weight loss is much smaller than in the standard and the linearity with the time is not clear. The surface eroded with the 5 mm diameter horn is around 4.5 mm^2 which is much smaller than the surface eroded with the 15.9 mm diameter horn that is 198

mm^2. It becomes difficult to measure the weight loss since the eroded material is much smaller. A comparison of the eroded areas is shown in Figure 3.15.

Figure 3.15 Comparison of eroded areas
with 15.9 mm and 5 mm diameter horns.

Apart from the fact that the eroded surface is small, there are other issues that may be present if the volume loss rate is used. Here, a explanation of this issues is presented. First, as shown in Figure 3.16, the eroded area change with the time since it presents new and larger surface when it is not flat, in the example it changes from 4.5 mm^2 to 6.6 mm^2. Besides, the width of the central and ring region may increase with the time. Furthermore, the erosion of the surface changes its geometry, loosing it flatness. As shown in Figure 3.17, the loss of flatness may change the velocity in the interface, producing turbulence and changing the boundary layer thickness and the bubble collapse occurrence. Also, the bubbles may become away from the eroded surface.
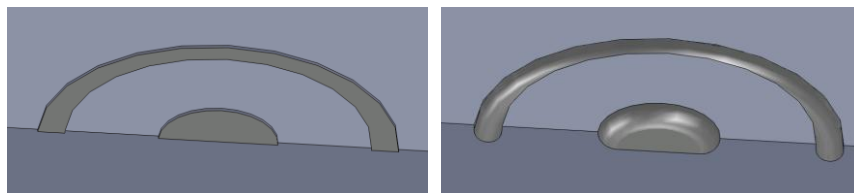
Figure 3.16 Change of erosion area.
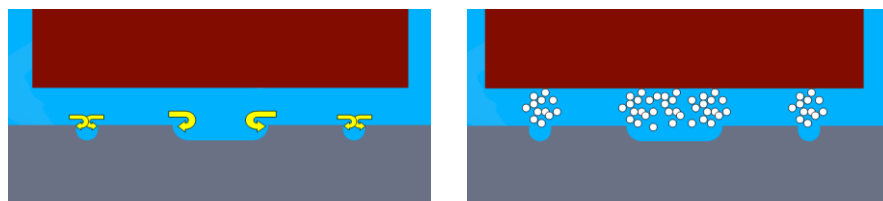
Figure 3.17 Possible effects of the erosion pattern in cavitation phenomena.

Although there are pitfalls of using cavitation erosion test with a 5 mm diameter, there are also some advantages. These advantages are:

- It produces a slower damage rate than the standard. This allows more control about the exposition to cavitation. For example: see section 4.1.5 and section 4.1.6.

- It produces different intensity of damage in different regions that helps to compare different stages of damage. This is used, for example, in section 4.1.6.

- All this characteristics are useful in research where it is important to approach the problems with different methods. This is demonstrated on ceramics where pseudoplastic deformation pits are found, see section 4.1.

- It is possible to measure surface loss as an alternative to volume loss rate. Interesting for applications where the surface state is important. In this research this is made with the central region, see Figure 4.18.

For these reasons, the experimental configuration with a small diameter probe is used thoroughly in this research instead of the standard configuration.

Chapter 4   Experimental results

In this chapter, the experimental results are presented. This chapter is divided in three sections that are the cavitation erosion resistance of ceramics, the phase delay in zirconia and the mechanical behaviour of the ceramic surface subjected to various conditions.

4.1   Early stages of cavitation erosion within ceramics

4.1.1   Cavitation erosion on Silicon Nitride

Figure 4.1 shows the damage produced in the silicon nitride "A" in the first 15 seconds of cavitation exposure. It consists on few small pits shown by a black arrow. The pits that are not labelled with a small black arrow were present before tests and can be the results of the sample polishing.

Figure 4.1 Pseudoplastic deformation pits in silicon nitride "A" that have been produced in 15 seconds of cavitation exposure. (Optical microscope).

Figure 4.2 shows the measurement with an interferometer profiler of a plastic deformation pit produced in the first minute. The largest pits can have dimensions of up to 0.05-0.09 μm depth and diameters of 8-12 μm depending on the silicon nitride material and the pit. Typical diameters of the jet stream in a collapsing bubble are about 4 μm for bubbles of 200 μm diameter (Haosheng et al. 2008).This value is consistent with the size of the damage.
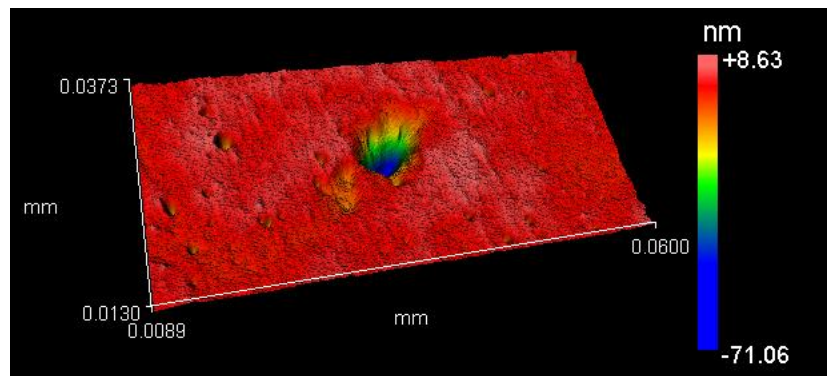
Figure 4.2 Pseudoplastic deformation pit in silicon nitride "A" that has been produced in one minute of cavitation exposure. (Interferometer measurement).

Figure 4.3 and Figure 4.4 show three typical pits of the early erosion damage seen with polarizing filter with two magnifications. They are indicated with circles. The contrast produced by the slope of the plastic deformation is very obvious at low magnification with polarizing filter but it is not so evident at high magnification, this is an optical effect. It is possible to observe at high magnification that no material loss, in terms of grain pull-out, break-outs or complete dislodging has occurred yet. These pits could be local shallow surface pseudoplastic deformation creating a slight surface depression visible under the optical microscope with polarizing filter. These surface local depressions or pseudo plasticity pits are a result of pseudo plasticity deformation under the pressure of a large bubble collapsing. Observation at high magnification showed that there could be some microcrack on the surface corresponding to the edges of the depressed region from cavitation compression pressures or from shock waves.
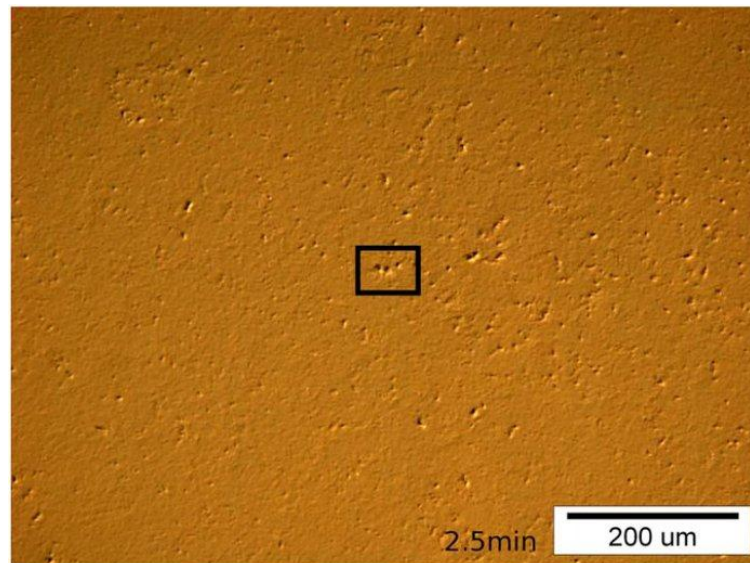
Figure 4.3 Pseudoplastic deformation pits in silicon nitride "B" that have
been produced in 2.5 minutes of cavitation exposure. (Optical microscope).
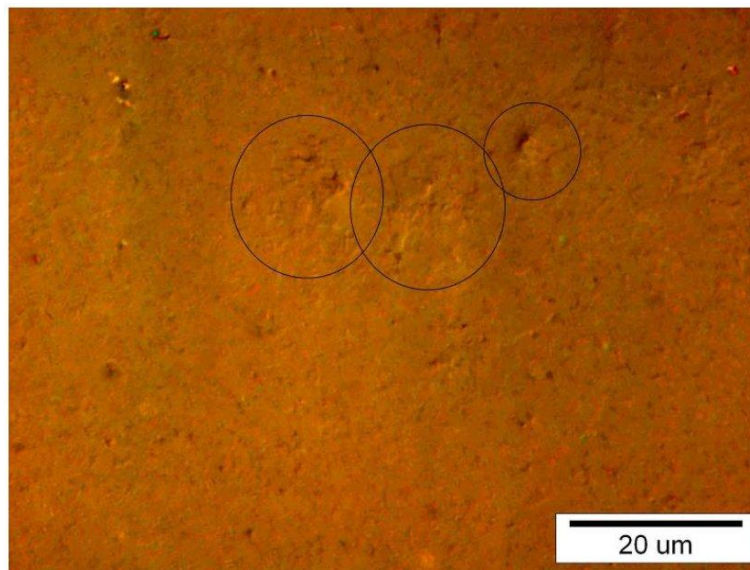
Figure 4.4 High magnification of the indicated zone of Figure 4.3.
(Optical microscope).

Figure 4.5 shows the surface of silicon nitride "A" eroded after 180 minutes of
cavitation erosion as opposed to Figure 4.4 after 2.5 minutes. The surface
experiences material loss, with small surface break-outs clustered, where several
grains are pulled out, dislodged from the surface. The rest of the surface shows
evidence of smaller isolated grain pull-outs or grain in the process of being dislodged
from the surface and possible intergranular cracking.
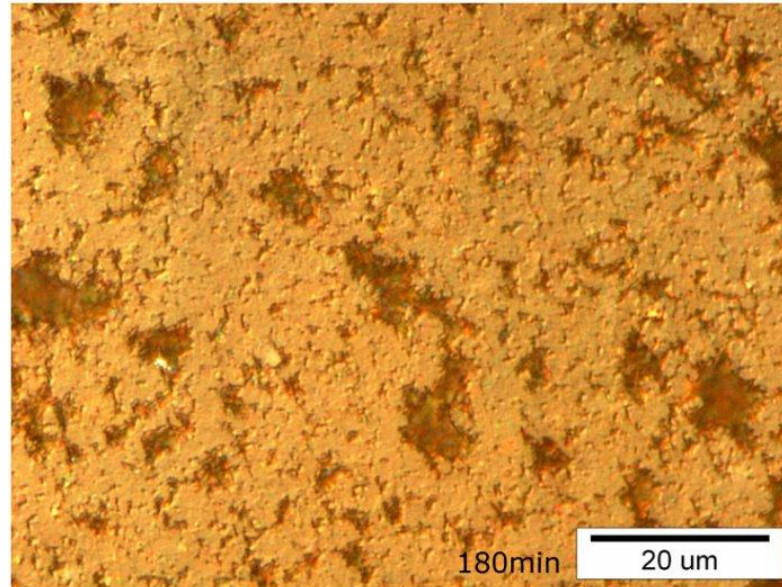
Figure 4.5 Surface damage on silicon nitride "A" after 180min. (Optical microscope).

All surface features are produced by cavitation, as the original surface was devoid of any of these features. SEM observation of these features is also performed and it is shown in Figure 4.6. The damage is mostly intergranular cracking, partial and complete dislodging and pull-outs of single grains or cluster of grains (Figure 4.7). When damage is initiated, new roughness due to missing surface grain enhances the severity of erosion and further wear around the first damage nuclei.
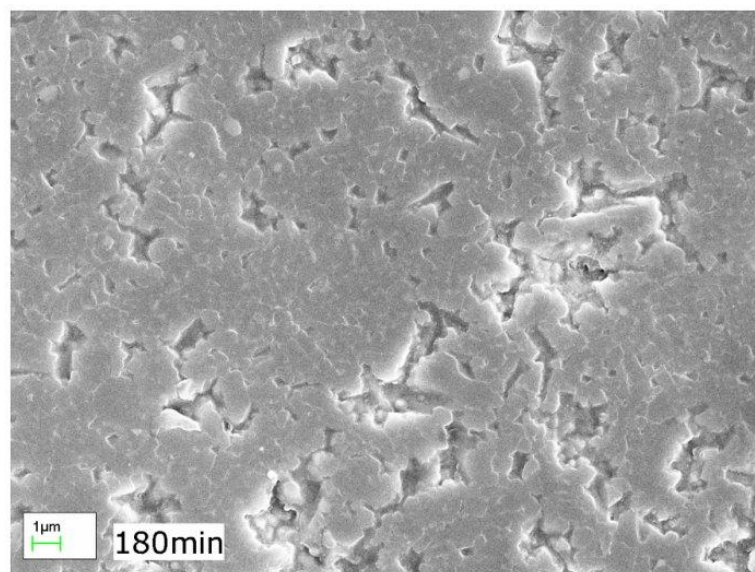
Figure 4.6 Surface damage on a silicon nitride "A" after 180min.(SEM).
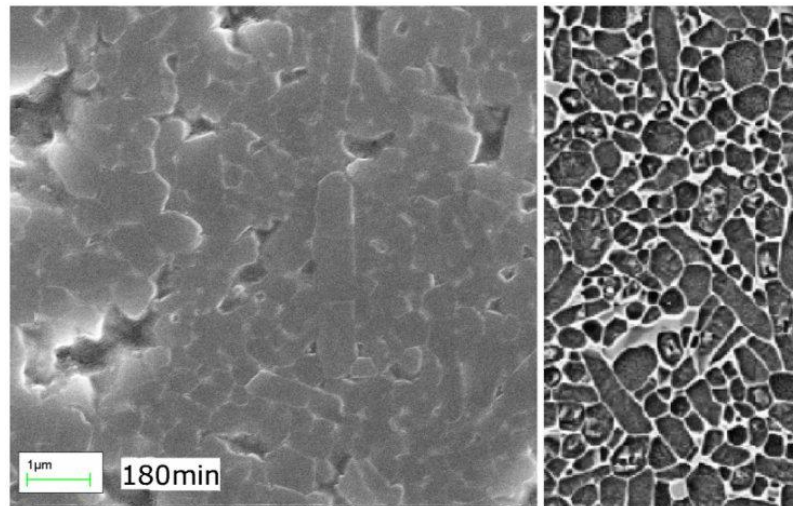
Figure 4.7 Surface damage on a silicon nitride "A" after 180 min.
Comparison with microstructure Figure 2.5 from SKF. (SEM).

4.1.2 *Cavitation erosion on Zirconia.*

Zirconia "H" presents the best cavitation erosion resistance behaviour among the ceramic materials studied here. Four small pseudoplastic deformation pits are seen in the first 30 seconds of cavitation erosion test, and this number increases proportionally with the time. These pseudoplastic deformation pits are similar to those shown on the surface of silicon nitride but they tend to be smaller than those of silicon nitride and their formation is more unlikely than in silicon nitride. The largest pits can have dimensions of up to 0.03-0.05 μm depth and diameters of 3-6 μm. The same impact pressure from a collapsing bubble is more likely to produce a pseudoplastic deformation pit in silicon nitride than in zirconia since the pressure threshold to produce the pit is smaller in silicon nitride than in zirconia.

Figure 4.8 shows the erosion damage after 180 min of test with visible material loss.
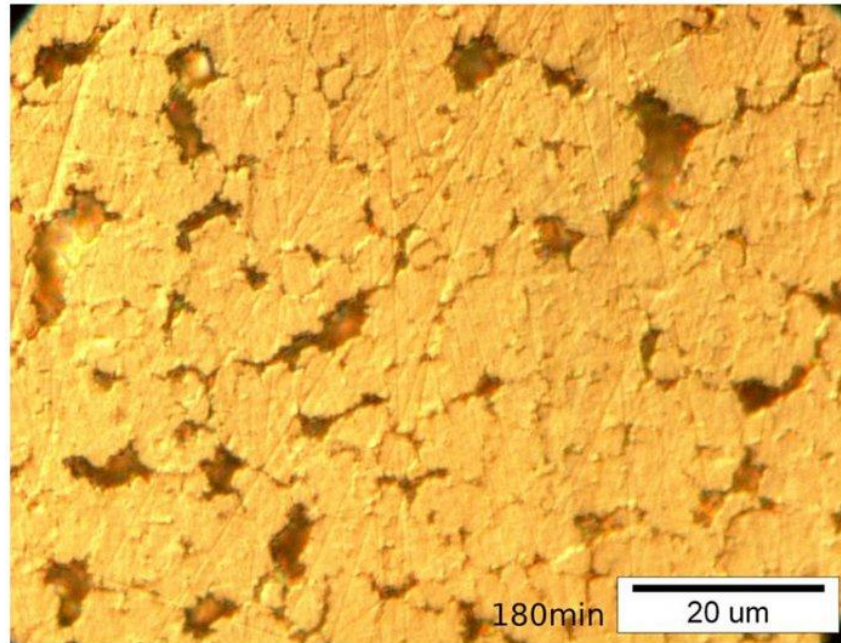
Figure 4.8 Zirconia "H". Surface damage. (Optical microscope).

The process of material loss consists of the following: the pressure and the pseudoplastic deformations create cracks that with the time dislodge grains from the surface and can lead to larger local break-outs, Figure 4.9 and Figure 4.10.
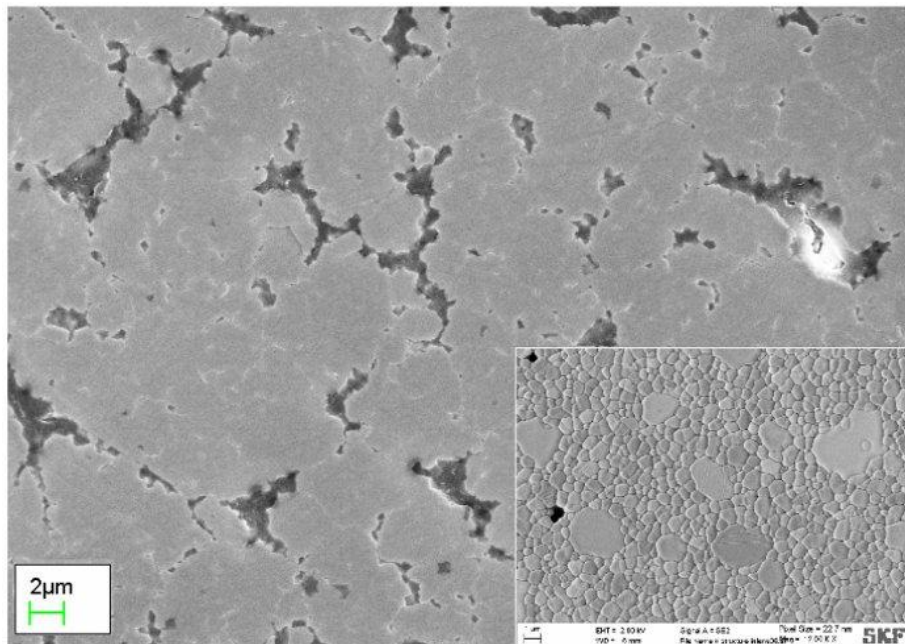
Figure 4.9. Zirconia "H". Surface damage after 180 minutes.
Comparison with microstructure Figure 2.12 from SKF. (SEM).
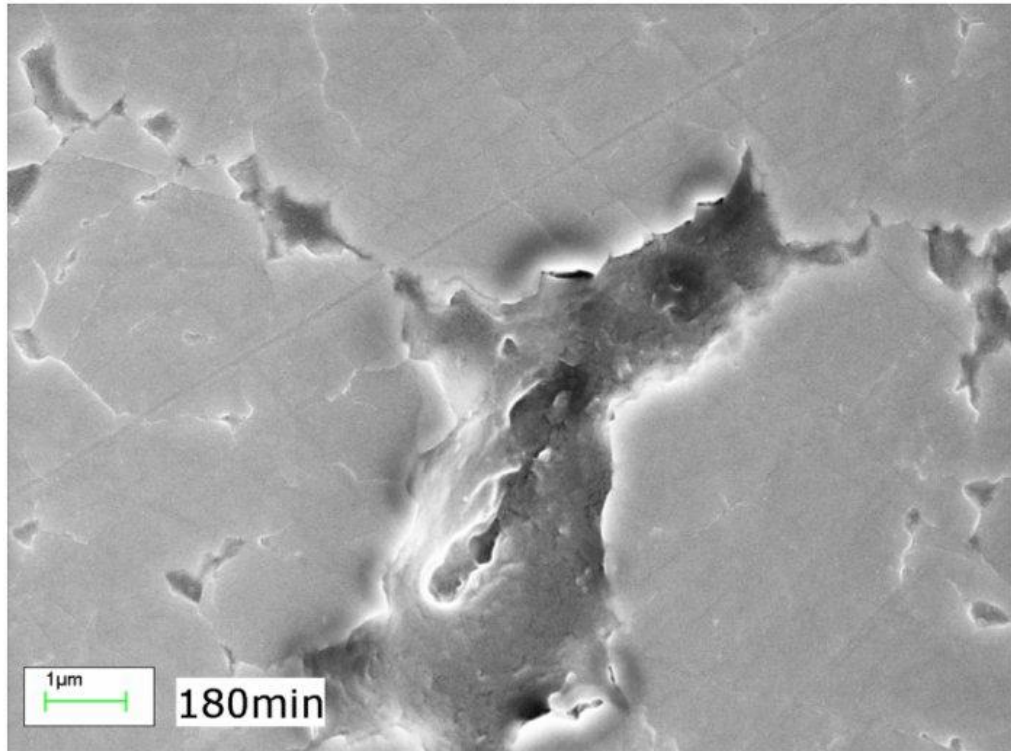
Figure 4.10. Zirconia "H". Surface damage, detail. (SEM).

The zirconia is based on the tetragonal phase, metastable phase, stabilised at room temperature by the yttria dopant. As explained in section 1.2.6, it is known that the tetragonal phase can change and transform back into the stable monoclinic phase at low temperature when subjected to enough pressure and in presence of water. Upon phase transformation, the grain undergoes a small volume increase. The relationship of this with the cavitation resistance has been studied (Lu et al. 2008). It has been found that in fact there is a change of phase and transformation toughening in zirconia when it is exposed to cavitation.

The present study found out that the surface can change just with the time after the end of the erosion test, when the sample is stored at room temperature in air. Figure 4.11 shows the surface after 40 minutes of cavitation exposure. Figure 4.12 shows exactly the same surface that Figure 4.11 two months later. The surface has changed. It is possible to look at the same points in both micrographs using the polishing lines as references. The surface develops a topography with small local protruding areas. This suggests that the metastable tetragonal phase can transform spontaneously into the monoclinic in time when stored at rest in air at room temperature after being

"activated" with cavitation. This transformation occurres at room temperature. This is studied deeper in section 4.2 for other zirconia materials with different composition.
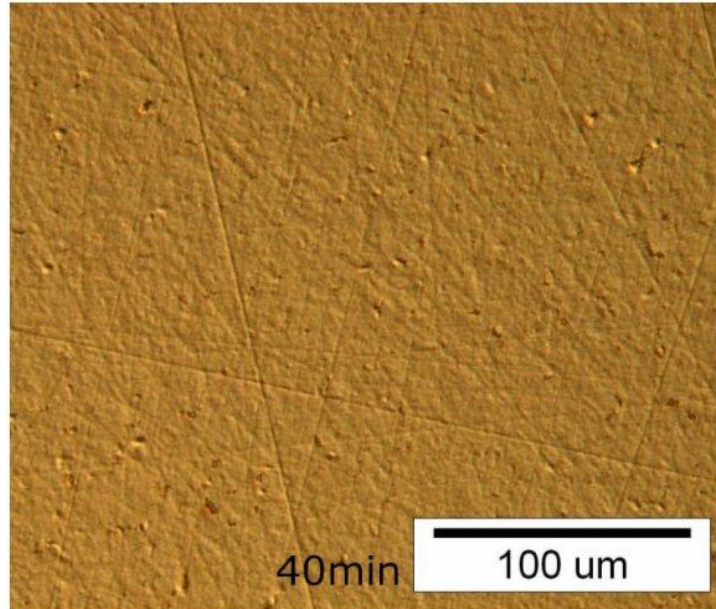
Figure 4.11 Zirconia "H". Surface state after the experiment. (Optical microscope).
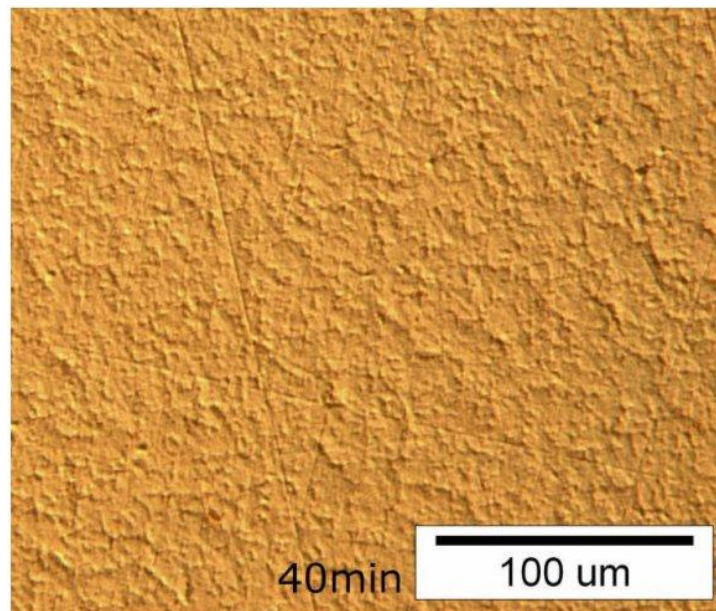
Figure 4.12 Surface of Figure 4.11. Surface state 2 months after the experiment. (Optical microscope).

4.1.3 *Cavitation erosion on Alumina.*

Alumina cavitation erosion shows in the first 30 seconds a few number of points with
change of slope. This is not clear if it is due to pseudoplastic deformation pits or
direct brittle fracture dislodging grains at the surface. These features are very small
in comparison with the ones visible in other materials. Very quickly with testing
time, intergranular micro-cracks appear and grow, especially close to defects from
the finishing. These cracks lead to grain pull-outs and larger break-outs in the first
minutes of tests. Figure 4.13 and Figure 4.14 show the micro-cracks and the grain
pull-outs and larger break-outs after 6 and 10 minutes of tests in the same region.
The mechanism of erosion of the alumina "N" is different to the others materials.
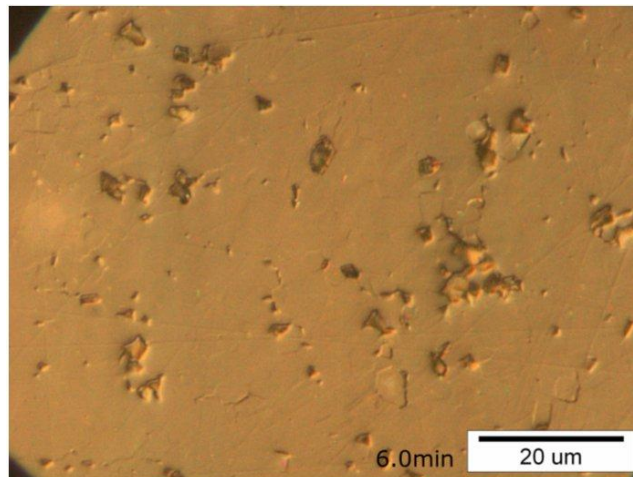
Figure 4.13. Alumina "N". Cracks and grain pull-outs (6 minutes). (Optical microscope).
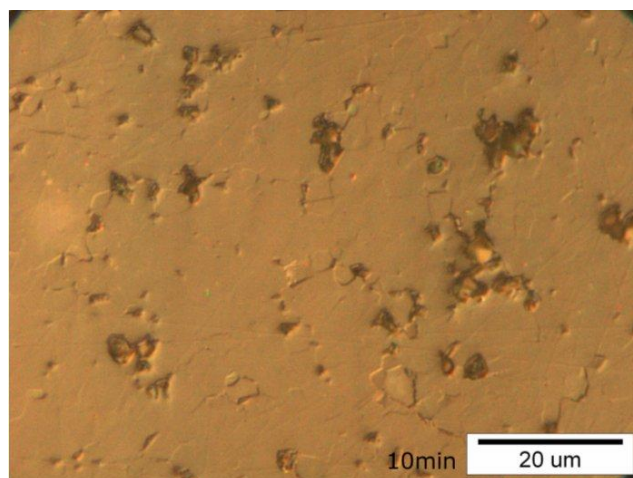
Figure 4.14. Alumina "N". Cracks and grain pull-outs (10 minutes). (Optical microscope).

4.1.4 *Cavitation erosion on Steel.*

Stainless steel is studied here as a reference material for comparison purposes. The stainless steel sample is a nitrogen martensitic stainless steel with a Vickers hardness of 734 kg/mm2.

The stainless steel behaviour under cavitation erosion test is completely different to the ceramic materials due to its capability of plastic deformation and work-hardening. The plastic deformation of its surface is pronounced and accumulated with testing time. It starts within the first few seconds and extends during experimental time. To see the plastic deformation pits isolated one from each other is necessary to stop the ultrasonic transducer in the first seconds. This study has done it after two seconds, in order to measure the volume of the pits respect the original surface.

The number of plastic deformation pits over a determined area increases quickly in the first minute. These pits are clearly larger than those from other materials. The largest pits can have dimensions of up to 0.08-0.15 µm depth and diameters of 11-15 µm. After the first minute the number of pits increases but these pits are smaller with the time. Figure 4.15 shows the damage progress. This effect is originated because of the work-hardened of the surface produced by accumulated plastic deformation.
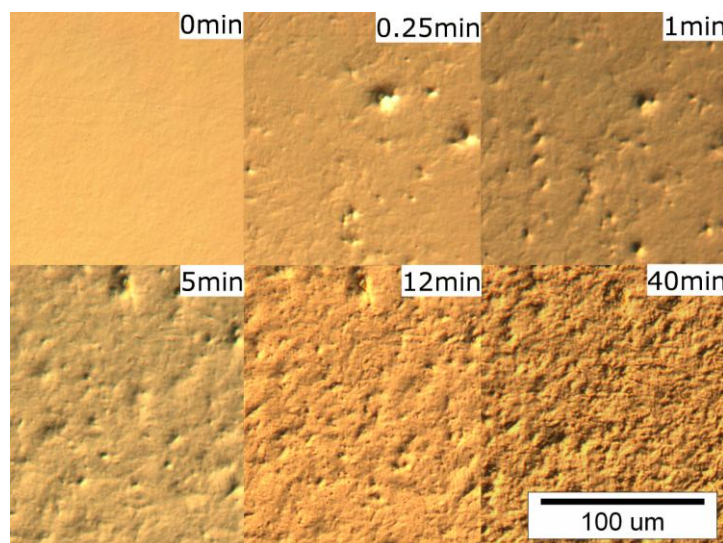
Figure 4.15. Stainless steel. Plastic deformation. (Optical microscope).

The typical form of the plastic deformation pit is shown in Figure 4.16. This shows that there is no accumulation of material on the sides of the pit, thus, the pit is so shallow that the material, probably, is just compressed towards inside of the surface, orthogonal to this without creating apparently raised edges from elastic relaxation, but this could be hidden because of the different magnification scale of the image in vertical and horizontal axis, because of the very small depth of the pit, 88 nm and because of the elastic properties of the material surrounding that can absorb the small deformation.
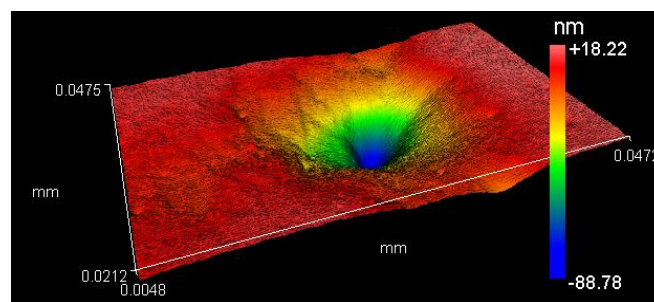
Figure 4.16. Plastic deformation pit in Stainless Steel that has been produced in two seconds of cavitation exposure. (Interferometer measurement).

A different colour appears in the region of more severe cavitation erosion during the second hour of cavitation exposure in the micrographs. Although it may be possible to think that this colour is due to oxidation because of the temperatures that cavitation can achieve, the analysis of elements in the scanning electron microscope does not show evidence of oxygen in the region. Figure 4.17 shows this coloured effect. On the other hand, identification of material loss start using microscopy is not possible due to the high undulation of the surface due to deformation.
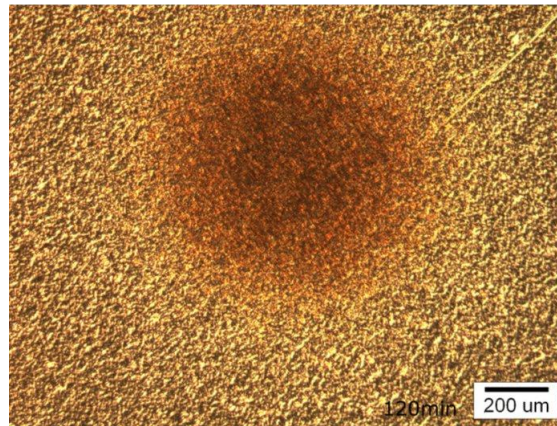
Figure 4.17. Cavitation erosion region on steel after 120
minutes of cavitation exposure. (Optical microscope).

4.1.5 *Rankings of cavitation erosion resistance and performance.*

In order to create a ranking of the materials and to obtain a better understanding of
the mechanisms of cavitation erosion of these materials, several criterions are
followed. Table 4.1 shows the volume and the depth of a typical pseudoplastic
deformation pit visible with polarizing filter and low magnification in optical
microscope. It is measured with interferometer profiler at maximum magnification
and the result showed is an average of at least three different pits for each material.
An example of these pits is Figure 4.2.

Table 4.1 Measurement averages of pseudoplastic deformation pits with profiler
interferometer.

	Time of measurement	Typical Volume (μm^3)	Typical Depth (μm)
Alumina "N"	-	Not measurable	Not measurable
Zirconia "H"	4 min	0.6	0.03
Silicon nitride "A"	1 min	1.7	0.05
Silicon nitride "C"	0.5 min	2.0	0.06
Silicon nitride "D"	1 min	2.2	0.08
Silicon nitride "B"	2 min	3.3	0.09
Stainless steel	2 sec	10.0	0.13

Table 4.2 shows the surface roughness after 120 minutes of cavitation exposure. The
table is ordered from smaller to greater roughness.

Table 4.2 Surface roughness after 120 minutes to cavitation exposure.

	R_a	*rms*
Silicon nitride "A"	0.007 µm	0.020 µm
Zirconia "H" (after 11 days)	0.014 µm	0.048 µm
Zirconia "H" (after 3 months)	0.019 µm	0.065 µm
Zirconia "H" (after 1 day)	0.032 µm	0.158 µm
Stainless steel	0.153 µm	0.206 µm
Silicon nitride "C"	0.527 µm	0.670 µm
Silicon nitride "B"	0.654 µm	0.913 µm
Silicon nitride "D"	1.083 µm	1.324 µm
Alumina "N"	1.138 µm	1.437 µm

Table 4.3 shows the number of plastic deformation pits that are possible to count using optical microscope after 30 seconds of cavitation exposure. In the case of alumina is not clear if this is pseudoplasticity pits or slope change due to immediate fracture/partial grain dislodging. This measurement are made summing the pits produced in the first 15 seconds plus the pits produced from 15 to 30 seconds. The number of pits is similar in both times.

Table 4.3 Number of plastic deformation pits produced in the surface after 30 seconds of cavitation exposure.

Material	0-15 s	15-30 s	Total
Zirconia "H"	3	1	4
Alumina "N"	4	9	13
Silicon nitride "A"	31	31	62
Silicon nitride "D"	25	37	62
Silicon nitride "B"	42	35	77
Silicon nitride "C"	44	45	89
Stainless steel	massive	massive	massive

Table 4.4 shows the surface that is removed due to cavitation erosion after 120 minutes of exposure. To calculate this, the micrographs are processed with image software. By means of changing the contrast and the brightness, the images of Figure 4.18 are obtained where the black dots correspond to a region where the original surface is lost and the reflection of light in the optical microscope is weak. As the size of the pixel is known, the area of surface loss is calculated. The processed

micrographs are shown in Figure 4.18. Table 4.5 shows the comparison of silicon nitride "A" and zirconia "H" in a later state, after 180 minutes of exposure. In this stage zirconia "H" has a better result.

Table 4.4 Surface loss after 120 minutes to cavitation exposure.

Material	Surface loss (Area)
Silicon Nitride "A"	$0.006\ mm^2$
Zirconia "H"	$0.015\ mm^2$
Silicon Nitride "B"	$0.308\ mm^2$
Silicon Nitride "D"	$0.450\ mm^2$
Silicon Nitride "C"	$0.548\ mm^2$
Alumina "N"	$>1.067\ mm^2$
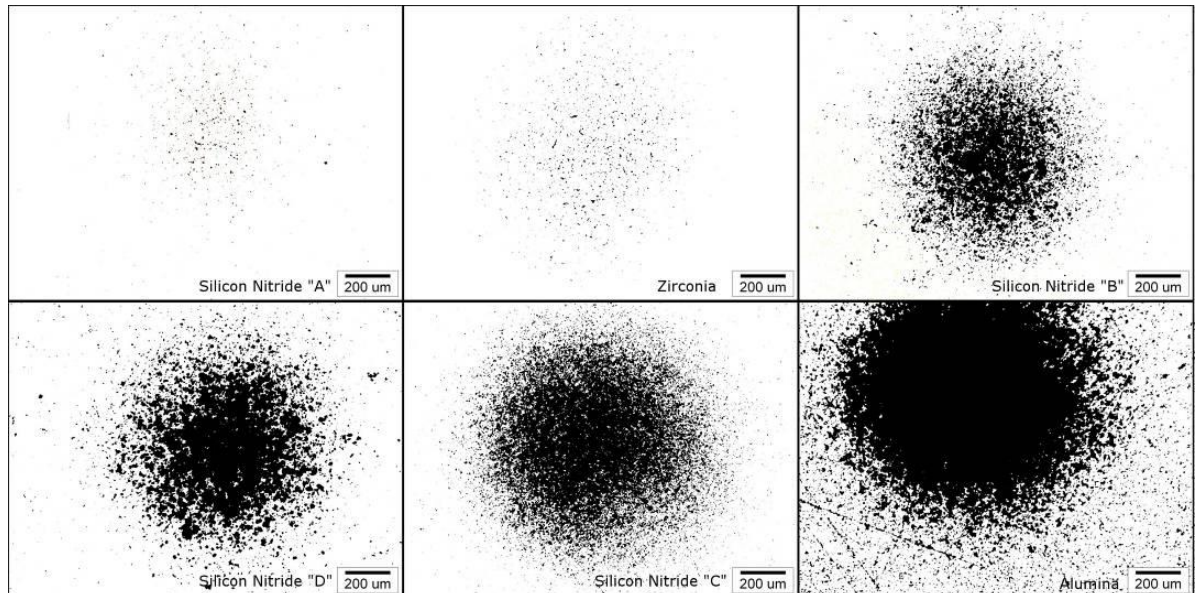
Figure 4.18 Surface loss after 120 minutes to cavitation exposure. Processed micrographs.

Table 4.5 Surface loss after 180 minutes to cavitation exposure.

Material	Surface loss (Area)
Zirconia "H"	0.091 mm2
Silicon nitride "A"	0.144 mm2

4.1.6   *Hardness of ceramics subjected to cavitation erosion.*

As explained before, section 4.1.1, silicon nitride and zirconia suffers permanent deformation when subjected to cavitation erosion. According to the theory, when a grain of ceramic is plastically deformed, there is dislocation movement and multiplication. This effect produces on the grain a work hardening effect that increases the hardness of the grain. This is due to the dislocations interaction. When dislocations intersect, jogs are formed and they pin the dislocations (Green 1998). The work hardening for a single crystal has been extensively studied. A review of different models made in order to calculate the work hardening due to dislocations in the different slip systems can be found (Khan and Huang 1995). In general, these models present in a matrix or summation way the contribution to the deformation in every slip system for the work hardening in a specific slip system.

 According to the theory of work hardening due to dislocations, it can be expected to have greater material hardness in the area damaged by erosion than in the original surface. As stated in section 4.1.4, steel has this behaviour remarkably, there is a work hardening produced by the plastic deformation of the surface. Then, the existence of this behaviour in ceramics is studied here.

The hardness of the surface in the whole cavitation erosion pattern is measured. The material chosen for this experiment is silicon nitride "A", the properties of the material are in section 2.4. It is subjected to cavitation erosion for 3 hours creating on the surface the typical damage characterised by a central region and a ring region as explained in section 3.1.1 and 3.1.10. These two regions allow measuring the hardness within surface with different damage grade. The central region has the most severe damage, the ring region has also severe damage and the zone between central region and ring region has light damage. Besides, there is a transition from light damage to no damage in the external part of the ring region.
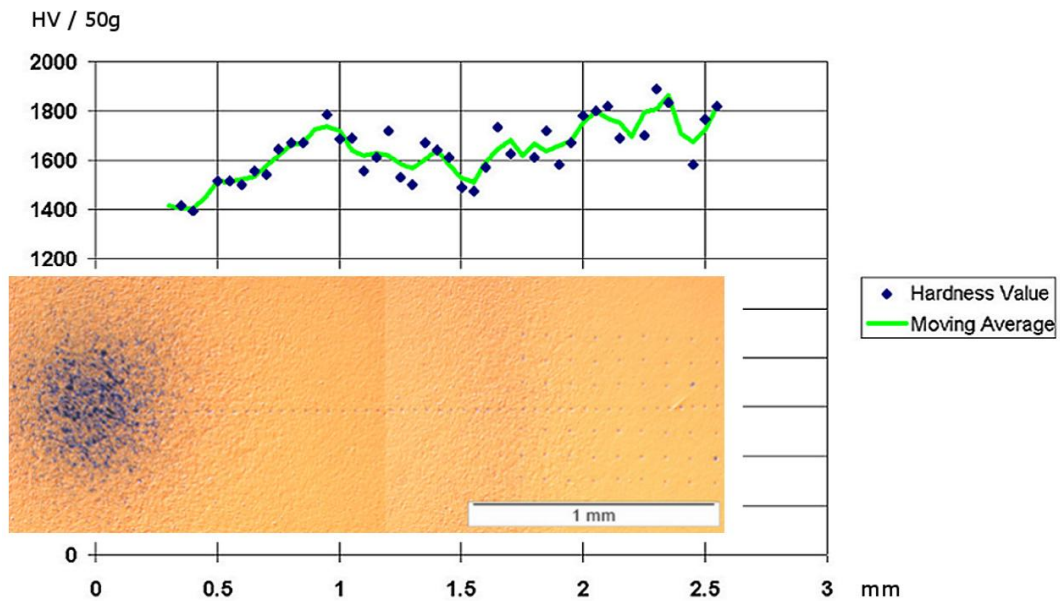
Figure 4.19 Vickers Hardness (50g) along the cavitation erosion pattern of Silicon Nitride after 3 hours of cavitation erosion. Composition of two images.

Figure 4.19 shows the distribution of microhardness in the different regions of cavitation damage. It is clear that the region outside the damage has the highest hardness, conversely the regions that have clear damage present the lowest hardness. The hardness is minimal in the central region, where the cavitation damage is severe. In the zone between the central region and the ring region, the hardness is higher than in the other regions but it is still a bit lower than outside of the damaged surface.

In order to study the apparent softening effect on the surface statistically, the hardness of silicon nitride "D" is measured before and after 4 minutes of cavitation exposure. The measurement of hardness is made in the same region with 65 indentations before cavitation and 64 indentations after cavitation. The indentations are separated by 70 µm and the diagonal of the indentation is approximately 5 µm. Some of the indentations made after cavitation are close to previous indentations and are not taken into account because of this. The load for the Vickers hardness is 25 grams. This load is chosen as a balance between a lower load (15 grams) whose indentation could be difficult to be measured in the optical microscope and a larger

load (50 grams) whose indentation could be too deep and the softening effect due to small surface cracks could be reduced.
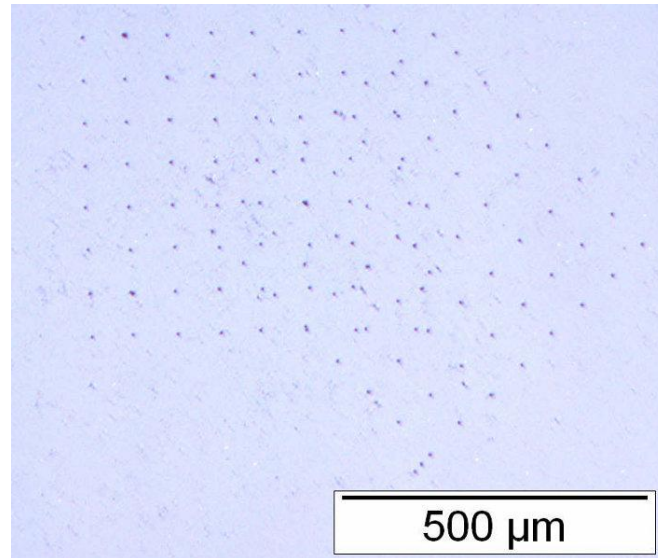
Figure 4.20 Vickers Hardness (25g) indentations on silicon nitride "D". The two groups of indentations, before and after 4 minutes of cavitation. Micrograph without polarizing filter.

From the statistical point of view, the two groups of indentation measures are studied as samples of two populations. The populations are all the values that can be obtained through Vickers hardness indentation on the surface of silicon nitride "D", before and after cavitation. The size of the samples is equal of bigger than 60. The Kolmogorov-Smirnov test is used to compare the samples with a standard distribution. The result of the test is that the samples follow a standard distribution as it was expected. To characterise a standard distribution is necessary a sample size bigger than 30. In this case, the sample sizes are 60 and 65 that are far enough to characterise the standard distribution. The values of hardness and its probability density function are plotted in Figure 4.20. The Vickers hardness for silicon nitride "D" before cavitation is 1493 kg/mm^2 and its standard deviation is 139 kg/mm^2, the hardness after 4 minutes of cavitation exposure is 1398 kg/mm^2 and its standard deviation is 166 kg/mm^2.
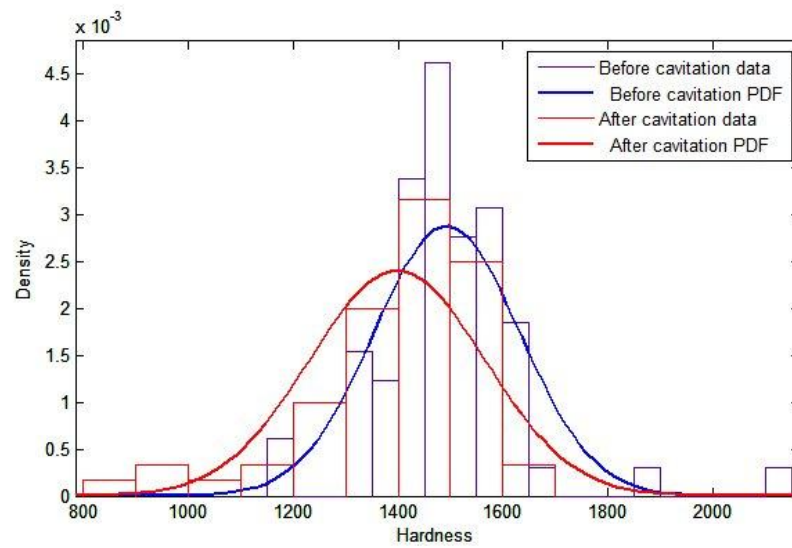
Figure 4.21 Probability density function (PDF) of Vickers hardness (25g) of silicon nitride "D" before and after 4 minutes of cavitation exposure.

As it is possible to see in Figure 4.21, although the standard deviation of the indentation values is larger after cavitation than before, the probability of obtaining a value of 1600 kg/mm^2 after cavitation is smaller than before. The same situation happens for any value bigger than 1493 kg/mm^2. This means that there is no work hardening effect on the surface although very slight damage is produced on the surface with 4 minutes of cavitation exposure.

The same experiment is performed with silicon nitride "A". Silicon nitride "A" has the best cavitation erosion resistance performance among the silicon nitrides tested in section 4.1.5. However, unlike zirconia, it presents a very similar number and size of plastic deformation pits as other silicon nitrides. The number of indentations made for these distributions is between 32 and 36 indentations. The results are presented in Figure 4.22.
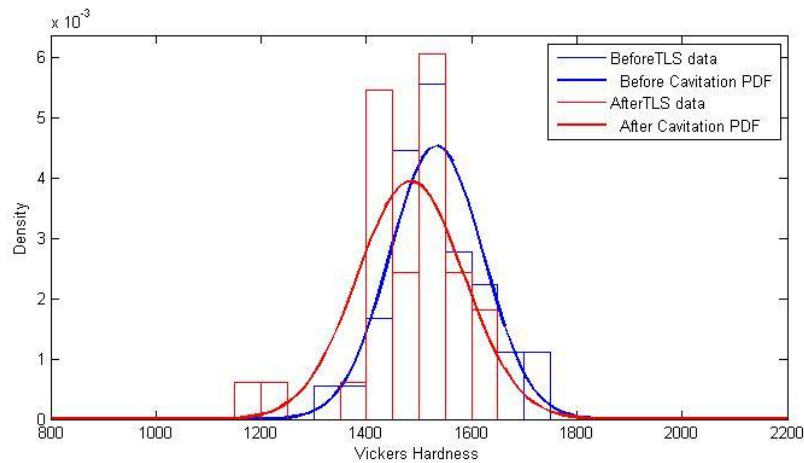
Figure 4.22 Probability density function (PDF) of Vickers hardness (25g) of silicon nitride "A" before and after 4 minutes of cavitation exposure.

In the same way as made for silicon nitride, the softening effect on the surface of zirconia "I" is measured, in this case. As the number of plastic deformation pits is small for zirconia, since the behaviour reported in section 4.1.2 is repeated in other zirconia materials, the exposure times are 4 minutes and 20 minutes. The number of indentations for the measurements is between 32 and 36. The exposure to cavitation for 4 minutes hardly changes the value of the hardness, and it increases the standard deviation. However, the exposure to cavitation for 20 minutes reduces the "apparent" hardness and increases clearly the standard deviation, Figure 4.23. In this case, after 4 minutes of cavitation exposure, the hardness of the material slightly increases. Also, the possibility of having a hardness measurement of, for example, 1330 kg/mm^2 is higher after cavitation than before. This behaviour may be produced by the transformation toughening during the exposure to cavitation. The increase of volume in the monoclinic phase may produce a compressive residual stress that gives smaller indentation footprints.
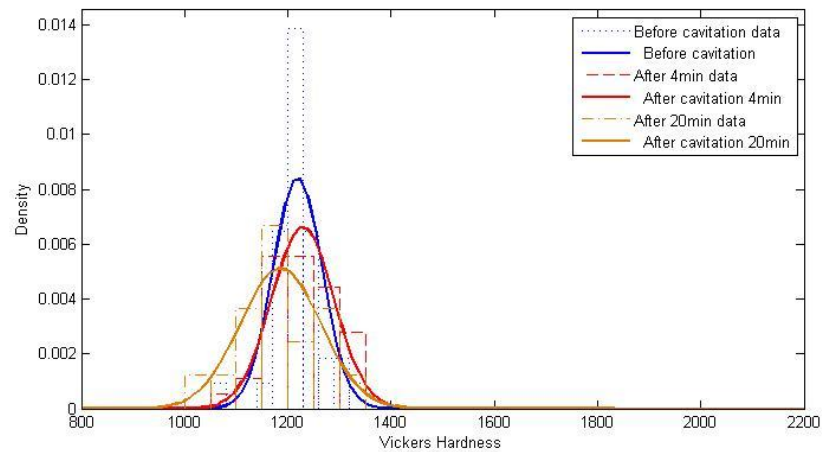
Figure 4.23 Probability density function (PDF) of Vickers hardness (25g) of
zirconia "I" before and after 4 and 20 minutes of cavitation exposure.

The hardness and the standard deviation are summarized in Table 4.6. It is interesting
the fact that silicon nitride "A", that has better performance in cavitation erosion
resistance that silicon nitride "D", has a smaller decrease of hardness than silicon
nitride "D".

Table 4.6. Vickers Hardness (25g) and standard deviation before and after cavitation
exposure.

Material	Before	After 4 minutes cav.	After 20 minutes cav.
Silicon nitride "D" kg/mm^2	1493 ($\pm$139)	1398 ($\pm$166)	-
Silicon nitride "A" kg/mm^2	1533 ($\pm$ 88)	1484 ($\pm$101)	-
Zirconia "I" kg/mm^2	1219 ($\pm$ 47)	1229 ($\pm$ 60)	1185 ($\pm$ 78)

When subjecting ceramics to cavitation exposure, although the surface presents some
deformation, there is no apparent work hardening effect. It is clear that the work
hardening effect is not achieved, but a weakening effect. The explanation is that the
cracks associated with cavitation exposure (section 5.1.1), that are created in the
grain boundaries, allow the movement of the dislocations, produce regions where the
grains can move one respect another, creates stress risers that facilitate deformation
and weaken the surface. Although it is likely, according to the theory, that the
dislocations have produced work hardening on the grain itself, the surface, as a set of
grains, grain boundaries and cracks, is weakened.

4.2 Phase transformation delay in zirconia subjected to cavitation erosion.

As seen in section 4.1.2, zirconia "H" has a phase transformation delay after being exposed to cavitation. This phenomenon is reported for first time in this investigation. The cavitation erosion "activates" the surface. In order to look into this phenomenon deeper, the roughness of the sample is monitored. A 3D interferometry profile is measured in a region exposed to cavitation for 40 minutes one day after and eleven days after, and in other region exposed to cavitation for the same time two months ago. These values are shown in Table 4.7.

Table 4.7. Zirconia "H", change of roughness with the time after 40 minutes of cavitation exposure. The surface has been "activated".

	R_a	*rms*
Region A after 1 day	0.004μm	0.006μm
Region A after 11 days	0.006μm	0.010μm
Region B after 2 months	0.008μm	0.011μm

In order to check if the transformation creates bulging of the surface due to volume increase and if it does not produce real cracking and grain dislodging several high magnification micrographs of this process are taken after 40 minutes and 120 minutes of cavitation exposure. Figure 4.24 and Figure 4.25 show that the principal characteristic of this transformation is bulging of the surface and the existing cracks become more visible than before. In this case, the changes of the surface seems to be smaller than before due to polarizing filter does not show the slopes of the surface in an evident way with high magnification.
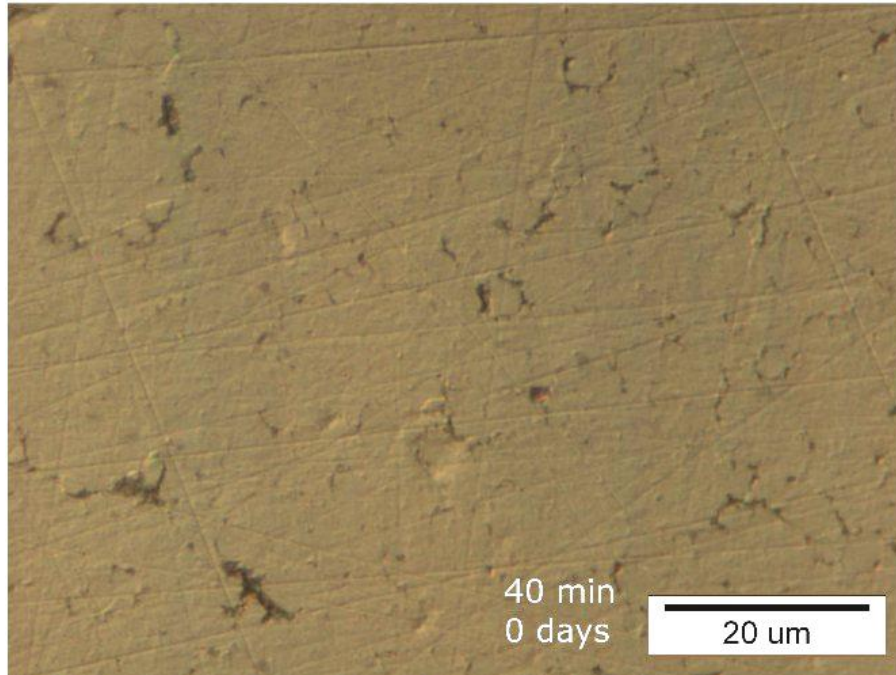
Figure 4.24. Zirconia "H". Surface state after the experiment. Optical microscope.
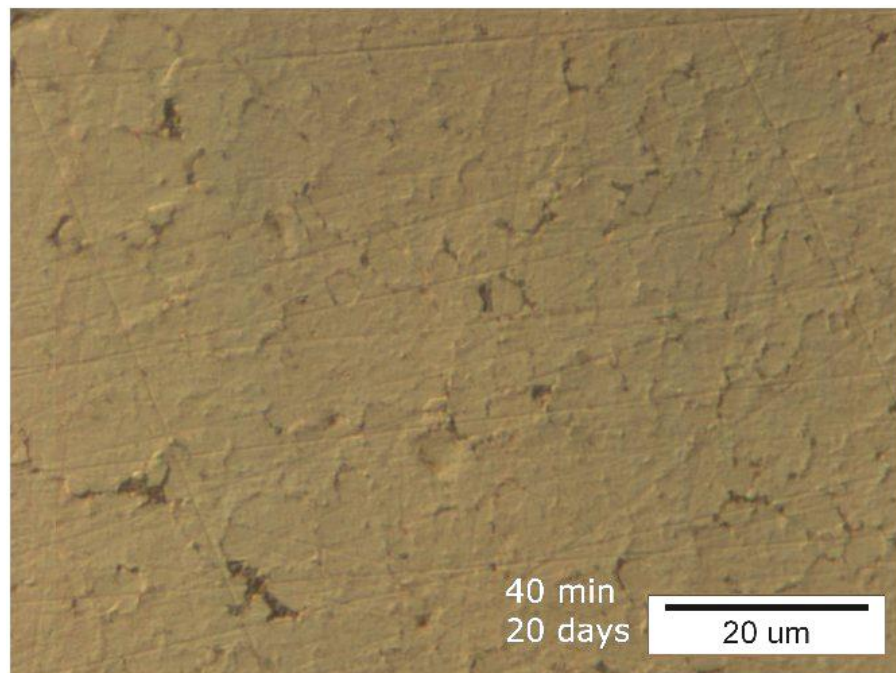
Figure 4.25. Zirconia "H". Surface state after the experiment. Optical microscope.

It is important to check if the phase transformation delay occurs with other types of partially stabilized zirconia. As such it is studied with detail for five commercial types of zirconia. The zirconia materials are "I", "J", "K", "L" and "M". The properties of the materials are given in section 2.4.

The "activation" of the surface effect is clearly shown in zirconia "I", "J" and "M". In zirconia "K" is shown, but in a smaller amount than in "I", "J" and "M". Zirconia "L" does not present the aging effect. To illustrate this, an image composition with the five different materials is presented in Figure 4.26. The samples are exposed to cavitation erosion for 40 minutes. Then, micrographs of the eroded surface are taken and the samples are rest in a cupboard, at room temperature for one month. After that time, new micrographs of the same surfaces are taken. Figure 4.26 shows the micrographs immediately after the exposure to cavitation in the first row and one month later in the second row.

Materials "I" and "J" present clear aging. Material "M" presents clear aging also but the damage due to cavitation erosion is higher. Material "K" presents aging also but in a smaller amount than the others probably due to the presence of hafnium oxide in its composition. Material "L" does not present the aging phenomena.
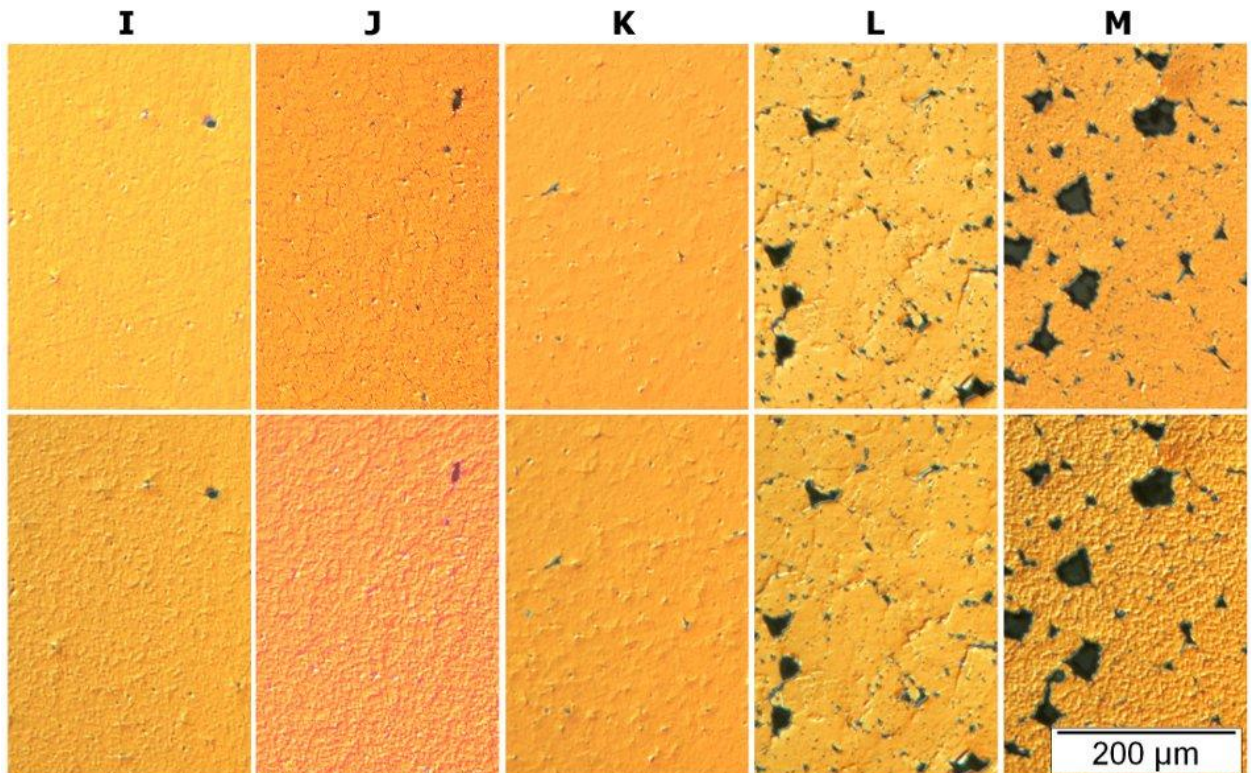
Figure 4.26. Aging of zirconia after 40 minutes of cavitation erosion. Micrographs from first row are taken after the experiment and those from second row one month after the experiment.

In order to clarify whether there is an influence of humidity on the change from tetragonal to monoclinic phase of zirconia, the eroded sample is isolated with grease from the ambient humidity. The grease is spread on the eroded surface just after the experiment and sealed with a sheet of acetate to isolate it from humidity. The aging effect is unchanged with the presence of grease. This indicates that the effect of the ambient humidity is not relevant for the aging effect. The grease used is Asonic GHY 72 from Kluber.

Zirconia "J" shows low loss of surface after 40 minutes of cavitation. Also, the surface develops an extensive change of phase as it is evident with numerous protrusions (Figure 4.26). It is known that the change of phase from tetragonal to monoclinic has an increase of 3-5% of volume (Li et al. 2001). This would give an idea of the depth of the phase transformation. The pick valley value for the protrusions created by the transformation is 50 nm. This means that the height of the protrusions is around 50 nm. As the increase of volume is known, it is possible to calculate the depth of the phase transformation. A depth of 1.6 µm that increases its length by 3 % changes its length in 50 nm. Then the depth of the phase transformation is around 1.6 µm. This is a quick calculation in order to have a good approximation. Other effects as deformation, residual stress, or crack formation are not taken into account for this. It is interesting to point out that the depth of the phase transformation is similar to the grain size expected in zirconia. This suggests that the transformation only affects to the superficial grains. The size of the grains is visible in the thermal etched surface of zirconia "H", Figure 2.12.
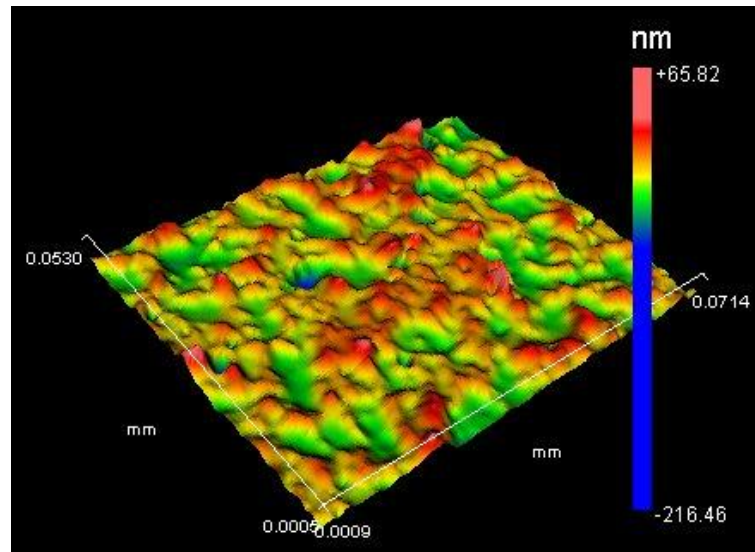
Figure 4.27. Zirconia "J" after 40 minutes of cavitation exposure and
two months of aging.

X-ray diffraction measurements are performed in order to confirm that there is phase transformation on the zirconia surface, see section 2.2. The diffraction angle of the X-ray depends on the distance between atomic planes. Different phases have different interatomic plane distances and diffract at different angles. If the diffraction of the X-rays is in a specific angle, it is possible to conclude the existence of the phase with the interatomic distance that corresponds to that diffraction angle. Also, the intensity of the diffraction gives a measurement of the proportion of that phase in the irradiated volume.
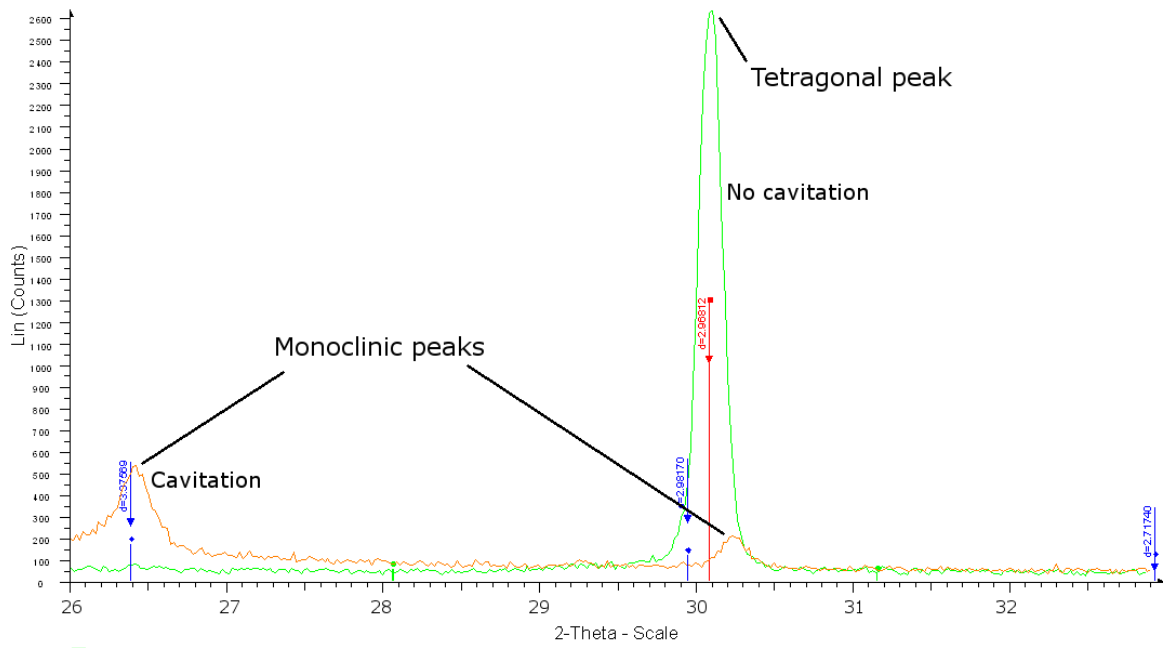
Figure 4.28. X-ray diffraction intensity versus angle for zirconia "I" after 40 minutes of cavitation exposure and 4 months of ageing, and without cavitation.

Figure 4.28 shows the X-ray diffraction angles for zirconia "I" without cavitation and after 40 minutes of cavitation and 4 months of ageing. Zirconia "I" without cavitation shows only tetragonal phase. Conversely, zirconia "I" with cavitation shows only monoclinic phase. This result demonstrates clearly that cavitation produces change of phase in partially stabilized zirconia. In order to understand what is happening during the ageing process, X-ray diffraction measurements are taken after 40 minutes of cavitation, either two days or four months after the cavitation exposure for zirconia "J". Figure 4.29 shows that originally zirconia "J" was tetragonal. After the exposure to cavitation erosion, some tetragonal zirconia is transformed into monoclinic A. The delay in the transformation of zirconia is demonstrated with the appearance of another monoclinic phase in the sample that has 4 month of ageing. This another monoclinic phase is shown as monoclinic B in Figure 4.29. Both monoclinic phases are detected by the software of the X-ray machine. It is concluded that in zirconia "J" the exposure to cavitation erosion produces monoclinic phase A, mainly by the stress caused by the impact of the collapsing bubbles. Also, it is concluded that the partially stabilized tetragonal zirconia transforms into monoclinic phase B spontaneously with the ageing.
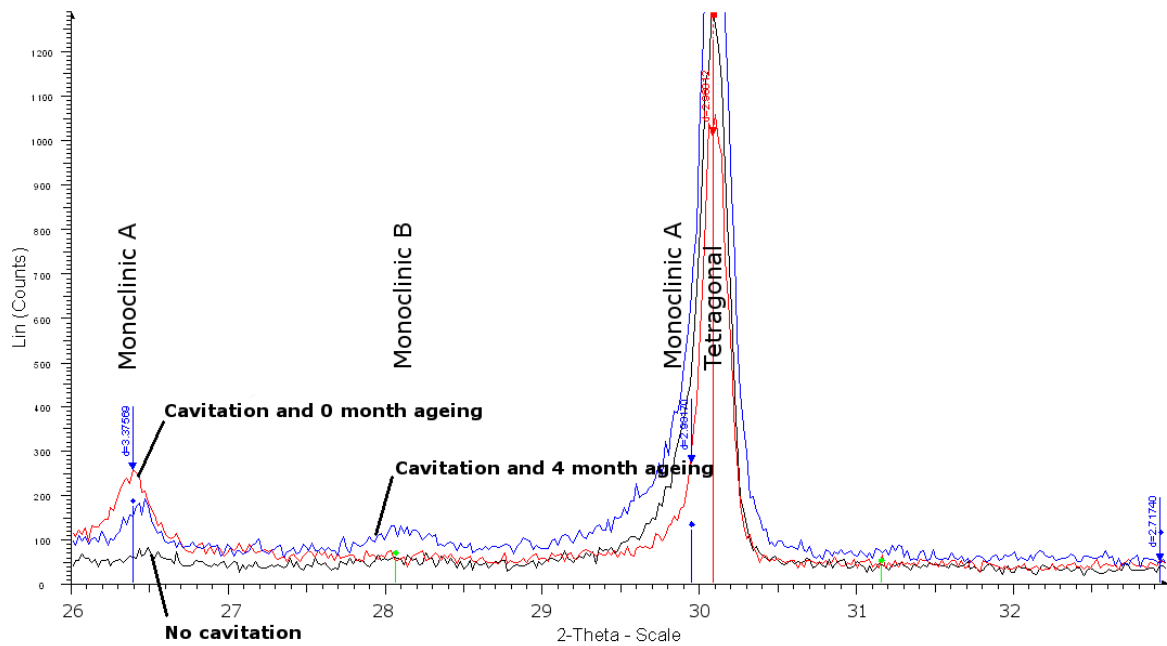
Figure 4.29. X-Ray diffraction intensity versus angle for zirconia "J" with no cavitation exposure; after 40 minutes of cavitation exposure and 2 days of ageing; and after 40 minutes of cavitation exposure and 4 months of ageing.

4.3 Mechanical behaviour of ceramic subjected to various conditions

In order to understand in a better way the mechanical behaviour of the surface of ceramic materials, other wear processes and mechanical stresses are applied to the surface. These experiments aim to produce plastic deformation and residual stresses in order to understand how the material plastically deforms and how the phase transformation of zirconia is related to residual stresses originated by plastic deformation.

4.3.1 _Yield strength of Silicon Nitride under very high contact pressure in rolling contact_

It is known that silicon nitride balls in hybrid bearing normally do not fail, the failure is produce by damage in the steel tracks due to contamination of the oil, degradation of the seals, excessive load or excessive number of cycles. However, a ceramic ball that has a c-crack, normally created by impacts between balls, can produce a fatigue failure because of the growth of the c-crack with the cyclic contact pressure. This has been extensive studied in the literature (Hadfield 1998; Hadfield and Stolarski 1995; Wang and Hadfield 1999, 2000a, 2000b, 2001, 2004; Zhao et al. 2006a, 2006b). However, recently, the use of full ceramic bearing, bearing with ball and tracks made of ceramic, has changed the tribological couple. While in the hybrid bearings, a very high load is limited by and excessive plastic deformation in the race, it is not clear if a full ceramic contact presents some kind of plastic flow on the track before failure. In the rolling contact of steel, if the Yield strength of the steel is achieved, there is a plastic flow of a layer material due to plastic deformation in the subsurface (Bhargava et al. 1985a, 1985b; Hahn et al. 1987; Hearle and Johnson 1987; Merwin and K.L. 1963; Ponter et al. 1985).

In this research there is an attempt to measure plastic deformation in the ceramic track. A technique to measure the track is developed, also a stand is built in order to overcome the difficulties of measuring a track that is not visible. This technique consists on the use of a goniometer in order to locate the ball holder in such way that the track is in the highest point of the ball. Then, the ball is measured on the highest point of the surface that is spotted by the circular fringes. This technique allows measuring the geometry of the contacting track although when it is not visible.
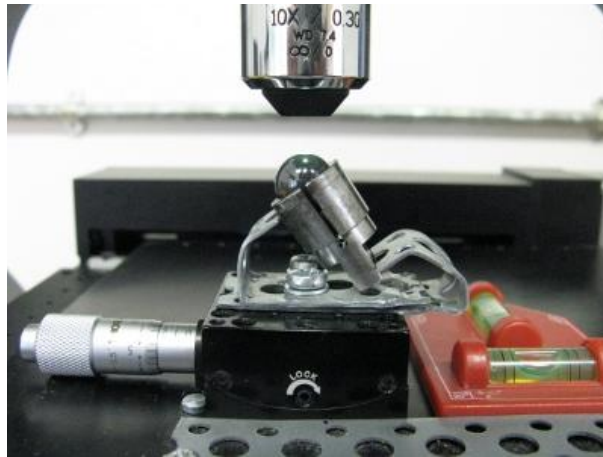
Figure 4.30 Stand to measure the track.

The silicon nitride chosen is silicon nitride "F", see section 2.4. Other properties are given in Table 6.1 of the appendixes. Balls of ½" diameter and grade 10 have been subjected to rolling contact in a modified four ball machine Plint TE-92. The oil used has been Shell Talpa 20. The contact pressure has been calculated by Hertz.

When subjecting the silicon nitride to very high load, using lower and upper ceramic balls, no sign of deformation of the track is found. The track is measured with an interferometer that has a precision up to 0.3 nm. Due to the waviness and roughness of the surface, it is determined that only a deformation of the track bigger than 4-5 nm may be detected. This deformation was not detected. However, it was found that when the contact pressure is similar to the yield strength of the ceramic, the surface of the ceramic fails with a big fatigue spall produced by propagation of a subsurface crack. The fatigue spall was produced in the lower ball, that rotates free. While in the upper ball, where the track is fixed, no deformation was measured. The fatigue spall was produced when subjected the ball to a 5 KN load, that in the four ball machine geometry is 10.3 GPa Hertz's contact pressure.

No superficial deformation was found in any of the experiments. It is known that a grain of ceramic material has dislocations in its crystal structure and they allow plastic deformation through dislocation movement and multiplication (Milhet et al. 2000, 2003; Suematsu et al. 1996). However, the limitation of the plastic

deformation of ceramic materials is due to the grain boundaries. The glassy grain boundary stops the propagation of dislocation and prevents plastic deformation (Wachtman 1996).

Ceramic materials have an elastic behaviour at working stresses, however, the silicon nitride presents a yield strength that has been calculated in different ways in the literature. An interesting way used by literature for this research is by means of a circular contact pressure created by a tungsten carbide sphere because the contact is similar to the experiment in the modified four ball machine. The Yield strength measured values are between 7-12 GPa (Lee and Lawn 1998; Lee et al. 1997).

When subjected the balls to the Hertz pressure of 10.3 GPa in the rolling contact experiment, the balls failed immediately. It is concluded that the yield strength is achieved and that the balls cannot support the stress state created and fail. The failure of the ball is in form of fatigue spall, as shown in Figure 4.31.
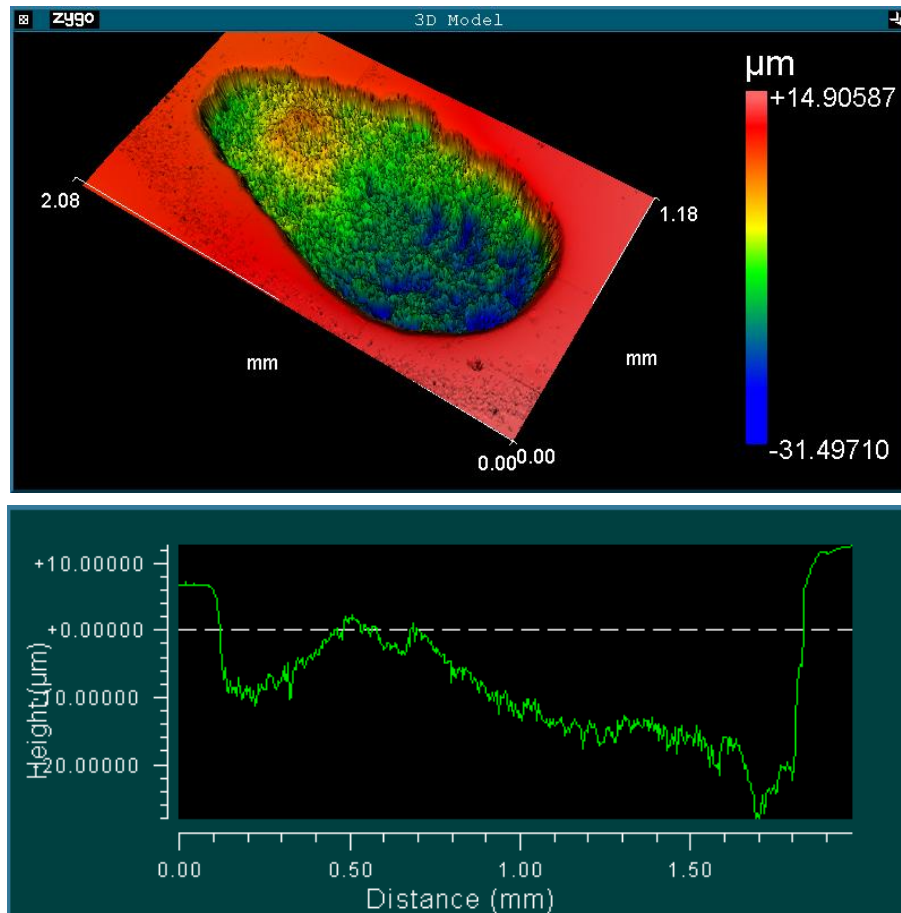
Figure 4.31 Fatigue spall and profile of silicon nitride ball at 10.3 GPa rolling contact. Interferometry.

An interesting discussion about the fatigue spall (Figure 4.31) is to check if the spall was originated in the maximum shear stress region predicted by the theory. This behaviour may conduct to an indirect measurement of the Yield strength in relation with the depth of the spall. According to Hertz's theory, the maximum shear stress is produced at depth of 0.48a (for ν=0.3) and it is in that region where the initiation of the plastic Yield is expected (Johnson 1985). In the experiment, the maximum depth of the crack is 35 μm and the contact radius "a" is 308 μm. Then the region of maximum shear stress is around 149 μm that is much deeper than the deepest point of the fatigue spall. This suggests that the fatigue spall was produced in a local flaw such a pore or micropore rather than in the maximum shear stress region. The possibility of using the depth of the fatigue spall in order to have an indirect measurement of the Yield strength is rejected since the depth of the spall is determined by an arbitrary location of flaws rather than by the mechanical properties

of the material itself. Where the spall is initiated is not at a depth of 0.48a but where a local flaw previously existed. Then, it is not possible to relate depth of spall with contact radius and this with contact pressure.

4.3.2   Wear of Silicon Nitride under very high contact pressure in rolling

contact

During the experiments that are made here trying to measure some minimal plastic deformation, no plastic deformation occurs but a different effect occurs in the rolling contact of silicon nitride ball against silicon nitride ball. The effect consists on the wear of the track due to the running-in condition of the new unworn balls. Wear of the upper balls is detected when new lower balls are used. The wear of the upper ball, the one that has a defined track on it, is measured for different conditions (Figure 4.32). It is found that the important factor for the wear of the track is the surface condition of the balls rather than other parameters as lubricant film thickness. A review of running-in studies for different materials is available in the literature (Blau 2005). The results of the experiments are explained below.
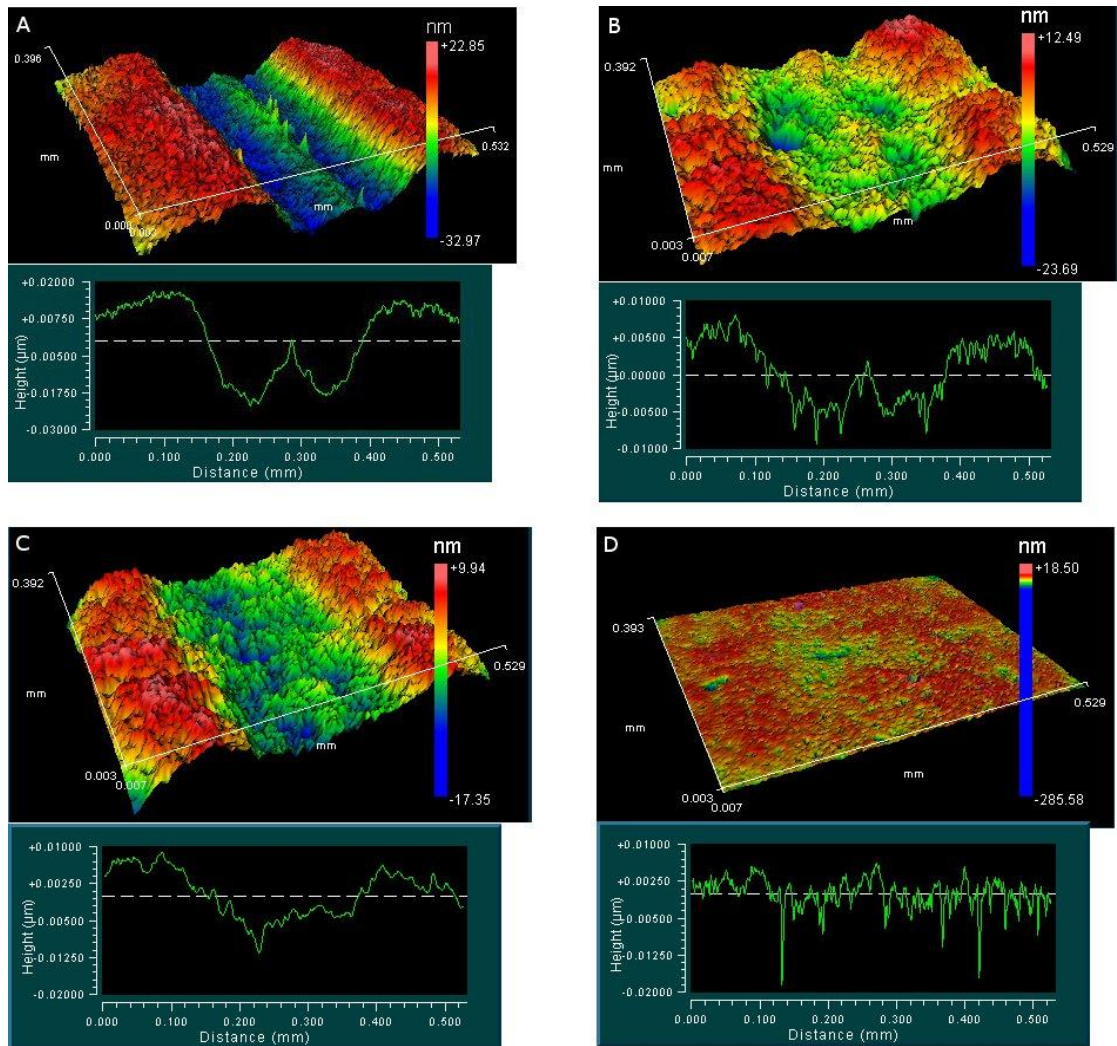
Figure 4.32 Wear of the upper ball track. Condition of the experiments given in Table 4.8. The film thicknesses are 5 nm for A, 14 nm for B, 14 nm for C and 5 nm for D. The four experiments are carried out in this order with the same bath of lower balls that accumulated the transient wear.

The experiments are summarised in Table 4.8. The contact pressure is calculated with Hertz's theory, the film thickness and the film parameter "λ" are calculated according to the Hamrock and Dowson theory, see section 1.2.8.

Table 4.8 Rolling contact experiments pursuing wear measurements.

Test	Speed (rpm)	Oil	Film Thickness (h_0)	λ	Wear depth (nm)	Wear volume (μm^3)
Silicon nitride "F", 760 N (5.5 GPa), 500000 revolutions (1125000 cycles), 40 °C.						
A	300	ISO15	5	1.9	32	135240
B	1200	ISO15	14	4.8	10	41630
C	333	ISO VG46	14	4.8	8	35420
D	83	ISO VG46	5	1.8	~0	~0

The characteristic shape of two parallel groves along the track is explained with the results of the film thickness optically measured in the literature. The film thickness of the lubricant has been measured in the literature in the sliding or rolling contact of a sphere and a transparent disc. It presents a typical "horse-shoe" shape when measured with interferometry (Stachowiak and Batchelor 2001). This "horse-shoe" shape indicates that the region of minimum thickness is not in the centre of the contact but in the two lateral regions. This is caused by the fact that the lubricant escapes from the contact by these sides. Furthermore, the width of the wear track in the experiments is around 285 μm while the Hertz's contact radius is 328 μm. This also supports the explanation that the wear is produced in those regions where the film thickness is minimum. This is also consistent with micrographs published in the literature where the polishing of silicon nitride rolling against steel is produced mainly in both sides of the track (Kang and Hadfield 2003).

The experiments presented here are carried out with the same bath of lower balls. Other experiments were carried out at first instance casting a similar result using silicon nitride "E" and "F". It was expected to have a wear rate proportional to the film thickness; however, the result indicated that the wear rate decreases as the rolling distance of the lower balls increases. Hence the determinant factor for the wear rate is not the film thickness but the running-in condition of the lower balls. It is important to remark that the roughness of the lower balls is measured with the interferometer profilometer. The measures of roughness of the lower ball do not change and they remain in a value of around 2 nm (R_a). This is caused by the fact that the interferometer profilometer measures the average height of the area within

the pixel. Then, spikes and other characteristics smaller than the size of the pixel are not measured. The minimum size of the pixel in the interferometer profiler used here is 640 nm. Although the measure of the roughness with the interferometer profiler does not change, this does not mean that the surface is not changing. It is concluded that the changes of the surface are smaller than the pixel sizes and to proper measure this changes it is necessary to measure the surface with an Atomic Force Microscope. This is out of the scope of the present research.

Also, the technique used here allows measurements of wear volume as small as 20,000 μm^3 with a high degree of repeatability. The weight of such volume is 0.06 µg that is smaller than the repeatability of commercial microbalances that is around 1 µg in the best case. Hence, the technique developed here is more precise than the methodology used commonly in the literature.

The wear of the upper ball depends on the state of the surface of the lower balls. The new unworn lower balls produce a transient wear in the upper ball. After the running-in finishes, the wear rate drops almost to zero. This is consistent to what has been reported in the literature. Chao et al measured the transient wear of silicon nitride in rolling contact. They used a ball on rod experiment with the rod of 9.525 mm diameter rotating at 3600 rpm, hence the film thickness may be thicker than in the experiments made here although they tried to get boundary conditions. They measured an initial high wear rate that drops to zero after some rolling distance (Chao et al. 1998). In the experiments shown here the wear rate is clear at the beginning but, in the last experiment the wear rate is practically zero. This is caused by the transient wear of the lower balls. Once the lower balls passed through their transient wear no more measurable wear is produced in the upper ball. Also, this is consistent with the good performance attributed to the silicon nitride in boundary conditions and dry conditions (Popp and Sternagel 1999; Sanders et al. 1999).

4.3.3 *Zirconia surface stability subjected to polishing wear*

As stated in section 4.2, zirconia shows a delay in the phase transformation from tetragonal to monoclinic when subjected to cavitation erosion. In this section, the occurrence or not of this delay is study when the zirconia surface is polished.

The polishing effects on the surface are similar to the effects of cavitation erosion. It is known that polishing of the surface with diamond slurry produces abrasion lines on the surface with its correspondent residual stress associate to the plastic deformation produced in the abrasion (Eigenmann and Macherauch 1995). Also, the diamond, as third body abrasion, may produce microcracks on the surface (Stachowiak and Batchelor 2001). Hence, the similarities to cavitation erosion are that both produce a plastic deformation of the surface, a residual stress state and microcracks. As the residual stress is considered the responsible for the phase transformation (see section 5.2), there is a possibility that polishing has the same "activation effect" on the surface that may produce a phase transformation afterwards. This is investigated in this section.

The samples of zirconia are "I" and "J", more information can bee found in section 2.4. These two kinds of zirconia are chosen because they are bearing grade zirconia and one is stabilized with yttria and the other one is stabilized with magnesia. Also both of them show phase transformation delay as explained in section 4.2,.

The zirconia balls are cut with a diamond cut-off wheel, Struers 330-CA, in a precision cut-off machine, Struers Accutom-5. After that, they are moulded in a holder made of Buehler-MET conductive powder. Then they are polished with polycrystalline diamond suspension of 6 µm size, Buehler Metadi Supreme. The surface is micro photographed with polarizing filter after the polishing process is completed. Then, they are stored for several months and the surface is micro photographed again with the same polarizing filter. One of these micrographs is shown in Figure 4.33.
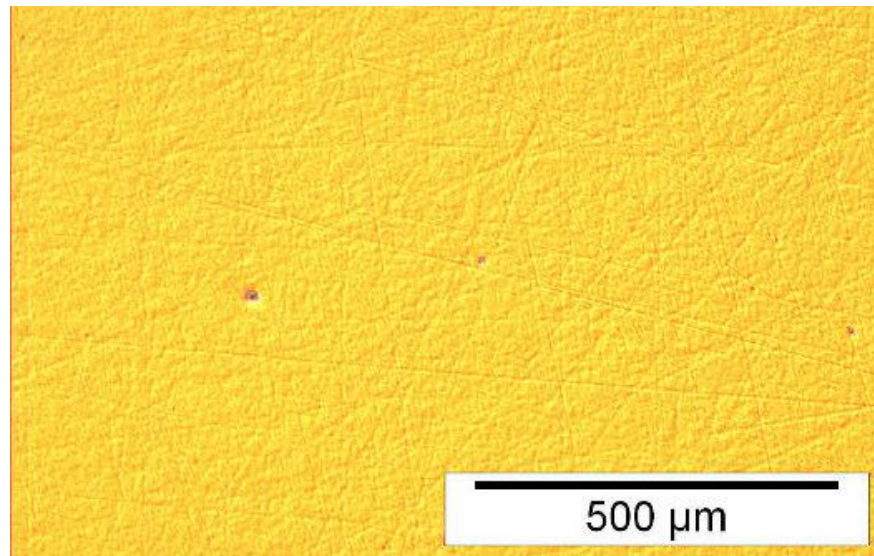
Figure 4.33 Micrograph of zirconia surface after polishing with 6 µm
diamond slurry. Zirconia "J" sample.

The same process is repeated with two more samples of each zirconia, but this time
the polishing with 6 µm is followed by another polishing with 3 µm polycrystalline
diamond suspension. In this case, the finishing of the surface is better. Also,
micrographs are taken.

None of the samples shows any phase transformation delay visible with the
polarizing filter. After several months, the surface remains unchanged from its
original state. As a conclusion, the surface is not "activated" by polishing in despite
it is "activated" by cavitation erosion creating subsequent changes. This is attributed
to the fact that the residual stress field associated with the polishing is not strong
enough to drive these changes.

4.3.4 *Zirconia surface stability subjected to a distribution of microindentations and its associated residual stress.*

It is known that a Vickers indentation produces plastic deformation, an associated
residual stress and in the case of ceramics, a crack in the corners. This has been
studied somewhere else (Fett et al. 2005). For this reason, there are, again,
similarities with the cavitation erosion, since both mechanisms produce plastic
deformation, residual stress and cracks. In comparison to the polishing process, the

residual stress is much more severe in the case of indentation than in the case of polishing. Furthermore, there is a possibility that indentation may "activate" the surface and produce subsequent phase transformation along the time. Although the experiments of polishing made here do not produce this "activation" of the surface, in this section it is study if the distribution of indentations "activates" the surface.

Different distributions of microindentations are made in samples of materials "H", "I" and "J", see section 2.4 for more information about the materials. Figure 4.34 shows an indentation distribution. In this case the Vickers microindentations are made with a load of 25 g. Other loads are used in other samples.
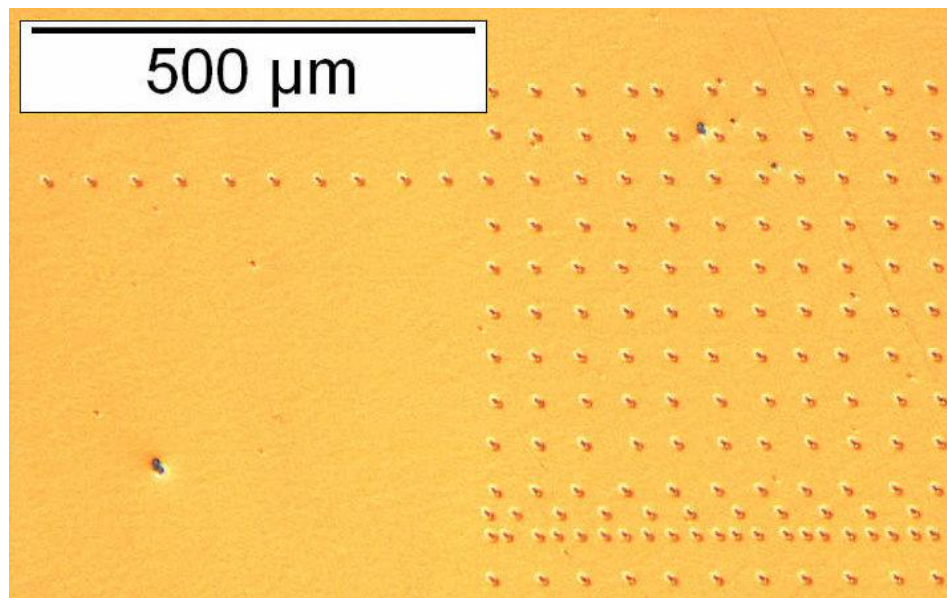
Figure 4.34 Micrograph of zirconia surface with the distribution of indentations.
Zirconia "I" sample.

The experiments show that there is no change of the surface along the time. Micrographs are taken one month later and no new protuberances or change of roughness occurs. The surface is not "activated" by the indentations. This result of no "activation" is the same as the result from polishing. Neither polishing nor indentations "activate" the surface and produce phase transformation delay.

4.3.5 _Zirconia surface stability subjected to lapping wear_

In the same way as made before with polishing process and distributions of indentations, the zirconia surface is subjected to lapping wear. The lapping process is a manufacturing process of balls. The balls are pressed with a specific load between two discs. One of the discs rotates while the balls are wet with diamond slurry. The diamond acts as a third body in the contact of the balls with the disc and produces the typical third body abrasion removing material. Depending on the load, the diamond size, speed and other parameters, it is possible to vary the cutting conditions, the material removal rate and the finishing (Kang and Hadfield 2001b; Kang and Hadfield 2005). The lapping machine used here is described somewhere else (Kang and Hadfield 2001a).

The diamond slurry used is 45 µm of size (Buehler Metadi Diamond Suspension). Then, the abrasion and plastic deformation tip produced in the ball is much more severe than that produced in the polishing process. For this reason, the residual stress field associated with this plastic deformation might be strong enough to "activate" the surface and drive phase transformation after the lapping machining is finished.

The materials chosen for this experiment are zirconia "I" and "J" bearing balls of 12.7mm diameter. See section 2.4. The balls were subjected to 6 hours of lapping machining but it was found that the wear and roughness of the balls are excessive and this makes difficult the comparison of the state of the surface. Consequently, a lapping process of 10 seconds is chosen in order to easily detect phase transformation in balls that has both worn and original surface. Figure 4.35 shows the state of the surface after 10 seconds of lapping. No phase transformation delay is detected in this experiment also.
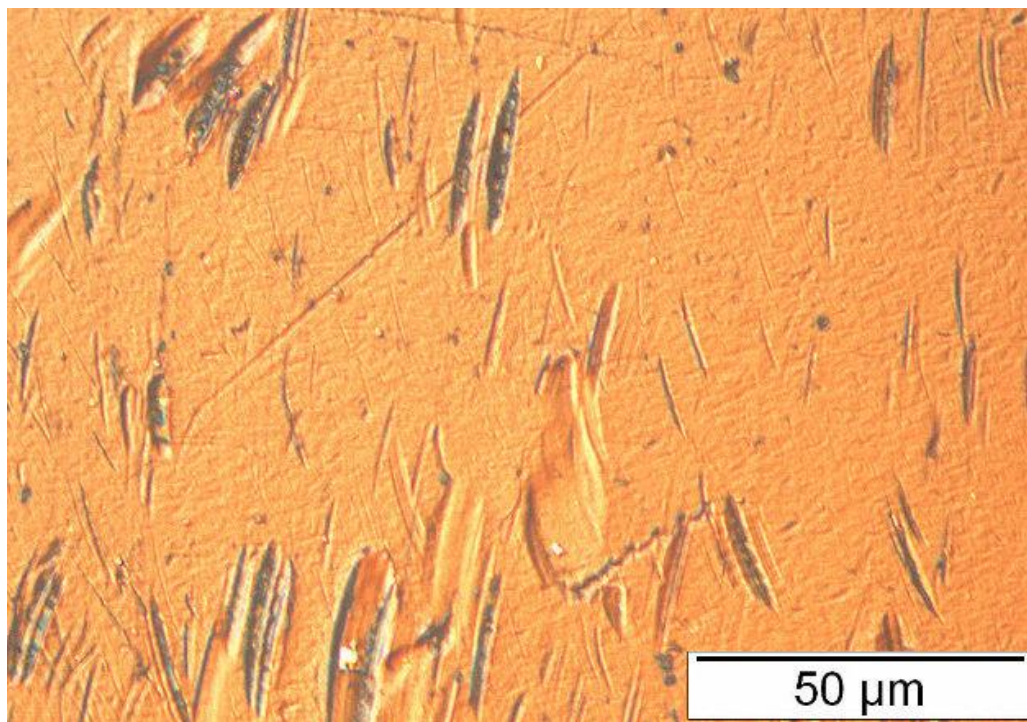
Figure 4.35 Micrograph of zirconia surface after 10 seconds of lapping process. Zirconia "J" sample.

Chapter 5   Discussion

In this chapter, a discussion of the results, performance and behaviour of the materials is presented. Also, the behaviour of the cavitation clusters is discussed as an important part of the research. Some of the contributions are presented with conclusive results. However, there are other contributions that are presented as the best explanation according to the established knowledge, the results and the limits of the laboratory devices and measurement apparatus.

5.1   Discussion of cavitation erosion of ceramics

The initial surfaces of the samples, although polished following the same methodology and sometimes simultaneously, present different topography and roughness depending on the sample material. This is due to the mechanical properties of the surface and the grain size. One of the main reasons for these differences in the roughness is that some materials lose grains in the polishing process. Generally, a grain whose tip has almost been polished away is detached from the surface creating a pit. Hence, the quality of the polished surface is degraded. Conversely, other materials that have the grains cohesively fixed to the bulk material do not present detachment of grains in the polishing and their finishing is superior (Figure 5.1). Table 5.1 shows the roughness of some samples. It is also interesting to note that some materials present better polishing behaviour than others. For example, silicon nitride "A" is quicker to polish than other silicon nitrides and its finish is higher quality, without presenting any detachment of grain tip. The explanation to this behaviour might be in a more consolidated microstructure, with finer grains, better attached to each other, less degree of porosity and some chemistry reaction between the sintering additives, silicon nitride and water. It is known that there are chemical reactions between water and silicon nitride in the wear process (Xu et al. 1997). The detailed explanation of this different result in the polishing process is out of the scope of the present research. However, it is interesting to point out that silicon

nitride "A" presents also the best performance in cavitation resistance among the silicon nitrides.
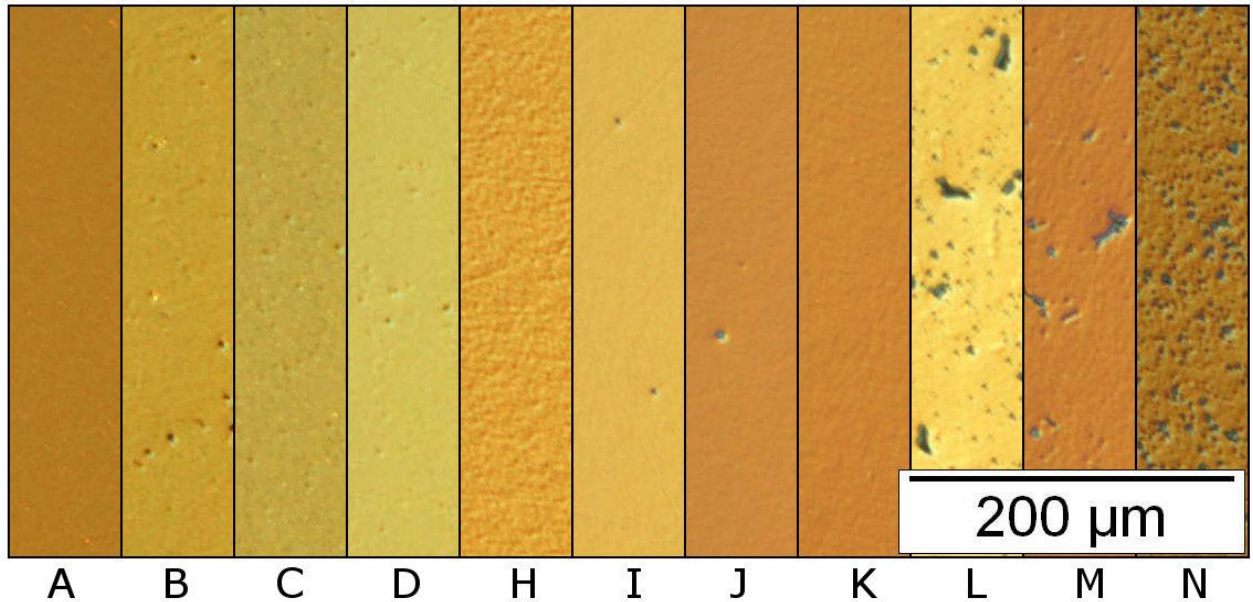
Figure 5.1 Polished finishing of different samples. "A" "B" "C" and "D" are silicon nitride; "H", "I", "J", "K", "L" and "M" are zirconia; and "N" is alumina.

Table 5.1 Roughness of samples after polishing and before tests.

	R_a (µm)	rms (µm)
Silicon nitride "A"	0.001	0.002
Silicon nitride "B"	0.003	0.003
Silicon nitride "C"	0.001	0.003
Silicon nitride "D"	0.008	0.010
Zirconia "H"	0.003	0.004
Alumina "N"	0.019	0.060

In terms of cavitation erosion resistance the best materials are silicon nitride "A" and zirconia "H" among those that have been tested in section 4.1.5. The criteria used here is surface loss as explained in section 4.1.5. The erosion in the test conditions for the first 120 minutes is minimal in both materials (Table 4.4). Then the time is

extended to 180 minutes to achieve differences (Table 4.5). Zirconia "H" is the best material in terms of cavitation erosion resistance.

It is important to note that silicon nitride "A" has a cavitation resistance much better than the rest of silicon nitrides. Also it is shown before that silicon nitride "A" is easier to polish and the quality of the finish is better than in the other silicon nitrides. Conversely, the material with the worst cavitation erosion performance is alumina (Table 4.4) that, also, has the worst finish during polishing. In the case of alumina the constant loss of grain tips from the surface make it difficult to achieve a mirror finish (Figure 5.1). Hence, there is evidence that the capabilities of the material to hold the grains in both polishing and cavitation erosion are related. This capacity of the material to hold the grains (without allowing a crack to grow and to detach it) has a relationship with the fracture indentation toughness. It is expected that the higher the fracture indentation toughness the higher the capacity to retain the grains. According to the values presented in Table 2.2, zirconia "H" has the highest fracture indentation toughness (10.5 MPa√m), the silicon nitrides "A", "B", "C", and "D" have similar fracture indentation toughness with a value around 7 MPa√m and finally alumina has the lowest value (3.8 MPa√m). There is some obvious relationship between the fracture toughness and the cavitation erosion resistance, but this does not explain the behaviour itself since silicon nitride "A" has even a lower value of fracture toughness than silicon nitride "C" but its cavitation erosion resistance is much better. The same situation occurs in relation with the bending strength. The bending strength has the highest value for zirconia "H", while the silicon nitrides have similar values and the value for alumina is much lower (Table 2.2). However, in this case the value of bending strength for silicon nitride "A" is higher than for the other silicon nitrides. Tomlinson and Mathews (1994) checked a simplification of a previous model intended to relate the erosion resistance of ceramic to particle impact. The simplified model has taken into account the hardness H; the coefficient E/H as an important parameter of micro-plastic deformation; and the fracture toughness K_C. They concluded that there is only a general trend of cavitation erosion resistance in relation with these values, but other factors play an important role. As a general trend, the cavitation erosion resistance is inversely proportional to the fracture toughness in ceramics. This conclusion is consistent with the results shown here.

The other zirconia materials have not been tested for the ranking of cavitation erosion resistance but results from other experiments show a similar behaviour. The cavitation resistance of ball bearing grade zirconia is high, as it is possible to observe the scarce amount of surface lost after 40 minutes of cavitation exposure. The comparison of the first row of Figure 4.26 with Figure 5.1 shows that the amount of surface lost is reduced for zirconia "I", "J", and "K" and close to the expected surface lost in zirconia "H" as shown in Figure 5.2, and they have better cavitation resistance than silicon nitride "D". Conversely, zirconia "L" and "M" show big regions where the dislodging of grains has coalesced and they are expected to have a poor cavitation erosion resistance. It is important to point out that these two materials are also difficult to polish, and they present a poor finish after polishing as shown in Figure 5.1. Zirconia "L" is a milling ball material, where mechanical properties are less relevant than in bearings because they are used to mill and to disaggregate samples in a cup in order to make analysis of its components. They can be easily removed or replace by other material balls depending on the samples to analyse. Zirconia "M" is a ball bearing material mainly directed to the sport and leisure industry.
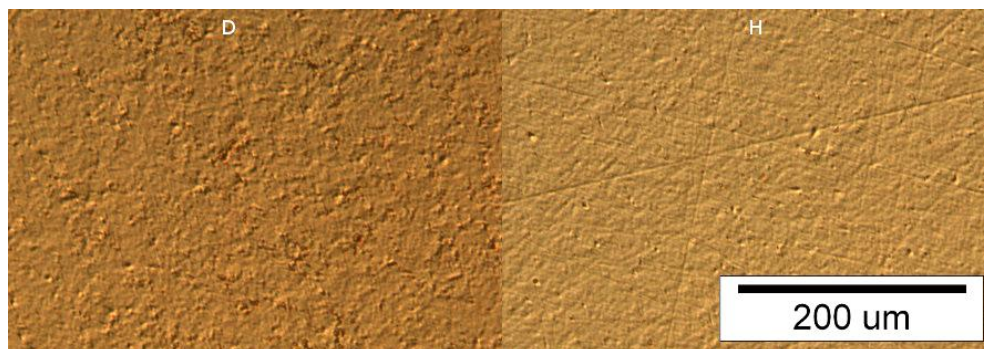
Figure 5.2. Surface state after 40 minutes of cavitation erosion for silicon nitride "D" and zirconia "H".

5.1.1 *Pseudoplastic deformation pits.*

One important contribution to knowledge of this research is the appearance of pseudoplastic deformation pits when the polished surface of silicon nitride or zirconia is exposed to cavitation erosion. These pits do not seem to have been

previously reported. The pits appear visible with the polarizing filter of the optical microscope that highlights the local depression (Figure 4.1). Also they are visible in the video monitor image of the interferometry profiler because they are highlighted with the optical fringes.

The average measurement of the pseudoplastic deformation pits are given in Table 4.1. The size of the pseudoplastic deformation pits is clearly bigger in silicon nitride than in zirconia. This phenomenon is repeated with the other zirconia samples apart from zirconia "H". Hence, typical sizes for the biggest pseudoplastic deformation pits in silicon nitride have diameters of 8-12 μm, depths of 0.05-0.09 μm and volumes of 2-3 μm^3. Conversely, the typical sizes for the biggest pseudoplastic deformation pits in zirconia have diameters of 3-6 μm, depths of 0.03-0.05 μm and volumes smaller than 1 μm^3. It is interesting to note that the silicon nitride with smallest pseudoplastic deformation pit is silicon nitride "A".

The comparison of the pseudoplastic deformation pits in ceramic with those in steel clarifies the mechanism that creates the pit. During the cavitation process numerous cavities are created and collapsed, however, only those that are close enough to the surface, damage the surface. Most of the bubbles collapse in the bulk of the fluid without creating any damage. Depending on the surface, the impact severity of some bubbles that collapse close to the surface passes a threshold that creates damage. In the case of steal it is easily recognised that there are some impacts that create big deformation pits and also there are weaker impacts that create smaller deformation pits. This is due to the size of the bubble; the distance from the centre of the bubble to the surface; and the way it collapses and generates the jet stream. It is obvious also that one pit is created by only one impact, and that the pit is not produced by fatigue on the surface. The evidence is that in the first second of exposure to cavitation, the number and size of created pits is the same as that during the second second of exposure. The number of pits changes linearly with time in the first seconds. After the first seconds, a work hardening effect occurs on the surface of the steel due to the plastic deformation of the pits and the size and number of plastic deformation is reduced as evidenced in Figure 4.15. The same linearity behaviour with the time of the number of pits on ceramic is shown in Table 4.3. The number of pits created in

the first 15 seconds (0s-15s) is very similar to the number of pits created in the second 15 seconds (15s-30s). That behaviour demonstrates that the pits are created by the single impact of a bubble.

Other possible explanations about the creation of the pits, such that they are created but thermal stresses, are unlikely. It is known that the collapsing bubble can produce high temperatures, overall if it has some amount of air to compress, but these temperatures are located in highly reduced points and for very short times as calculated by Fujikawa and Akamatsu (1980). In order to create thermal stresses on the ceramic surface would be necessary to transmit the heat from the core of the bubble through the boundary layer of the liquid to the ceramic surface. Besides, the presence of the jet stream reduces the chances to get a point of highly compressed air that achieves a high temperature. The high temperatures are achieved with the spherical geometry. The jet stream due to the presence of a close surface prevents the spherical geometry (Plesset and Chapman 1971). This jet will spread the air, avoid a central high compressed point and prevent high temperatures. The extreme high temperatures are achieved when the air that is presented in the vapour bubble is compressed in the central point of the collapsing bubble. This central point does not exist when the bubble collapses close to a surface since the jet stream goes throw the centre. Consequently, this explanation of thermal fatigue to create the pits is rejected. This is not the main mechanism that creates the pits. The pits are created by the impact of single bubbles.

The size of the diameter of the pits on steel is similar to the size of the diameter of silicon nitrides. The size on steel is around 11-15 µm, which is not much bigger than in silicon nitride. Again, this suggests that the mechanism creating the pseudoplastic deformation pits in ceramics is the same that in steel: the single impacts of bubbles.

In steel, the softer the surface is, the bigger the plastic deformation pit is. Conversely in ceramics this is not true. The typical hardness of the silicon nitride tested here is 1500-1600 kg/mm^2 while the typical hardens of the zirconia is 1250-1270 kg/mm^2. However the pseudoplastic deformation pits are much bigger in silicon nitride than in zirconia. Then, it is possible to think that the mechanism that produces the pits is

different from just deformation of the surface due to the impact as it is in steel. Here, this mechanism is discussed.

It is known that the plastic deformation of a single crystal of a ceramic produces work hardening on the surface as it has been reviewed in section 4.1.6. It is demonstrated that there is a permanent deformation of the surface after cavitation exposure. However the surface is softer instead of harder (Figure 4.21 and Figure 4.22).

On the other hand, it is known that the cavitation erosion process of ceramics is mainly intergranular crack growth due to fatigue and detachment of the grains (Litzow et al. 2006; Niebuhr 2007; Tomlinson et al. 1999). Hence, there is an initial time when these cracks appear and start to grow. Furthermore, some of the impacts of the collapsing bubbles produce high enough stress on the surface to create a crack, or several of them, that in subsequent impact would grow and finally, with the time, detach a grain.

The best explanation for the softening effect on the surface is that when the surface is cracked, there is a release of stress in the crack during the indentation. Then, the grains are less constrained and can deform more easily. For this reason, when the tip of diamond to produce the indentation presses the cracked surface, the footprint that creates is bigger than in a surface that has no cracks. The apparent hardness of the surface is lower. This is the best explanation for the softening effect. It is important to remember that although the surface looks like very rough with the optical microscope using polarizing filter, it is in reality quite smooth when it is seen without polarizing filter or when it is measured in the 3D profiler. For such reasons, it is not expected that slight changes of the flatness of the surface may alter significantly the value of the hardness. Actually, it is a common practice to measure the hardness on surfaces with lower flatness than the cracked ceramic surface. Other causes for this softening effect such as the chemical reaction of the surface in water are dismissed as these are not consistent with the known chemical stability of ceramics. The only explanation that is consistent with the established knowledge of ceramics and indentations is that the surface is cracked.

It is not possible to see these small cracks in a ceramic surface with the optical microscope. Also, the SEM images taken did not show the cracks. Even the corner cracks of indentation that are used to measure the fracture indentation toughness could not be seen. This is due to the lack of contrast in the SEM images; the difficulty related to the fact that ceramic is not conductive and needs a coating; and the small size of the cracks. In an attempt to overcome these difficulties, dye penetrant liquids were used.

Dye penetrant liquids are commonly used to detect surface cracks in aviation and other industries. A fluorescent liquid is spread on the surface to inspect. Then, the liquid penetrates in the cracks. After that, the surface is cleaned, leaving the liquid inside of the crack, which eventually leaks out and becomes visible with ultra violet light. This technique was used to detect the small cracks that appear in the cavitation erosion. However, the technique was not successful. No crack was detected. Furthermore, some indentations were made on the surface in order to create the cracks in the corner that are normally used to measure fracture indentation toughness. The corner cracks were not detected either. Figure 5.3 shows the dye penetrant inspection on silicon nitride "A". Point "A" is a Vickers indentation where there is no visible crack in the corners. Points "B" and "C" are pseudoplastic deformation pits. Points "D" and "E" are porosity or surface flaws. The technique of dye penetrant inspection is not valid to detect such a small cracks as those presented here.
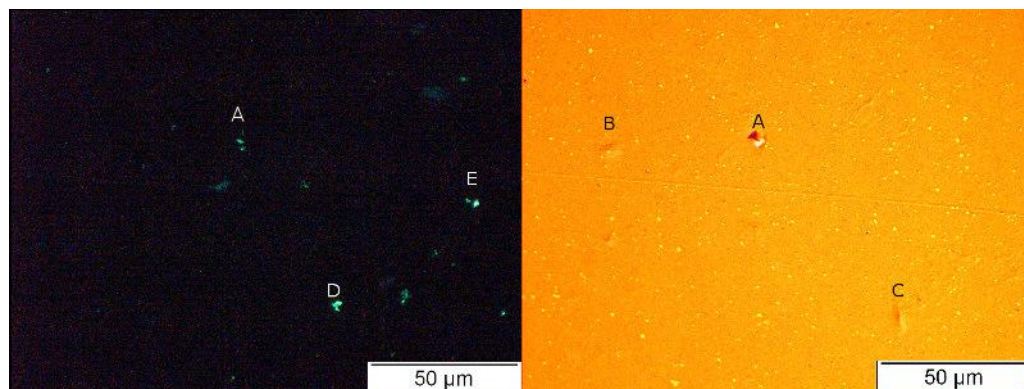
Figure 5.3. Dye penetrant inspection on the surface of silicon nitride "A" and same surface with polarizing filter.

In order to understand the mechanism of plastic deformation within silicon nitride, the surface of ball bearing has been subjected to extreme high loads in rolling contact. Despite the use of interferometry to detect small changes of the surface with a height as small as 5 nm, no plastic deformation is detected, as explained in section 4.3.1 and 4.3.2. The glassy boundary prevents the movement of dislocations and constrains the slip planes. In the same way, it could be expected that no deformation can happen when the ceramic surface is exposed to cavitation. However, the permanent deformation that is obvious in the pseudoplastic deformation pits implies a different mechanism to withstand the pressure that the one to withstand high pressure contact between ball.

The hardness indentation of ceramic surface is a good example of plastic or pseudoplastic deformation on the silicon nitride and zirconia surfaces. It is called pseudoplastic deformation because the plastic deformation is related to the creation and propagation of cracks. Otherwise, the constraint of the intergranular glassy phase would prevent the movement of slip systems. The grain size is shown in Figure 5.4 where it is possible to see the intergranular phases. The materials are ordered from finest grain to coarsest in Figure 5.4. The size of the grains are submicron for silicon nitride "A", "B", "C" and zirconia "H", and coarser for silicon nitride "D". The diameter of pseudoplastic cavitation pits for zirconia are 3-6 μm and for silicon nitride 8-12 μm. Conclusively the size of the pit is not directly related to the size of the grain since one pit cover a good amount of different grains and intergranular borders. Furthermore, the size of the pseudoplastic pit is similar within silicon nitrides despite the grain sizes are dissimilar containing the finest and the coarsest. Zirconia "H" has the smallest pseudoplastic deformation pit while the grain size is intermediate respect the values of silicon nitride grain sizes.
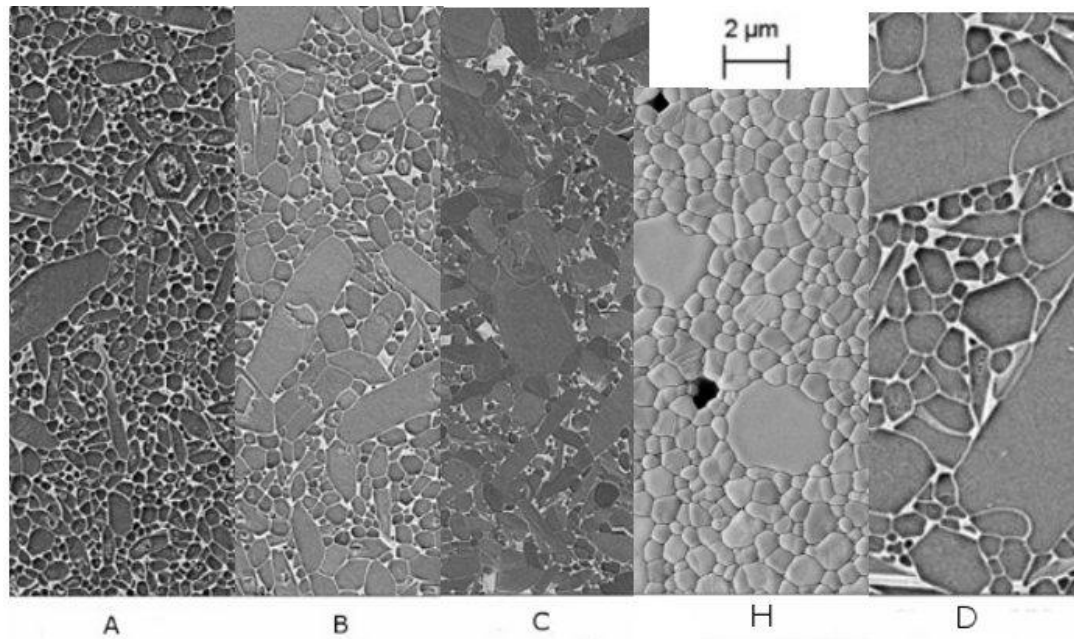
Figure 5.4. Comparison of the microstructures and grain size of silicon nitride "A", "B", "C" and "D" and zirconia "H". Composition made with Figure 2.5, Figure 2.6, Figure 2.7, Figure 2.8 and Figure 2.12 from SKF.

The best explanation for the creation of pseudoplastic deformation pits coherent with the experimental results and the established knowledge is that a pit is created when the surface is deformed by the impact of one bubble in a grade severe enough to create cracks in the intergranular phase. Then these cracks release the slip systems in the grain crystals allowing a small plastic deformation within the grains that will remain after the impact has concluded.

This explanation solves the questions related to the pseudoplastic deformation pits that are: (1) Why are the pits bigger in silicon nitride than in zirconia although zirconia is softer? ; and (2) Why is the number of pits smaller in zirconia than in silicon nitride? The answer to the first question is that the creation of cracks in zirconia is harder and the same impact creates less amount and smaller size of cracks in the intergranular phase of zirconia than in silicon nitride. Then the amount of plastic deformation allowed is smaller in zirconia since the size and number of slip planes released is smaller. The answer to the second question is that the threshold to create cracks in zirconia is higher than in silicon nitride, then, the number of collapsing bubbles that overpass that threshold is smaller in zirconia than in silicon nitride. On the other hand, this explanation is consistent with the softening effect of

the surface exposed to cavitation erosion. The creation of cracks reduces the apparent hardness of the surface.

Figure 5.5 - Figure 5.8 show the explanation for the creation of pseudoplastic deformation pits. Figure 5.5 represents a section of the original surface; Figure 5.6 shows the possible slip planes that are released when some cracks, represented by double line, are created. The presence of cracks release slip planes in the individual grains of the material and allow them to deform plastically. Slip planes are planes defined by the atomic crystal structure where the relative movement of the two parts of the grain divided by the plane is possible due to dislocations. Often, the slip planes are not completely planar and are called slip surfaces. In Figure 5.5 the slip planes are constrained and no plastic deformation is possible. When the collapsing bubble impacts the surface, the surface is elastically deformed (Figure 5.7). This elastic deformation creates a tension stress on the surface that produces cracks when a threshold is passed. Then, the cracks are produced and the grains are allowed to deform plastically driven by the water pressure according to the slip planes that have been released (Figure 5.8). This plastic deformation occurs at the same time as the surface is still highly elastically deformed. The surface (plastically deformed) fits the new geometry of the bulk material (elastically deformed). Later, the pressure from the collapsing bubbles ends and the bulk material tends to return to its original geometry but it is not totally allowed by the new surface plastically deformed. Consequently, the result is a surface that has suffered a local plastic deformation, creating the pit and creating a region with some residual stress. The residual stress is created because the plastic deformed surface fits the elastically deformed bulk, and when the pressure of the collapsing bubble disappear, the bulk tends to go to the original state, but the new surface does not match that geometry and creates a residual stress state, with compressive and tensile regions within the pit and its surroundings. This residual stress discussion is further supported with the zirconia results discussed in the next section.
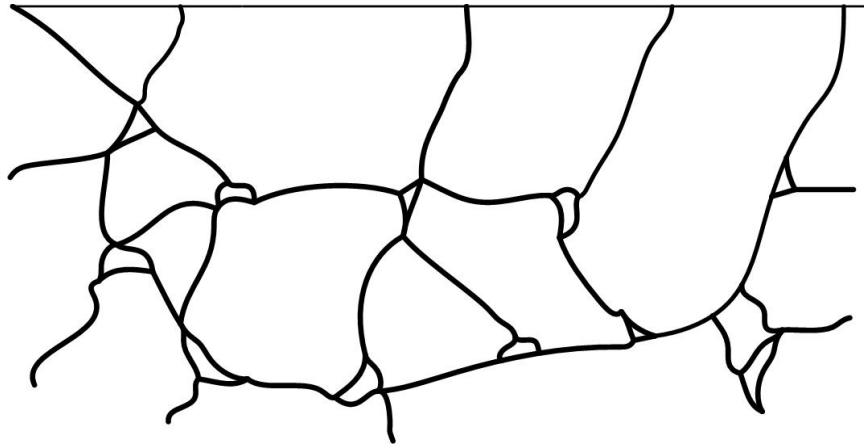
Figure 5.5. When there is no crack, the slip planes are constrained by the intergranular phase.
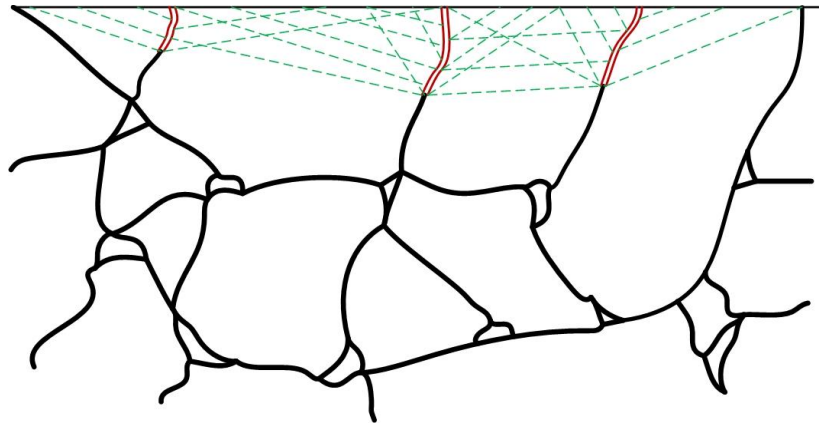
Figure 5.6. The cracks in the intergranular phase release the slip planes.
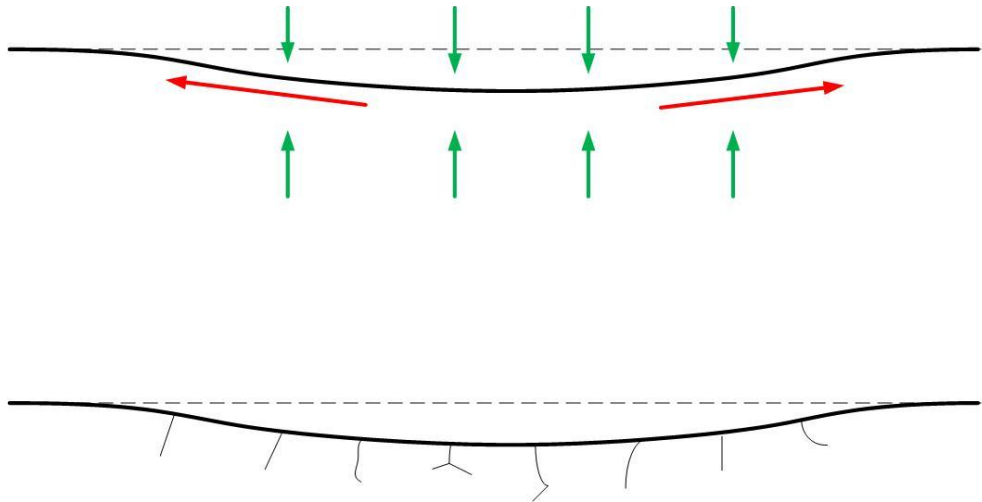
Figure 5.7. The water pressure deforms elastically the surface and creates cracks.
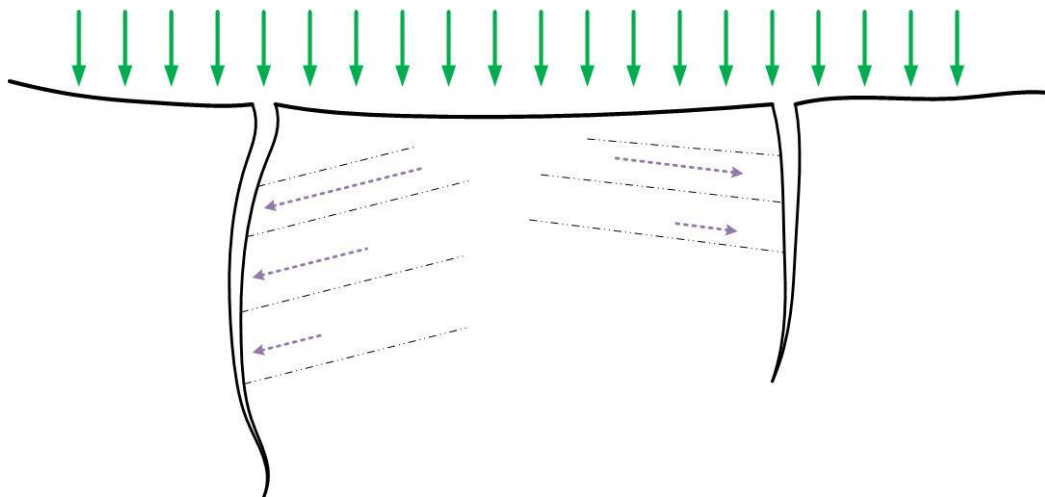
Figure 5.8. The water pressure deforms plastically the grains when the slip planes are released by the cracks. During this stage, the surface is highly elastically deformed.

Alumina "N" is harder than the silicon nitrides and zirconias tested here. Also it is more brittle than them. The hardness of alumina "N" is 1828 kg/mm^2, the fracture indentation is 3.77 MPa√m and the bending strength is 300 MPa. When alumina is exposed to cavitation, the surface develops quickly cracks and dislodging of grains. This behaviour is easily visible in Figure 4.13 and Figure 4.14, where the creation of cracks and dislodging of grains happens in the first minutes within the small amount

of surface due to the reduced angle of view of the highest magnification objective. It is also possible to see in the first seconds of exposure to cavitation some change on the surface with the polarizing filter. These changes are accounted in Table 4.3 with together the pseudoplastic deformation pits. But it is not clear if these changes are pseudoplastic deformation pits or grains that are partially detached from the bulk of the surface and for such reason they present another colour with the polarizing filter. It is also expected that a reduced amount of plastic deformation may happen within this grains. However, the difference between alumina and the other ceramics is that the mechanism in alumina is mainly cracking and partial or totally detachment of grains. While in the other ceramics, the detachment of grains only happens after a longer fatigue process of the surface. The pseudoplastic deformation pits of the ceramics do not lead to a quick detachment of grains. Conversely, the cracks in alumina are easily visible in the optical microscope due to the size of the crack. An impact of a bubble that in silicon nitride or zirconia may produce a pseudoplastic deformation pit, in alumina produces a partial dislodging of the grain as it is visible in Figure 4.13 and Figure 4.14. This is supported by the limited number of changes visible within the first seconds of cavitation exposure.

5.2 Discussion of phase transformation delay

As demonstrated in section 4.2, there is a transformation delay of tetragonal zirconia to monoclinic after cavitation exposure. When the surface of partially stabilized zirconia is exposed to cavitation, the eroded surface suffers some spontaneous transformation in the following weeks when stored at room temperature. This happens in the absence of ambient moisture since some samples have been stored with a protective grease layer and they have suffered the same spontaneous transformation. Then, according to the literature the mechanism to drive the phase transformation is stress. In this case, as no forces are applied, it is residual stress from the pseudoplastic deformation pits as explained in section 5.1.1.

As the phase transformation is driven by residual stress, other surface states were looked for as an attempt to emulate the surface state resulted from cavitation erosion. The surface were subjected to various mechanical processes in order to create such

residual stress state. These were: polishing with polycrystalline diamond suspension of 6 µm size; distribution of microindentations; and lapping. The idea of these experiments was to create a residual stress state that may drive a phase transformation with a similar delay as the one that occurs in cavitation erosion in order to understand the mechanism of the delay. Although these experiments have helped to understand the phase transformation delay, no delay is observed in other experiments apart to cavitation erosion. This is discussed below.

It is known that abrasive wear creates a region around the groove of plastic deformation due to the plowing mechanism, this region creates a residual stress state. In the work made by Deville et al. (2006) the ageing of a scratch from polishing on the zirconia surface is monitored at 140 °C, in steam at 3 bar. The stress related to the scratch accelerates the phase transformation. In the same way, the scratches created by polishing and by lapping are monitored but no transformation is detected when stored at room temperature (section 4.3.3 and section 4.3.5). Although it is probably that the stress created during the abrasive wear is high enough to induce transformation to monoclinic phase in the surroundings of the scratch, the residual stress state associated with this scratch is unable to transform further tetragonal zirconia into monoclinic. This is represented in Figure 5.9. Around the scratch, due to the plastic deformation, there are regions with compressive and tensile residual stresses. However, these residual stresses are unable to induce further transformation when stored at room temperature within the first months. It is also expected that due to the stresses during the abrasion, there is transformed zirconia in the surroundings of the scratch.
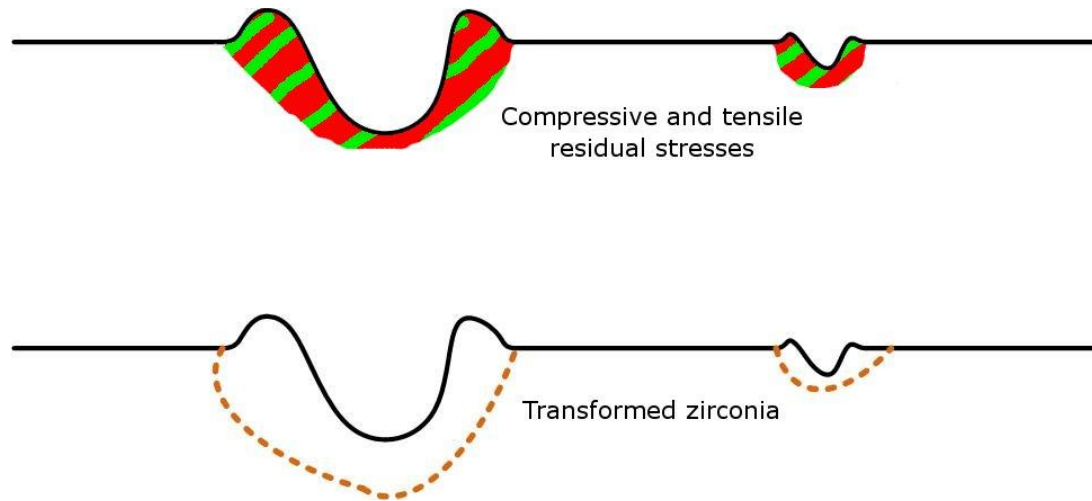
Figure 5.9. Explanation of the lack of further phase transformation in an abrasive scratch. The transformed zirconia is created during the abrasion.

A similar situation to the abrasion scratches happens within the indentation. It is known that the indentation produces plastic deformation around and that there is a residual stress state around the indentation due to the plastic deformation. During the indentation, it is expected that some tetragonal zirconia transforms into monoclinic due to the stress applied by the indenter. But the residual stress associated to the indentation is unable to induce further transformation when the sample is stored at room temperature (section 4.3.4). An explanation of this is shown in Figure 5.10, some transformed zirconia is expected to be created due to the stresses induced by the applied force of the indenter. The residual stresses that are created in the region of the indentation due to the plastic deformation are unable to induce further phase transformation.
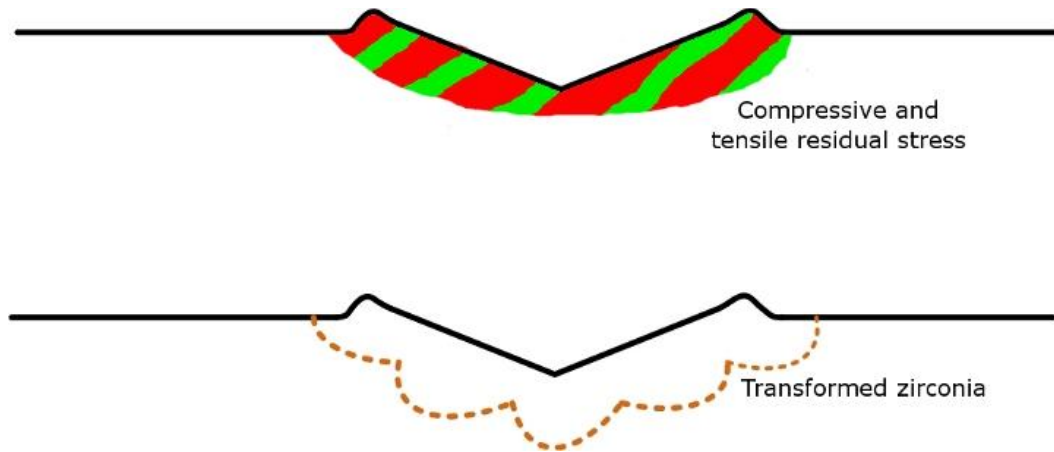
Figure 5.10. Explanation of the lack of further phase transformation in an indentation. The transformed zirconia is created during the indentation.

In the three experiments, polishing, lapping and indentation, the residual stress associated to the plastic deformation is located close to the mentioned characteristics. The regions between these characteristics do not develop any phase transformation, as the surface remains unchanged. For this reason, it is concluded that the residual stress created by these characteristics is not spread enough along the surface, and it is localized in the region where phase transformation has already been made by the applied forces rather than the residual stresses. Conversely, the residual stress state created by pseudoplastic cavitation pits is well spread all along the surface, the cavitation erosion creates a surface that has a slight plastic deformation and their associated residual stresses. The applied forces in the impact are not able to induce a complete phase transformation of the grains affected by the pseudoplastic deformation pits and the residual stress. Then, with the time, the residual stress spontaneously induces phase transformation in adjacent grains that remain as metastable tetragonal zirconia. The depth of the transformed zirconia is estimated in section 4.2 with a value of around 1.6 μm. This value is the same order of the expected grain size in zirconia "J".

Figure 5.11 shows a representation of this state, the surface is cracked and deformed. This plastic deformation of the grains creates a residual stress that is compressive or tensile depending on the direction and on the location. This residual stress is strong enough to spontaneously create phase transformation. As there is an increase of volume in the phase transformation from tetragonal to monoclinic, when a grain is

transformed to monoclinic, a new residual stress state is generated that may induce further phase transformation. There is a chain reaction effect.
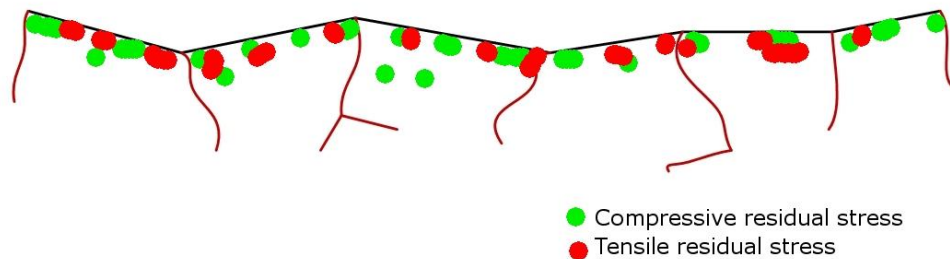
Figure 5.11. Explanation of the residual stress state in zirconia due to cavitation erosion.

Subcritical crack propagation is the behaviour where the cracks do not respond instantaneously to the applied stress. Conversely, in ceramics cracks may slowly grow under an applied stress well below of the stress needed to propagate a crack normally. This phenomenon is present either silicon nitride or PZT (Wachtman 1996). This characteristic may have some influence in the phase transformation delay of partially stabilized zirconia. It is possible that the subcritical crack propagation plays a role to change the residual stress state during the ageing process of the surface. However, it is clear that this role is secondary, and that the main reason for such a big topographic changes on the surface is the phase transformation of superficial grains. Evidence that support this affirmation is that, although silicon nitride suffers subcritical crack propagation, no sample of silicon nitride has shown any topographic change on the eroded surface when stored at room temperature. Consequently, the subcritical crack propagation is not the main mechanism for the topographic changes on the surface of zirconia.

The surface changes of the partially stabilized zirconia are progressive and they last around two months. They have been monitored with the different materials and this behaviour is present in all of them. There is a transformation rate that might be the subject of future investigations. Igawa et al. (1998) studied the phase transformation rate for metastable tetragonal zirconia powder at high temperature. The powder was composed by grains of different sizes and it was assumed that the whole grain transform instantly from tetragonal to monoclinic phase. In the present study, there

are several questions that are not answered. These questions are related to the way that transformation occurs. For example it is not clear if a whole grain of tetragonal zirconia transforms instantly in a whole grain of monoclinic, or there is a transition plane that is moving along the grain. This plane might move with the transformation of planes of atoms that change from tetragonal to monoclinic. Also, another factor that may influence transformation kinetic is the role of some kind of diffusion of atoms inside the lattice. How a crystal of tetragonal transform into monoclinic phase is something that is out of the scope of this research. However, it might explain the delay of the transformation. It is clear that the main cause to induce further transformation after the cavitation exposure has ended is the residual stress but it is unknown why this happens with a delay.

Finally, clear phase transformation delay is presented in zirconia "H", "I", "J", "K" and "M" (Figure 4.25 and Figure 4.26). Zirconia "H" and "K" are YTZP, that is partially stabilized tetragonal zirconia with yttria. Zirconia "I" is MgPSZ, that is a partially stabilized tetragonal zirconia with magnesia. The composition of zirconia "M" is unknown. The transformation of phase, apparently from the Figure 4.26, is less intense in zirconia "K" than in the others. Zirconia "K" has a higher percentage of yttria than the other YTZP, for this reason, the percentage of partially stabilized zirconia could be smaller and this could explain the less amount of transformation in its surface. When the proportion of oxide is higher than the amount necessary to achieve partially stabilized tetragonal zirconia, a cubic crystal structure that is stable appears, being called stabilized zirconia (Richerson 1982). It is concluded that the phase transformation delay is linked to the existent of partially stabilized tetragonal phase regardless of the oxide that is used to retain the tetragonal phase at low temperature.

5.3 Discussion about location of cavitation clusters

The published material about the use of analytical mechanics principles in fluid mechanics is scarce. However, the combination of both disciplines is possible. Fluid mechanics deal with a continuous of material that is considered to have a infinite

number of particles. Conversely, the classic theory of analytical mechanics deals with a limited number of solid particles that are defined by its location and orientation in the time.

In this research, Hamilton's principle is used to solve the value of the generalised coordinate that represents the location of the cavitation cluster. In other studies, Hamilton's principle is used to model the interaction of the fluid with a structure that can deform elastically (Lee and Park 2006; Qian et al. 2009; Unger et al.; Wadham-Gagnon et al. 2007). The kinetic energy with together the potencial energy of the fluid is added to the kinetic and elastic energy of the structure to get the Langrangian function that is used to apply Hamilton's principle. In this way, it is possible to couple the fluid and structural problem in only one equation.

In the problem of the location of cavitation cluster addressed here, no structural interaction is taken into account. There are also, studies using the Hamilton's principle to solve pure fluid mechanics problems but the approach followed by this studies is not related to the approach followed here. An example of this is the studied made by Gavrilyuk and Gouin (1999) where a new form of governing equations in fluid mechanics is worked out from Hamilton's principle. Gavrilyuk and Saurel (2002) uses the Hamilton's principle to couple the interaction between the two phases of a bubbly liquid and solves the equations to model wave propagation. Again, the approach followed is very different to the approach followed here.

In the article published by Oskouei and Dumanoglu (2001), Hamilton's principle is used to formulate the equations in the elements of the finite element method of a concrete dam and the water of the reservoir taking into account the energy derived from strain, kinetic and free surface potential. Although the article discusses cavitation on the wall of the dam during an earthquake, cavitation is not modelled by Hamilton's principle. Conversely, cavitation is assumed to happen in the regions where the pressure is negative according to the finite element analysis.

On the other hand, in relation to the findings of this research, it is seen that the erosion pattern correspond in location with the cavitation clusters. This is believed to

happen because the huge bubbles that coalesce in the cavitation cluster reduce the size of the boundary layer and pushes the collapsing bubbles close to the surface. For this reason the studied of the cavitation erosion patterns is useful to study the cavitation cluster location.

The use of Hamilton's principle to define the location of cavitation clusters is an original and strong contribution of this research. To the best of author's knowledge, no analytical mechanics principles has been used to solve cavitation clusters related problems previously. The approach followed here is to assume the existence of the cavitation cluster at a position determined by the generalised coordinate. Then, the Navier-Stokes equations are used to calculate the movement of the liquid according to conservation of mass and momentum. Hamilton's principle gives the values of the generalised coordinate that is solution of the problem and these values are compared with those experimental. As the trends and values of the generalised coordinate are similar to the experimental ones, it is concluded that the location of cavitation clusters fulfil a condition of least action where the existence of cavitation clusters alleviates the demand of energy from the system. Otherwise, the system would need a higher amount of energy to follow the movement of the ultrasonic horn than in the configuration that is solution. In other words, if the location of cavitation clusters changes, the amount of energy that the system requires increases and the system tends to return to the previous location of cavitation clusters.

This approach may be used in other configuration different to the 5 mm diameter horn. This is a promising research line that may explain the rather repetitive patterns of cavitation clusters in ultrasonic cavitation in the future. It is also a research line that may influence the fundamental theory of cavitation. There is also a possibility of developing governing equations for cavitation taking into account the surface energy and using Hamilton's principle. In such case, it would be expected that patterns as the one presented in Figure 5.12 would be fully explained.

Figure 5.12. Repetitive pattern of cavitation erosion in an ultrasonic horn of 20 mm diameter.

Chapter 6   Conclusions

6.1 Contributions to knowledge

A study of the mechanism of cavitation erosion in ceramics has been carried out. A detailed analysis of the cavitation clusters location in the experimental conditions has been presented from the point of view of fluid mechanics. The outcome of this research has been three important contributions to knowledge that are the following:

1. When polished technical ceramics are subjected to cavitation erosion, a pseudoplastic deformation pit appears during the early stages of erosion.

2. Partially stabilized zirconia presents a delay in the transformation of phase, stored at room conditions, of several weeks, after cavitation exposure that produces a surface topography change.

3. The location of cavitation clusters has been explained with the use of analytical mechanics; a condition of minimum energy is fulfilled. When the location of cavitation clusters is moved, the energy required for the system is higher and tends to return to its original location. The principle of least action is fulfilled.

Apart of the three contributions to knowledge presented above, there are other contributions in this research that are important and are summarized in the following section.

6.2 Other conclusions

An explanation of the pseudoplastic deformation pit has been developed as the best explanation consistent with the established knowledge and with the experimental results. The pseudoplastic deformation pits are produced due to the release of slip planes by cracks in the intergranular phase that allow plastic deformation. This is

supported by the evidence that the pits are smaller in zirconia than in silicon nitride although the hardness of zirconia is lower than the hardness of silicon nitride, and it is consistent with the strength of zirconia being higher than the strength of silicon nitride. Also this is supported by the fact that the number of pits is smaller in zirconia than in silicon nitride.

Other observations are:

1. Typical sizes of these pseudoplastic deformation pits are $0.6\mu m^3$ for zirconia and $2\mu m^3$ for silicon nitride.

2. The partially stabilized zirconia presents the transformation delay regardless of the oxide that is used to stabilize it, yttria, magnesia or others.

3. This transformation delay is driven by residual stresses, water is not important.

4. The cavitation with a 5mm diameter horn presents a ring shape cluster that produces an inwards and outwards movement of the liquid at the same time.

5. This ring-shape exists because it produces a situation of minimum energy and it changes its size to fulfil this. The acoustic approach is unsuitable for solving this because the speed of sound changes enormously with the presence of bubbles.

6.2.1 *Other methodology innovations.*

In the course of this research, some innovations in methodology have been employed and are summarised here:

1.   The "stationary specimen method" with small diameter horn has been studied, and used for the early stages of cavitation erosion. This method allows a light and controlled cavitation exposure that allows monitoring the initial erosion.

2.   A methodology to process the image in order to identify small changes on the surface has been developed and presented as a "movie" of the erosion.

3.   An experimental process to measure the track of a silicon nitride ball even when it is not visible has been used.

4.   A fluid dynamics model of this configuration has been proposed and it agrees with the experimental data. This model suggests that this method is not suitable for material loss rate due to the inwards / outwards movement of the liquid.

5.   A method to classify cavitation resistance has been developed as surface loss, instead of material loss. This method processes the image until the pixels are black or white.

6.3 Future work

The future work that comes out naturally from this research is in three different fields. These are the cavitation erosion of ceramics, the manufacturing process of ceramics and fluid mechanics.

Future work in the cavitation erosion of ceramics consists of the demonstration of the explanation for pseudoplastic deformation pits. This explanation is supported here by some experimental evidence, but this evidence is not fully conclusive. A strategy to fully demonstrate that the pseudoplastic deformation pits are always linked to the appearance of cracks is to etch the surface, in order to highlight the cracks and take good quality SEM images. The cracks should appear only in the regions where pseudoplastic deformation pits are visible with optical microscope.

A very interesting future work from the industrial point of view could be the understanding of the reasons why silicon nitride "A" has much better performance than the other silicon nitrides and it is much easier to polish. The combination of these two characteristics makes it a very interesting material for industry. Its performance is better and it is cheaper to manufacture (at least in the last stages of manufacturing processes). Also, the fact that it is easier to polish makes it interesting for applications where a shape that is not a ball must be used. It is believed that the

differences between silicon nitride "A" and the others come from the sintering powder, additives, and sintering process.

Future work in fundamental theory of acoustic cavitation from the point of view of fluid mechanics could be the utilisation of the new approach to explain the location of cavitation clusters in different configurations. This may lead to a complete explanation of the consistently reproducible damage patterns that usually are obtained in ultrasonic cavitation. Also, it might be possible taking into account the surface energy to define the Lagrangian as a function of several variables including the size of cavitation clusters and the distance between them in a way that a governing equation for cavitation clusters might be developed.

References

Adachi, K., Kato, K., and Chen, N., 1997. Wear map of ceramics. *Wear,* 203-204, 291-301.

Archard, J. F., 1953. Contact and rubbing of flat surfaces. *Journal of Applied Physics,* 24 (8), 981-988.

Asada, S., Fukuda, K., and Ueki, M., 1997. Surface damage of engineering ceramics in rolling contact. *Journal of the ceramic society of Japan,* 105 (3), 238-240.

Ashby, M. F., 1999. *Materials selection in mechanical design.* 2nd ed. Oxford: Butterworth-Heinemann.

Astm. 2003. Standard test method for cavitation erosion using vibratory apparatus, *G32-03*: ASTM.

Baumgartner, H. R., Sundberg, D. V., and Wheildon, W. M., 1973. Silicon nitride in rolling contact bearings. Final report jan. 3, 1973 - oct. 3, 1973.

Baumgartner, H. R., and Whieldon, W. M., 1973. Rolling contact fatigue of hot-pressed silicon nitride versus surface preparation techniques. *Surfaces and Interfaces of Glass and Ceramics*, 179-193.

Bhargava, V., Hahn, G. T., and Rubin, C. A., 1985a. An elastic-plastic finite element model of rolling contact, part 1: Analysis of single contacts. *Journal of applied mechanics,* 52 (1), 67-74.

Bhargava, V., Hahn, G. T., and Rubin, C. A., 1985b. An elastic-plastic finite element model of rolling contact, part 2: Analysis of repeated contacts. *Journal of applied mechanics,* 52 (1), 75-82.

Bhushan, B., 2002. *Introduction to tribology.* New York ; Chichester: Wiley.

Blau, P. J., 2005. On the nature of running-in. *Tribology International,* 38 (11-12), 1007-1012.

Campos-Pozuelo, C., Granger, C., Vanhille, C., Moussatov, A., and Dubus, B., 2005. Experimental and theoretical investigation of the mean acoustic pressure in the cavitation field. *Ultrasonics Sonochemistry,* 12 (1-2), 79-84.

Celotta, D. W., Qureshi, U. A., Stepanov, E. V., Goulet, D. P., Hunter, J., Buckberry, C. H., Hill, R., Sherikar, S. V., Moshrefi-Torbati, M., and Wood, R. J. K., 2007. Sand erosion testing of novel compositions of hard ceramics. *Wear,* 263 (1-6), 278-283.

Chao, L. Y., Lakshminarayanan, R., Iyer, N., Lin, G. Y., and Shetty, D. K., 1998. Transient wear of silicon nitride in lubricated rolling contact. *Wear,* 223 (1-2), 58-65.

Choi, H.-J., Han, D.-H., Park, D.-S., Kim, H.-D., Han, B.-D., Lim, D.-S., and Kim, I.-S., 2003. Erosion characteristics of silicon nitride ceramics. *Ceramics International,* 29 (6), 713-719.

Coleman, A. J., Saunders, J. E., Crum, L. A., and Dyson, M., 1987. Acoustic cavitation generated by an extracorporeal shockwave lithotripter. *Ultrasound in Medicine & Biology,* 13 (2), 69-76.

D'errico, G. E., Bugliosi, S., and Cuppini, D., 1997. Performance of ceramics in erosion tests by solid particle impingement. *Journal of Materials Processing Technology,* 64 (1-3), 85-92.

D'errico, G. E., Bugliosi, S., and Cuppini, D., 2001. Erosion of ceramics and cermets. *Journal of Materials Processing Technology,* 118 (1-3), 448-453.

Denry, I. L., and Holloway, J. A., 2006. Microstructural and crystallographic surface changes after grinding zirconiaa(euro)• based dental ceramics. *Journal of Biomedical Materials Research,* 76 (2), 440-448.

Deville, S., Chevalier, J., and Gremillard, L., 2006. Influence of surface finish and residual stresses on the ageing sensitivity of biomedical grade zirconia. *Biomaterials,* 27 (10), 2186-2192.

Dowson, D., 1998. *History of tribology.* 2nd ed. London: Professional Engineering Publishing.

Drum, W., 1939. *Dental ceramics manual.* Berlin Publishing House.

Eigenmann, B., and Macherauch, E., 1995. Determination of inhomogeneous residual stress states in surface layers of machined engineering ceramics by synchrotron x-rays. *Nuclear Instruments and Methods in Physics Research Section B: Beam Interactions with Materials and Atoms,* 97 (1-4), 92-97.

Fang, Q., Sidky, P. S., and Hocking, M. G., 1997. The effect of corrosion and erosion on ceramic materials. *Corrosion Science,* 39 (3), 511-527.

Fang, Q., Sidky, P. S., and Hocking, M. G., 1999a. Erosion and corrosion of psz-zirconia and the t-m phase transformation. *Wear,* 233-235, 615-622.

Fang, Q., Xu, H., Sidky, P. S., and Hocking, M. G., 1999b. Erosion of ceramic materials by a sand/water slurry jet. *Wear,* 224 (2), 183-193.

Fett, T., Kounga Njiwa, A. B., and Rödel, J., 2005. Crack opening displacements of vickers indentation cracks. *Engineering Fracture Mechanics,* 72 (5), 647-659.

Fujikawa, S., and Akamatsu, T. 1980. Effects of the non-equilibrium condensation of vapour on the pressure wave produced by the collapse of a bubble in a liquid. (Vol. 97, pp. pp 481-512). Journal of Fluid Mechanics.

Gavrilyuk, S., and Gouin, H., 1999. A new form of governing equations of fluids arising from hamilton's principle. *International Journal of Engineering Science,* 37 (12), 1495-1520.

Gavrilyuk, S., and Saurel, R., 2002. Mathematical and numerical modeling of two-phase compressible flows with micro-inertia. *Journal of Computational Physics,* 175 (1), 326-360.

Gogate, P. R., and Pandit, A. B., 2004. Sonochemical reactors: Scale up aspects. *Ultrasonics Sonochemistry,* 11 (3-4), 105-117.

Green, D. J., 1998. *An introduction to the mechanical properties of ceramics.* Cambridge: Cambridge University Press.

Grun, R., 1979. The crystal structure of [beta]-si3n4: Structural and stability considerations between [alpha]- and [beta]-si3n4. *Acta Crystallographica Section B,* 35 (4), 800-804.

Hadfield, M., 1995. Observations of lubricated rolling contact fatigue on silicon nitride rods. *Ceramics international,* 21 (1), 13-19.

Hadfield, M., 1998. Failure of silicon nitride rolling elements with ring crack defects. *Ceramics international,* 24 (5), 379-386.

Hadfield, M., and Stolarski, T. A., 1995. Observations of delamination fatigue on pre-cracked ceramic elements in rolling contact. *Ceramics international,* 21 (2), 125-130.

Hahn, G. T., Bhargava, V., Rubin, C. A., Chen, Q., and Kim, K., 1987. Analysis of the rolling contact residual stresses and cyclic plastic deformation of sae 52100 steel ball bearings. *Journal of tribology,* 109 (4), 618-626.

Hamrock, B. J., and Dowson, D., 1981. *Ball bearing lubrication, the elastohydrodynamics of elliptical contacts,.* John Wiley & Sons.

Haosheng, C., Jiang, L., Darong, C., and Jiadao, W., 2008. Damages on steel surface at the incubation stage of the vibration cavitation erosion in water. *Wear,* 265 (5-6), 692-698.

Hattori, S., Ogiso, T., Minami, Y., and Yamada, I., 2008. Formation and progression of cavitation erosion surface for long exposure. *Wear,* 265 (11-12), 1619-1625.

Hearle, A. D., and Johnson, K. L., 1987. Cumulative plastic flow in rolling and sliding line contact. *Journal of applied mechanics,* 54 (1), 1-7.

Hertz, H. 1881. Uber die berunhrung fester elasticher korper, (on the contact of elastic solids) (Vol. 92, pp. 156-171). J. Reine und Angewandte Mathematik.

Ho, C.-J., Liu, H.-C., and Tuan, W.-H., 2009. Effect of abrasive grinding on the strength of y-tzp. *Journal of the European Ceramic Society,* 29 (12), 2665-2669.

Igawa, N., Nagasaki, T., Ishii, Y., Noda, K., Ohno, H., Morii, Y., and Fernandez-Baca, J. A., 1998. Phase-transformation study of metastable tetragonal zirconia powder. *Journal of Materials Science,* 33 (19), 4747-4758.

Johnson, K. L., 1985. *Contact mechanics.* Cambridge: CUP.

Kang, J., and Hadfield, M., 2001a. A novel eccentric lapping machine for finishing advanced ceramic balls. *Proceedings of the Institution of Mechanical Engineers. Part B, Journal of Engineering Manufacture,* 215 (6), 781-795.

Kang, J., and Hadfield, M., 2001b. Parameter optimization by taguchi methods for finishing advanced ceramic balls using a novel eccentric lapping machine. *Proceedings of the Institution of Mechanical Engineers. Part B, Journal of Engineering Manufacture,* 215 (1), 69-78.

Kang, J., and Hadfield, M., 2003. Comparison of four-ball and five-ball rolling contact fatigue tests on lubricated si3n4/steel contact. *Materials & Design,* 24 (8), 595-604.

Kang, J., and Hadfield, M., 2005. Examination of the material removal mechanisms during the lapping process of advanced ceramic rolling elements. *Wear,* 258 (1-4), 2-12.

Karimi, A., and Avellan, F., 1986. Comparison of erosion mechanisms in different types of cavitation. *Wear,* 113, 305-322.

Karunamurthy, B., Hadfield, M., Vieillard, C., and Morales, G., 2010a. Cavitation erosion in silicon nitride: Experimental investigations on the mechanism of material degradation. *Tribology International,* 43 (12), 2251-2257.

Karunamurthy, B., Hadfield, M., Vieillard, C., Morales-Espejel, G. E., and Khan, Z., 2010b. Cavitation and rolling wear in silicon nitride. *Ceramics International,* 36 (4), 1373-1381.

Kato, K., and Adachi, K., 2002. Wear of advanced ceramics. *Wear,* 253 (11-12), 1097-1104.

Khan, A. S., and Huang, S., 1995. *Continuum theory of plasticity.* New York ; Chichester: John Wiley & Sons.

Kosmac, T., Oblak, C., Jevnikar, P., Funduk, N., and Marion, L., 1999. The effect of surface grinding and sandblasting on flexural strength and reliability of y-tzp zirconia ceramic. *Dental Materials,* 15 (6), 426-433.

Lathabai, S., 2000. The effect of grain size on the slurry erosive wear of ce-tzp ceramics. *Scripta Materialia,* 43 (5), 465-470.

Lee, S. K., and Lawn, B. R., 1998. Role of microstructure in hertzian contact damage in silicon nitride: Ii, strength degradation. *Journal of the American Ceramic Society,* 81 (4), 997-1003.

Lee, S. K., Wuttiphan, S., and Lawn, B. R., 1997. Role of microstructure in hertzian contact damage in silicon nitride: I, mechanical characterization. *Journal of the American Ceramic Society,* 80 (9), 2367-2381.

Lee, U., and Park, J., 2006. Spectral element modelling and analysis of a pipeline conveying internal unsteady fluid. *Journal of Fluids and Structures,* 22 (2), 273-292.

Lee, W. E., and Rainforth, W. M., 1994. *Ceramic microstructures : Property control by processing.* London: Chapman & Hall.

Li, J., Zhang, L., Shen, Q., and Hashida, T., 2001. Degradation of yttria stabilized zirconia at 370 k under a low applied stress. *Materials Science and Engineering: A,* 297 (1), 26-30.

Litzow, U., Gahr, K.-H. Z., and Schneider, J., 2006. Cavitation erosion of advanced ceramics in water. *International Journal of Materials Research: Zeitschrift fuer Metallkunde,* 97 (10), 1372-1377.

Liñán Martínez, A., 1967. *Mecánica de fluidos (primera parte).* Madrid: Publicaciones de la Escuela Técnica Superior de Ingenieros Aeronáuticos.

Lu, J., Zum Gahr, K.-H., and Schneider, J., 2008. Microstructural effects on the resistance to cavitation erosion of zro2 ceramics in water. *Wear,* 265 (11-12), 1680-1686.

Lyng, S., Sudmann, E., Hulbert, S. F., and Sauer, B. W., 1973. Fixation of permanent orthopaedic prosthesis: Use of ceramics in the tibial plateau. *Acta orthopaedica Scandinavica,* 44 (6), 694-701.

Merwin, J. E., and K.L., J., 1963. An analysis of plastic deformation in rolling contact. *Proceedings of the Institution of Mechanical Engineers, 177*.

Milhet, X., Demenet, J. L., and Rabier, J., 2000. Intragranular plasticity of î² si3n4 between 20 â°c and 700 â°c. *Journal de physique. IV, Proceedings,* 10 (6), Pr6-165-Pr166-169.

Milhet, X., Demenet, J. L., and Rabier, J., 2003. The role of dislocations in the plastic behavior of silicon nitride a review. *Defect and Diffusion Forum,* 218 (1), 23-37.

Mohajerani, A., and Spelt, J. K., 2009. Edge rounding of brittle materials by low velocity erosive wear. *Wear,* 267 (9-10), 1625-1633.

Moussatov, A., Granger, C., and Dubus, B., 2003. Cone-like bubble formation in ultrasonic cavitation field. *Ultrasonics Sonochemistry,* 10 (4-5), 191-195.

Moussatov, A., Granger, C., and Dubus, B., 2005. Ultrasonic cavitation in thin liquid layers. *Ultrasonics sonochemistry,* 12 (6), 415-422.

Niebuhr, D., 2007. Cavitation erosion behavior of ceramics in aqueous solutions. *Wear,* 263 (1-6), 295-300.

Oka, Y. I., Mihara, S., and Yoshida, T., 2009. Impact-angle dependence and estimation of erosion damage to ceramic materials caused by solid particle impact. *Wear,* 267 (1-4), 129-135.

Oka, Y. I., and Miyata, H., 2009. Erosion behaviour of ceramic bulk and coating materials caused by water droplet impingement. *Wear,* 267 (11), 1804-1810.

Papanagiotou, H. P., Morgano, S. M., Giordano, R. A., and Pober, R., 2006. In vitro evaluation of low-temperature aging effects and finishing procedures on the flexural strength and structural stability of y-tzp dental ceramics. *The Journal of Prosthetic Dentistry,* 96 (3), 154-164.

Plesset, M. S., and Chapman, R. B., 1971. Collapse of an initially spherical vapour cavity in the neighbourhood of a solid boundary. *Journal of Fluid Mechanics,* 47 (02), 283-290.

Ponter, A. R. S., Hearle, A. D., and Johnson, K. L., 1985. Application of the kinematical shakedown theorem to rolling and sliding point contacts. *Journal of the mechanics and physics of solids,* 33 (4), 339-362.

Popp, M., and Sternagel, R., 1999. *Hybrid ceramic and all ceramic anti friction bearings.* Paper presented at the Proceedings of the 8th Europena Space Mechanisms and Tribology Symposium, Tolouse.

Prieto Alberca, M., 1994. *Curso de mecánica racional – dinámica.* Madrid: ADI Madrid.

Qian, Q., Wang, L., and Ni, Q., 2009. Instability of simply supported pipes conveying fluid under thermal loads. *Mechanics Research Communications,* 36 (3), 413-417.

Ren, C. Z., Wang, T. Y., Jin, X. M., and Xu, H., 2002. Experimental research on the residual stress in the surface of silicon nitride ceramic balls. *Journal of Materials Processing Technology,* 129 (1-3), 446-450.

Richerson, D. W., 1982. *Modern ceramic engineering : Properties, processing and use in design.* New York: Dekker.

Sanders, J. H., Cutler, J. N., Miller, J. A., and Zabinski, J. S., 1999. In vacuuo tribological investigations of metal, ceramic and hybrid interfaces for high-speed spacecraft bearing applications. *Tribology International,* 32 (11), 649-659.

Scott, D., and Blackwell, J., 1973. Hot pressed silicon nitride as a rolling bearing material. A preliminary assessment. *Wear,* 24 (1), 61.

Scott, D., Blackwell, J., and Mccullagh, P. J., 1971. Silicon nitride as a rolling bearing material. A preliminary assessment. *Wear,* 17 (1), 73-82.

Silberman, E., 1957. Sound velocity and attenuation in bubbly mixtures measured in standing wave tubes. *Journal of the Acoustical Society of America,* 29 (8), 925-933.

Stachowiak, G. W., and Batchelor, A. W., 2001. *Engineering tribology.* 2nd ed. Boston, Mass. ; Oxford: Butterworth-Heinemann.

Suematsu, H., Petrovic, J. J., and Mitchell, T. E., 1996. Plastic deformation of silicon nitride single crystals. *Materials Science and Engineering: A,* 209 (1-2), 97-102.

Timoshenko, S. P., and Goodier, J. N., 1982. *Theory of elasticity.* 3rd ed. Auckland ; London: McGraw-Hill.

Tomlinson, W. J., Kalitsounakis, N., and Vekinis, G., 1999. Cavitation erosion of aluminas. *Ceramics International,* 25 (4), 331-338.

Tomlinson, W. J., and Matthews, S. J., 1994. Cavitation erosion of structural ceramics. *Ceramics International,* 20 (3), 201-209.

Tu, J. P., and Li, J., 1997. Effect of phase transformation induced plasticity on the erosion of tzp ceramics. *Materials Letters,* 31 (3-6), 267-270.

Unger, R., Haupt, M. C., and Horst, P., Application of lagrange multipliers for coupled problems in fluid and structural interactions. *Computers & Structures,* 85 (11-14), 796-809.

Vatani Oskouei, A., and Dumanoglu, A. A., 2001. Nonlinear dynamic response of concrete gravity dams: Cavitation effect. *Soil Dynamics and Earthquake Engineering,* 21 (2), 99-112.

Wachtman, J. B., 1996. *Mechanical properties of ceramics.* New York ; Chichester: Wiley.

Wada, S., and Yokoyama, K., 1999. Differences in the tetragonal to monoclinic phase transformation rate in hot water of 3 mol% y_2o_3-zro_2 ceramics under different surface conditions. *Journal of Ceramic Society of Japan,* 107, 92-95.

Wadham-Gagnon, M., Pai¨Doussis, M. P., and Semler, C., 2007. Dynamics of cantilevered pipes conveying fluid. Part 1: Nonlinear equations of three-dimensional motion. *Journal of Fluids and Structures,* 23 (4), 545-567.

Wang, D. F., and Mao, Z. Y., 1996. A study for erosion of si3n4 ceramics by impact of solid particles. *Wear,* 199 (2), 283-286.

Wang, Y., and Hadfield, M., 1999. Rolling contact fatigue failure modes of lubricated silicon nitride in relation to ring crack defects. *Wear,* 225 (2), 1284-1292.

Wang, Y., and Hadfield, M., 2000a. The influence of ring crack location on the rolling contact fatigue failure of lubricated silicon nitride: Experimental studies. *Wear,* 243 (1), 157-166.

Wang, Y., and Hadfield, M., 2000b. The influence of ring crack location on the rolling contact fatigue failure of lubricated silicon nitride: Fracture mechanics analysis. *Wear,* 243 (1), 167-174.

Wang, Y., and Hadfield, M., 2001. Ring crack propagation in silicon nitride under rolling contact. *Wear,* 250 (1-12), 282-292.

Wang, Y., and Hadfield, M., 2004. Failure modes of ceramic rolling elements with surface crack defects. *Wear,* 256 (1-2), 208-219.

Wheildon, W. M., Baumgartner, H. R., Sundberg, D. V., and Torti, M. L., 1973. Ceramic materials in rolling contact bearings. Final report january 3, 1972 - february 3, 1973. FEBRUARY-3.

Wijngaar, L. V., 1972. One-dimensional flow of liquids containing small gas bubbles. *Annual Review of Fluid Mechanics,* 4, 369-396.

Williams, J. A., 1994. *Engineering tribology.* Oxford: Oxford University Press.

Wood, A. B., 1941. *A text book of sound.* London: G. Bell and Sons Ltd.

Xu, J., Kato, K., and Hirayama, T., 1997. The transition of wear mode during the running-in process of silicon nitride sliding in water. *Wear,* 205 (1-2), 55-63.

Young, F. R., 1999. *Cavitation.* London: Imperial College Press.

Zaretsky, E. V., 1990. *Bearing elastohydrodynamic lubrication: A complex calculation made simple.* (E-5360). Cleveland: NASA Lewis Research Center.

Zhao, P., Hadfield, M., Wang, Y., and Vieillard, C., 2006a. Subsurface propagation of partial ring cracks under rolling contact: Part i. Experimental studies. *Wear,* 261 (3-4), 382-389.

Zhao, P., Hadfield, M., Wang, Y., and Vieillard, C., 2006b. Subsurface propagation of partial ring cracks under rolling contact: Part ii. Fracture mechanics analysis. *Wear,* 261 (3-4), 390-397.

Appendices

Appendix A. Micrographs of the early stages of cavitation erosion on ceramics.

Here, a selection of micrographs showing the cavitation erosion process in polished ceramics is presented. The black arrows in the micrographs identify the new pseudoplastic deformation pits produced on the surface since the previous micrograph. In the case of alumina, the arrows indicate a local change of tilt due to cracks. The graphic scale is provided. It is easy to identify the damage on silicon nitride. The damage on alumina is not easy to identify, since there is not visible plastic deformation but it shows a clear loss of material after 20 minutes of cavitation erosion. The pseudoplastic deformation pits on zirconia are smaller than in silicon nitride and they are more difficult to be seen.

Cavitation erosion of silicon nitride "A". Time of exposure indicated.
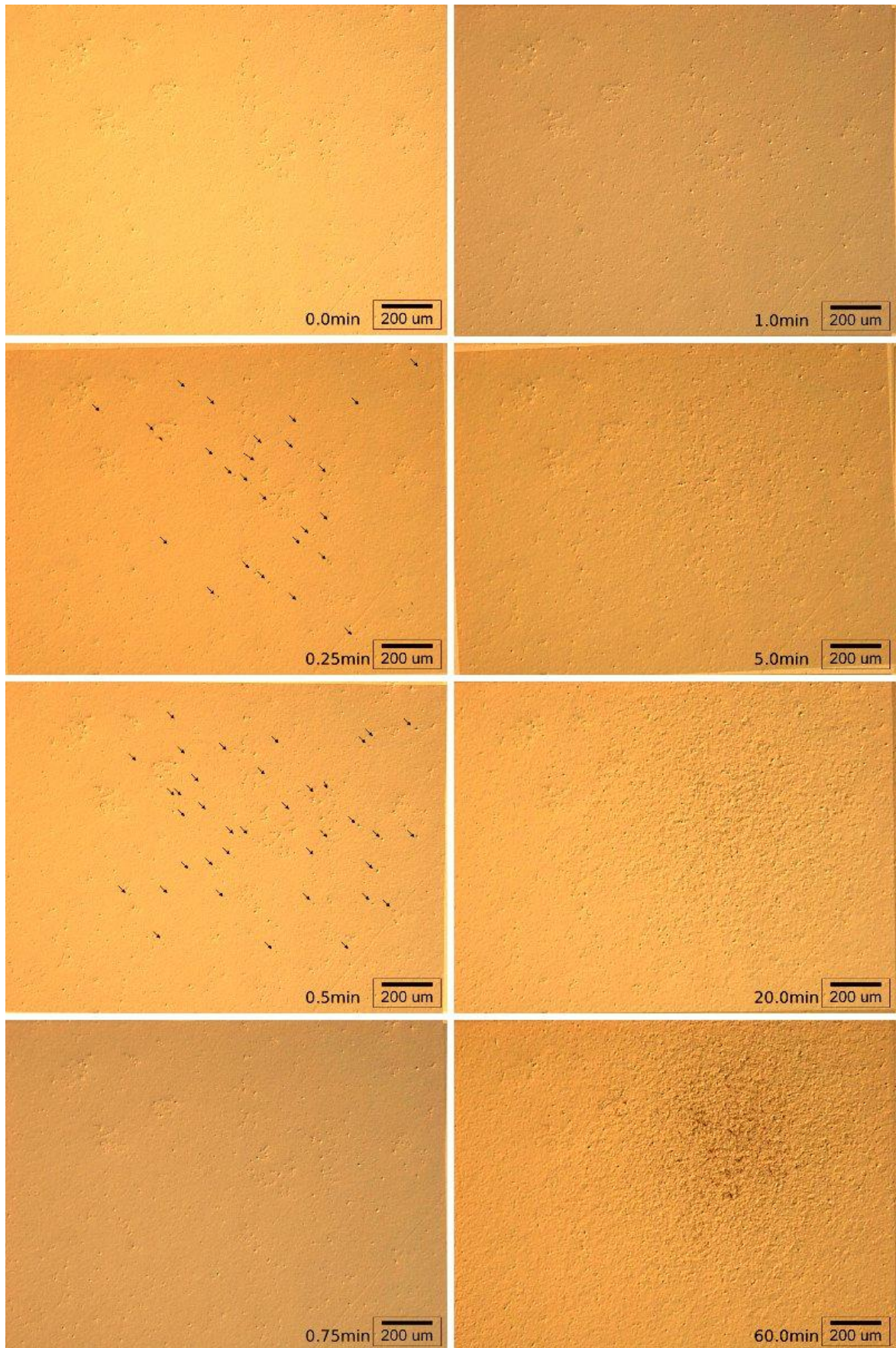
Cavitation erosion of silicon nitride "D". Time of exposure indicated.
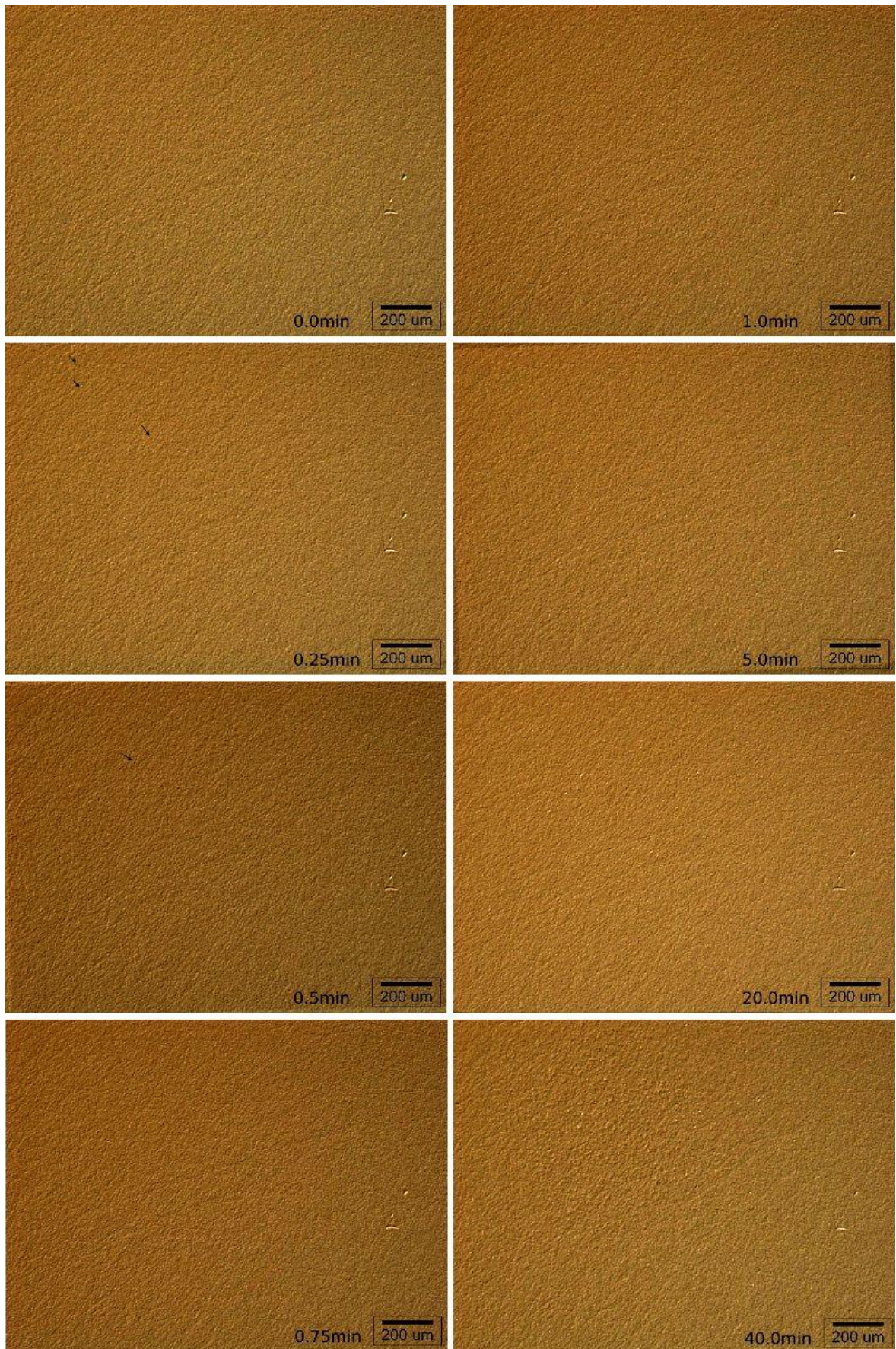
Cavitation erosion of zirconia "H". Time of exposure indicated.
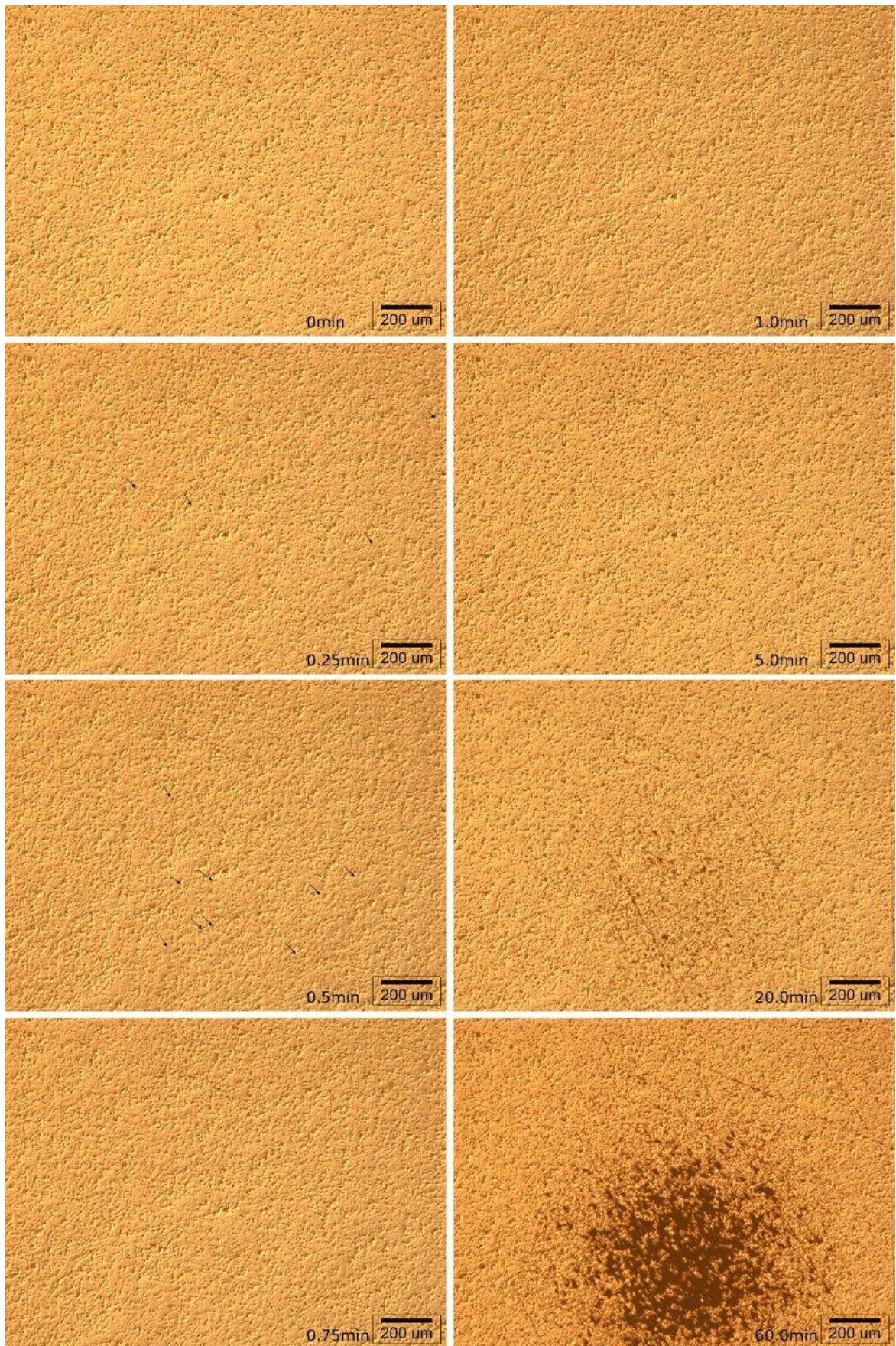
Cavitation erosion of alumina "N". Time of exposure indicated.

Appendix B. Procedure to obtain the equations for the cavitation cluster model.

As an example, the works out of the equations from section 3.1.5 are presented.

Firstly, the liquid region between the central region and the ring region is modelled. This region is called "1" in Figure 3.6. The volume of liquid is constant and the bubbly region absorbs the change of volume. The volume of liquid is calculated when the distance between the sample and the horn is minimal, then the volume of the bubbly region is zero.

$$V_{L1} = \pi \left(R_{C1}{}^2 - R_{R1}{}^2 \right)(h(t)) = \pi \cdot R_R{}^2 (h_0 - \frac{a}{2})$$

<div align="right">Equation 6.1</div>

where V_{L1} is the volume of the liquid in region "1" and $h(t)$ is the distance between horn and sample that follows the following equation:
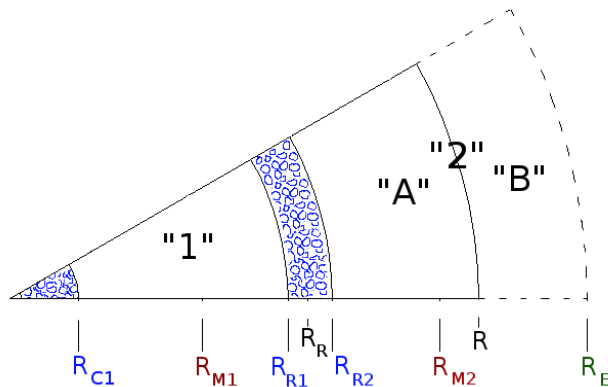
$$h(t) = h_0 + \frac{a}{2}\sin(2\pi f t)$$

<div align="right">Equation 3.3</div>

Figure 3.6. Sector showing the two liquid regions analysed.

This region between the central region and the ring region has not any radial force resultant due to it being surrounded by two bubbly regions. The momentum along the radial direction for this region should be zero. With this simplification it is possible

to calculate the fluid velocity in this region. As there is cylindrical symmetry only a sector of the disk is used (Figure 3.6). The velocity is given as a function of the time and the radius using Navier-Stokes in integral and cylindrical form for the conservation of mass and for the radial momentum (Liñán Martínez 1967).

The fluid velocity at R_{M1} is zero since it is the radius where the movement of the liquid changes direction, for radius bigger than R_{M1} the movement is outwards when the horn is going down and for radius smaller than R_{M1} the movement is inwards when the horn is going down. Then, the velocity at R_{M1} is zero. With conservation of mass, it is possible to calculate the velocity of the liquid in the control volume defined between R_{M1} and r, where r is between R_{M1} and R_{R1}.

$$\int_{\partial\Omega_{R_{M1-r}}} \rho\vec{v}(r,t)\cdot\vec{n}d\partial\Omega = -\frac{d}{dt}\int_{\Omega_{R_{M1-r}}} \rho d\Omega \qquad \text{Equation 6.2}$$

where $\Omega_{R_{M1-r}}$ is the control volume and $\partial\Omega_{R_{M1-r}}$ is the control surface. The control surface is delimited by the cylinder of radius R_{M1} where the fluid velocity is zero, the surface of the horn and the sample and the cylinder of radius r. The velocity, in this model, is parallel to the surface of the horn and sample. Hence the dot product of the velocity with the normal vector is zero for these surfaces. Working out the Equation 6.2 gives:

$$v(r,t) = \frac{-\frac{d}{dt}\int_{\Omega_{R_{M1-r}}} d\Omega}{\partial\Omega_r} = \frac{-\frac{d\Omega_{R_{M1-r}}}{dt}}{\partial\Omega_r} = \frac{-\pi(r^2 - R_{M1}^2)h'}{2\pi rh} = \frac{(R_{M1}^2 - r^2)h'}{2rh} \qquad \text{Equation 6.3}$$

The previous work out is also valid when r is between R_{C1} and R_{M1}, and the control volume between r and R_{M1}. In this new control volume the result is the same as Equation 6.3. The last expression of Equation 6.3 is Equation 3.4 that shows the fluid velocity for region "1":

$$v(r,t) = \frac{(R_{M1}^2 - r^2)h'}{2rh} \qquad \text{Equation 3.4}$$

In Equation 3.4, the value of R_{M1} is still unknown, to obtain the value the momentum equations are used. The velocity is in the radial direction. Then, the momentum equation along z and ϕ are not used. The forces applied to the system are vertical, due to the movement of the horn. Consequently, there is no change of momentum along the radial direction. The momentum equation is

$$\frac{d}{dt}\int_{\Omega}\rho\vec{v}d\Omega+\int_{\partial\Omega}\rho\vec{v}\vec{v}\cdot\vec{n}d\partial\Omega=\int_{\partial\Omega}\tau\cdot\vec{n}d\partial\Omega+\int_{\Omega}\rho\vec{f}d\Omega \qquad \text{Equation 6.4}$$

where there is no mass entering or leaving the control volume. Then, the second term is zero. There is no forces doing work in a radial direction. Then the third and the forth term are zero. Equation 6.4 transforms into Equation 6.5. This last equation means that the derivative of the momentum with respect to the time is zero. The consequence of this is that the momentum is constant and equal to zero since there is a time where the velocity of the system is zero, that is when h' is zero at times equal to $t=(1+2n)/(4f)$, where n is a natural number.

$$\frac{d}{dt}\int_{\Omega}\rho\vec{v}d\Omega=0 \qquad \text{Equation 6.5}$$

Then, the momentum equation in this system for region "1" at a time very close to $t=(1+2n)/(4f)$ is:

$$\int_{\Omega}\vec{v}d\Omega=\int_{0}^{R_R}\frac{(R_{M1}{}^2-r^2)h'}{2rh}rdr=0\Rightarrow 0=R_{M1}{}^2R_R-\frac{R_R{}^3}{3} \qquad \text{Equation 6.6}$$

where it is possible to obtain R_{M1} in the same form as Equation 3.5.

$$R_{M1}=\frac{R_R}{\sqrt{3}} \qquad \text{Equation 3.5}$$

For the calculus of the energy, the velocity given by Equation 3.4 is valid for this liquid region "1" between these two radii, R_{C1} and R_{R1}. The radii are calculated using conservation of mass. In the case to calculate R_{R1}, the control volume is between R_{M1} and R_{R1}. The volume of liquid does not change then the conservation of mass equation is

$$\int_{\partial\Omega_{R_{M1}-R_{R1}}} \rho\vec{v}(r,t)\cdot\vec{n}\partial\Omega = -\frac{d}{dt}\int_{\Omega_{R_{M1}-R_{R1}}} \rho d\Omega = 0 \qquad \text{Equation 6.7}$$

and at time $t = 1/(4f)$, R_{R1} is equal to R_R, then at any time the volume of liquid is equal to the volume at time $t = 1/(4f)$:

$$\pi\left(R_{R1}^{\;2} - R_{M1}^{\;2}\right)\left(h_0 - \frac{a}{2}\right) = \int_{\Omega_{R_{M1}-R_{R1}}} d\Omega = \int_{R_{M1},0,0}^{R_{R1},2\pi,h} r\,dr\,d\phi\,dz = \left(\frac{R_{R1}^{\;2}}{2} - \frac{R_{M1}^{\;2}}{2}\right)2\pi h \qquad \text{Equation 6.8}$$

where it is possible to work out the value of R_{R1} as given by given by Equation 3.7.

$$R_{R1}(t) = R_{M1}\sqrt{1 + 2\frac{h_0 - \frac{a}{2}}{h(t)}} \qquad \text{Equation 3.7}$$

Working out in a similar way, the value of R_{C1} is obtained and given by Equation 3.6.

$$R_{C1}(t) = R_{M1}\sqrt{1 - \frac{h_0 - \frac{a}{2}}{h(t)}} \qquad \text{Equation 3.6}$$

Appendix C. Other properties of silicon nitride "E" and "F".

Table 6.1 Properties of Silicon Nitride according to the manufacturer Saint-Gobain.

MATERIAL	"E"	"F"
	NBD-200	SN101C
Sintering Aid	Mg0	$Y_2O_3;Al_2O_3$
Density [g/cm^3] (% Theoretical)	3.16 [>99.9%]	3.21 [>99.9%]
RT Flexural Strength [MPa]	>900	>1000
Weibull Modulus	>15	>25
Elastic Modulus [GPa]	320	310
Poisson's Ratio	0.26	0.27
Vicker's Hardness H_V10	1550	1600
Fracture Toughness [MPa * m$^{1/2}$]	>5.5	>6.5
Thermal Expansion Coeff. 10^{-6}/°C; [RT-1000?C]	2.9	3.7
Thermal Conductivity [W/mK] @ 25°C	29	34
Electrical Resistivity [Ω-cm]	1014	1014
Dielectric Constant @ 1MHz	8	8
Corrosion 5% HF Solution, 500 Hours Weight Loss/ Surface Area [g/cm^2]	0.68	0.1
Corrosion 5% HCL Solution, 500 Hours Weight Loss/ Surface Area [g/ cm^2]	0.0002	0.0036

Appendix D. Residual stress analysis in ceramic balls.

It is known that the ceramic balls for rolling application present a compressive residual stress on the surface that enhances the fatigue life and the abrasion resistance. The residual stress on the surface is produced during the sintering process that is divided in three phases: heating, heat preservation and cooling. As the surface is cooled down before the core of the ball, this surface fits an expanded hot core. When the core is at room temperature, the skin of the ball has to fit a smaller core and, consequently, is compressed (Ren et al. 2002).

In order to analytically study the stress tensor on the surface of the ball, a differential volume is defined in the ball by the radius, distance to the centre, and a differential angle. Its shape is a spherical cone. It is limited by the sphere with radius r, the sphere with radius $r + dr$, and the cone aperture is $2d\psi$. The centre of the spheres and the apex of the cone is the centre of the ball.

The equation of equilibrium in radial direction is

$$\sigma_r\left(\pi r^2 (d\psi)^2\right) + \sigma_t\left(2\pi r(d\psi)dr\right)d\psi = \left(\sigma_r + \frac{d\sigma_r}{dr}dr\right)\left(\pi(r+dr)^2 d\psi^2\right) \qquad \text{Equation 6.9}$$

That can be transformed into (Timoshenko and Goodier 1982):

$$\sigma_t = \sigma_r + \frac{r}{2}\frac{d\sigma_r}{dr} \qquad \text{Equation 6.10}$$

The Equation 6.10 has some important implication. The first one is that the existence of residual stress in the tangential direction is associated with residual stress in the radial direction. It is also possible to calculate the residual stress in radial direction if the residual stress in tangential direction it is known.

To solve the Equation 6.10, it is necessary to defined boundary conditions. As the boundary conditions at the core of the ball are unknown, an approximate solution that fulfils the equation and that is close to the real solution on the surface is presented.

As an example, a constant tangential residual stress of -400 MPa is assumed in the surface of a ball of 10 mm diameter. The ambient pressure is neglected. Then, the radial stress at radius 5 mm is zero.

Close to the surface, Equation 6.10 is expressed as:

$$-400 = 0 + \frac{r}{2}\frac{d\sigma_r}{dr} \quad \text{for } r = 5 \qquad \text{Equation 6.11}$$

where it is possible to calculate the values of σ_r close to the surface.

$$\sigma_r \approx -160(r-5) \quad \text{for } r \leq 5 \text{ and very close to 5} \qquad \text{Equation 6.12}$$

Then, at a depth of 100 µm the value of the tensile radial residual stress is approximately 16 MPa, and for a depth of 200 µm it is approximately 32 MPa. As it is shown here, a compressive residual stress in tangential direction is linked to a tensile residual stress in radial direction.

The residual stress increases the fatigue life of the ceramic balls because prevents the small and orthogonal to the surface cracks from growing. However, to keep the equilibrium of forces it is necessary to have a tensile residual stress in the same place but in different direction.

It is shown that the compressive residual stresses are always linked to tensile residual stress. To have this situation there are two possibilities that might appear separately or together. One possibility is to have tensile and compressive residual stresses in different direction, like this case; the other possibility is to have tensile and compressive residual stresses in different location, like, for example, in the case of a too short metal beam welded in a structure.

Appendix E. X-ray diffraction angles and phase analysis in zirconia.

The phases of zirconia are given \by the software DiffracPlus of the Bruker X-ray diffraction solution. This software has a database of the crystal structures reported in the literature. It compares the results obtained with the diffraction angles of the database. According to this software the phases are:

	Diffraction angle	Z	a	b	c	β
Tetragonal P42/nmc (137)	30.1°	2	3.612	3.642	5.211	90°
Monoclinic P21/c(14)	26.4°	4	5.21	5.26	5.37	80.53°
Monoclinic P21/c(14)	28.1°	4	5.18549	5.21202	5.37736	98.798°

where Z is the number of formulas per cell, a, b, and c are the interatomic distances measured in Ångströms and β is the crystal structure angle.

Appendix F. ASTM G32 Summary.

The introduction given by the American Society for Testing and Materials indicates that the ASTM G32 test may be used to determine the cavitation erosion resistance in materials present "*in pumps, hydraulic turbines, hydraulic dynamometers, valves, bearings, diesel engine cylinder liners, ship propellers, hydrofoils, and in internal flow passages with obstructions*".

The erosion is produced by ultrasonic cavitation that is believed to have basically the same erosion mechanism that the hydrodynamic cavitation encountered in current applications.

The test describes two different procedures: the normal test where the specimen is threaded to the horn tip and the "stationary specimen method" where a flat specimen is placed in front of the horn tip. The latest is only suitable in case the specimen cannot be threaded as it is the case of ceramics.

The results of the test might be also used as a screening test for liquid impingement erosion resistance of materials, although there are other specific tests for this purpose. The test is not recommended for elastomeric or complaint coatings because they might reduce the severity of the cavitation.

In the results from this test, the shape of the curve "material loss-exposure time" has to be considered since the erosion nature is nonlinear. Also, the standard specifies some reference materials to verify the results. It gives guidance on the setting-up of the experiment and preparation of specimens.
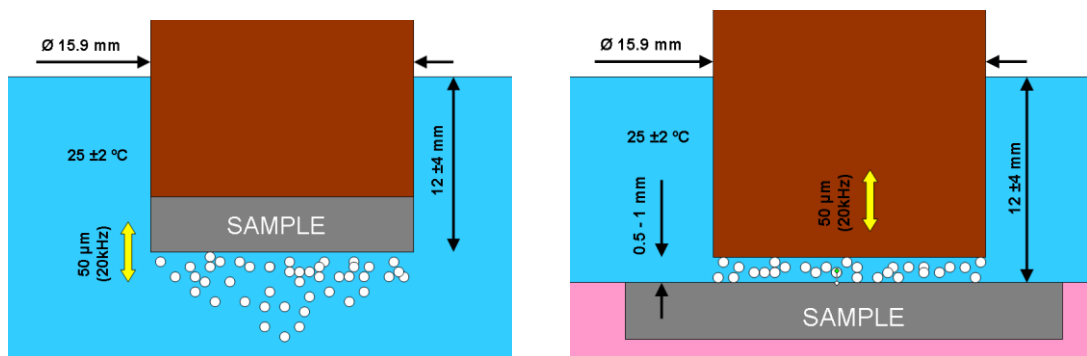
ASTM G32 test and the "stationary specimen method" defined in the ASTM G32

The main parameters of the ASTM G32 test are summarized here:

- Frequency: 20 ± 0.5 kHz
- Peak to peak amplitude: $50 \, \mu m \pm 5\%$
- Immersion depth: 12 ± 4 mm
- Liquid depth: >100 mm
- Nominal beaker size: $\geq 2000 \, cm^3$
- Temperature of distilled water: 25 ± 2 ºC
- Tip diameter: 15.9 ± 0.05 mm
- Specimen height: $4 - 10$ mm
- Specimen surface roughness: $0.8 \, \mu m$ r.m.s.
- Maximum specimen chamfer or radius: < 0.15 mm
- Concentricity of the horn respect to the beaker: 5%
- Gap between tip and specimen (stationary specimen): $0.5 - 1$ mm